Delta – Atlanta Hartsfield (UNA-UNA) Study

prepared by

Prem Lobo, Philip D. Whitefield, Donald E. Hagen, Max B. Trueblood, Nathan L. Mundis, Ian P. Magdits
University of Missouri – Rolla

Scott C. Herndon, Tim Onasch, John T. Jayne, Richard C. Miake-Lye
Aerodyne Research

Wynn L. Eberhard
Earth Systems Research Laboratory
National Oceanic and Atmospheric Administration

Roger Wayson
U.S. Department of Transportation

February 2008

FINAL REPORT

DELTA – ATLANTA HARTSFIELD (UNA-UNA) STUDY

February 2008

Prepared by:

Prem Lobo, Philip D. Whitefield, Donald E. Hagen, Max B.
Trueblood, Nathan L. Mundis, Ian P. Magdits
University of Missouri – Rolla

Scott C. Herndon, Tim Onasch, John T. Jayne, Richard C.
Miake-Lye
Aerodyne Research

Wynn L. Eberhard
Earth Systems Research Laboratory, National Oceanic and Atmospheric Administration

Roger Wayson
United States Department of Transportation

Any opinions, findings, and conclusions or recommendations expressed in this material are those of the authors and do not necessarily reflect the views of the FAA, NASA or Transport Canada.

Center of Excellence for Aerospace Particulate Emissions Reduction Research

FINAL REPORT

Delta – Atlanta Hartsfield (UNA-UNA) Study

Prepared by

Prem Lobo, Philip D. Whitefield, Donald E. Hagen, Max B. Trueblood,
Nathan L. Mundis and Ian P. Magdits
Center of Excellence for Aerospace Particulate Emissions Reduction Research
G-7 Norwood Hall, University of Missouri – Rolla, Rolla, MO 65409
Contact: plobo@umr.edu or pwhite@umr.edu

Scott C. Herndon, Tim Onasch, John T. Jayne and Richard C. Miake-Lye
Aerodyne Research Inc.,
45 Manning Road, Billerica, MA 01821
Contact: herndon@aerodyne.com or rick@aerodyne.com

Wynn L. Eberhard
Earth Systems Research Laboratory
National Oceanic and Atmospheric Administration,
325 Broadway, Boulder CO 80305
Contact: Wynn.Eberhard@noaa.gov

Roger Wayson
U.S. Department of Transportation,
Research and Innovative Technologies Administration,
John A. Volpe National Transportation Systems Center,
Environmental Measurement and Modeling Division, RTV-4F, Cambridge, MA 02142
Contact: Roger.Wayson@volpe.dot.gov

Acknowledgments

Table of Contents

List of Figures

List of Tables

Abstract

This report describes the results of an aviation PM emissions campaign entitled the Delta-Atlanta/Hartsfield (previously known as UNA-UNA (Un-named Airline - Un-named Airport)) Study. There were two components to this study – a dedicated engine test and an airport study where advected plumes were sampled from commercial transports during normal airport operations. This report describes both measurement activities, and shows the tremendous promise for a fresh perspective on the magnitude and nature of aviation emissions under 'real-world' conditions, the analysis and interpretation of which was greatly informed by the dedicated engine tests. These two approaches together form the basis of a combined aviation emissions characterization program which is informative, thorough, atmospherically relevant, and novel. The findings from this study together with those from the other campaigns will reshape the understanding of aviation emissions associated with airport local and regional air quality and may settle several outstanding questions with respect to particulate emission from aviation sources. Finally, this report underscores a need for further analysis of these data.

Executive Summary

In September 2004, mobile laboratories operated by University of Missouri-Rolla (UMR), Aerodyne Research, Inc. (ARI) and the National Oceanic and Atmospheric Administration (NOAA) were deployed at Hartsfield-Jackson Atlanta International Airport to conduct two series of measurements of aircraft engine generated PM emissions. The first series was conducted at the maintenance facilities of Delta Airlines and focused on PM emissions in the vicinity of the exhaust nozzle of several different aircraft whose engines were cycled through a matrix of reproducible engine operating conditions. The second series was conducted by placing the mobile laboratories adjacent to and downstream of active runways. In these latter measurements advected exhaust plumes generated by a broad mix of commercial transport aircraft taxiing and departing the airport during normal operations were detected and analyzed.

This study was originally subject to non-disclosure agreements between the research team and Delta Airlines and until December 2006 was referred to as the Un-named Airline - Un-named Airport (UNA-UNA) Study. In November 2006, a meeting was arranged between the test coordinators, test team and representative from Delta Airlines and the Atlanta Hartsfield Airport to secure the release of the data and rescind the non-disclosure agreement. An overview of the test campaign along with analyzed data was presented at this meeting. Shortly thereafter, legal representatives of Delta Airlines agreed to terminate the non-disclosure agreement, permitting the public release of the data, and asked that the study be henceforth known as the Delta-Atlanta Hartsfield Study. This study represents the achievement of one of the first milestones on the Aviation Emissions Characterization Roadmap (AEC Roadmap, formerly PM National Roadmap). It represents one of the first opportunities to measure PM emissions from in-service commercial transports and blazed the trail for the subsequent studies JETS APEX2 and APEX3.

The first series of measurements took place between 10:00pm and 5:00am on 21-25 September. The aircraft tested were selected from those scheduled to be overnight at the airport. The exhaust plumes of each aircraft were investigated using both probe sampling at the engine exhaust nozzle exit (UMR-ARI) and remote sensing using LIDAR (NOAA) at a point in the plume close to the exhaust nozzle exit thus permitting comparisons of measurement techniques. Another objective was to acquire PM emissions data from engines on in-service commercial transport aircraft. Associated with this objective, was a study of engine to engine variation within the same class. The airframes and engines studied are listed in the table below.

Date	Aircraft Number	Airframe	Engine	Thrust (kN)
September 22, 2004	908	MD-88	JT8D-219	93
September 23, 2004	918	MD-88	JT8D-219	93
September 23, 2004	134	B767-300	GE CF6-80A2	217
September 24, 2004	1816	B767-400ER	GE CF6-80C2B8F	258
September 24, 2004	635	B757-200	PW 2037	166
September 25, 2004	640	B757-200	PW 2037	166

The range of engine operating conditions examined focused on the Landing Take-Off (LTO) cycle with additional intermediate settings. For the JT8Ds the complete range of power settings was explored, but for the higher thrust engines, transient instabilities induced in the probe stands at mid to high power limited the range of powers sampled.

The probe sampling measurements by UMR focused on physical characterization measurements including particle size distribution, number density and soluble mass fraction. ARI focused on using an Aerosol Mass Spectrometer and related supporting instruments to quantify the composition of the particles as a function of size and power. Concurrent with the probe sampling, remote sensing was performed by NOAA using a mobile LIDAR system. NOAA supplied and operated the LIDAR, which used eye-safe ultraviolet light from a laser pulsing at 10 Hz and scanned the beam up and down in a vertical plane perpendicular to the direction of engine exhaust. The LIDAR system was contained in a trailer positioned about 300 m from the aircraft. The principal wavelength for this project was 355 nm. The back scatter (or reflection) of energy from the laser by the total aerosols emitted by the aircraft engine was measured just behind the rear stabilizer of the aircraft by the LIDAR.

Gas turbine engine emissions are influenced by engine power settings and ambient conditions at the engine inlet. For discussions of the influence of test operating conditions on the exhaust aerosol, it is convenient to represent the size distributions with characteristic parameters: number-based geometric mean diameter (Dgeom), geometric standard deviation (Sigma), mass-based geometric mean diameter (DgeomM), and total concentration; and the derived size dependent parameters: number-based emission index (EIn) and mass-based emission index (EIm).

For the JT8Ds, Dgeom increases with engine power setting from minima ~20nm to maxima ~ 40nm. Sigma increases slightly with power from ~1.7 at low power to ~1.8 at high power. DgeomM exhibits a minimum ~30% power with relatively high values at low and high power. EIn is higher at the low power conditions, exhibits a minimum at 30% power and then increases with power. EIm is similar to EIn, higher at the low power conditions, exhibits a minimum at 30% power and then rapidly increases with power. These trends are consistent with behavior of the CFM56-2C1 engine studied in the APEX campaign.

The two JT8D engines in this study have the greatest black carbon emission indices. This is due to a prevalent soot mode at 40-80 nm (particle mobility diameter). The CF6 and

PW2037 engines emit soot in a smaller size mode, < 50nm with overall less total black carbon mass. These engines, however, have a greater particle number emission index than the JT8D. Anecdotally, the JT8D emits fewer but larger particles while engines designed to reduce smoke number certification measurements emit more numerous quantities of smaller particles.

Studies for CF6-80s were confined to low and mid power conditions due to probe rake limitations. In contrast to the JT8Ds, no statistically meaningful power dependence was observed. The range of low and mid power PM parameters for the CF6-80s were comparable to those for the JT8Ds.

Data for the PW2037 again suggests a trend of increasing emissions with power, but high power points were not sampled due to probe rake limitations. It should be noted that in other engines studied (JT8D, CFM56) it was the high power points that made the power dependency most evident. The range of low and mid power PM parameters for the PW2037s were also comparable to those for the JT8Ds.

From least EIn to greatest, the trend is CF6-80C2B8F, PW2037, JT8D-219 and CF6-80A2. The AMS Organic particulate loading qualitatively correlates with the ICAO UHC with a couple of outliers in the JT8D-219. This is reasonable since the mechanism leading to incomplete combustion and unburned hydrocarbons is also likely to produce partially combusted low volatility species which can either participate in nucleation or condense to available soot surface area. In the case of the JT8D-219 engine, the latter is quite likely due to the presence of a relatively greater black carbon emission index.

From the LIDAR analysis, similar trends for the MD88s, CF6-80s and PW2037s are observed. The MD88's (JT8D engines) exhibited strong emissions at high power settings, substantial emissions at idle (4%) and taxi (7%) power settings, and low emissions at other power settings. The B767's (CF6-80 engines) had low emissions, even negative values. (It is of course impossible to have negative soot emissions, but the noise in the data, nonuniform ambient, and imperfections in the theory could all contribute to negative values of *EI*. These negative *EI* values help indicate the limits of accuracy in the current LIDAR method). The B757's (PW2037 engines) had emission index values that overall were between those of the MD88's and the B767's. Differences between the two aircraft of one type were smaller than differences between types of aircraft.

Upon completion of the dedicated engine testing, the various groups turned their attention to measurements of aircraft emissions on the airfield at various locations near the ends of runways where takeoff operations were occurring. With the exception of the data acquired on 26 September it was not possible to collocate the LIDAR and the UMR-ARI measurement systems. Despite this limitation, for the overall project both groups were successful in data collection with 344 takeoffs being measured by the LIDAR and in excess of 500 taxi and takeoff events by the UMR-ARI measurement system.

The UMR and ARI mobile laboratories were positioned with assistance from airport operations staff just downwind of an active runway. Two locations were selected to

perform these measurements based on the prevailing wind direction on a given day. On September 27, 2004, the prevailing wind was from the N/NE and UMR and ARI were collocated on the western end of the airport's southern runways, and on September 28 and 29, 2004 the prevailing wind shifted to the W/NW direction and UMR and ARI moved to the eastern end of the southern runways. In this work, exhaust plumes advected in the direction of the sampling systems were continuously analyzed. Exhaust pollutant emission ratios relative to exhaust CO_2 were determined for various gas-phase and particulate metrics by looking at the concomitant rise in the measurement of a target pollutant above background with increased CO_2. These emissions ratios were converted to fuel based emissions indices using above ambient CO_2 as an internal exhaust plume tracer. The characteristic of advected plumes - plume rise and plume spread (horizontal and vertical) were measured using the LIDAR technique. These measured parameters are key variables in dispersion modeling and are being used to help in model development.

Due to the vast nature of this dataset, analysis is still ongoing for many of the plumes observed. In order to demonstrate the potential of this dataset, two specific subset analyses are presented here. The first encompasses 12 aircraft plume events that have been selected for detailed analysis. These events were chosen to cover a variety of engine technologies and conditions. The following general conclusions from these selected analyses can be drawn.

- The combination of the PM and gas analysis of the advected plume provides unique identification of the engine operating condition generating the plume, i.e. idle, spool-up, maximum thrust, etc.
- When compared to engine exit plane measurements, it is clear that extensive secondary volatile aerosol formation is occurring during plume advection.
- The black carbon component of the PM emissions detected in the advected plume appears to be a strong function of engine model.

The second subset encompassed 289 takeoff plumes, sampled over the three day campaign. These plumes were selected because they were generated by six of the most common engine types, then operating at Atlanta Hartsfield. Daily engine by engine averages of PM number- and mass-based emission indices have been calculated. It should be noted that the emission indices were based on DMS500 measurements and were corrected for size dependent line loss. Since most of the particles have diameters <20nm, these line loss corrections significantly impact the number-based emission index calculations. For all engines, for all days, the following range of values was observed:

EIn: $3*10^{16} - 2*10^{17}$ particles/kg fuel
EIm: $0.1 - 0.35$ g/kg fuel

These averages, based on measurements of PM emissions from in-service aircraft under normal operating conditions, give credence to the rough averages reported by Penner et al., 1999 in the IPCC report – *Aviation and the Global Atmosphere*.

1.0 Background

1.1 Introduction

The growth of commercial air traffic over the last decade has led to an increased contribution to the local inventory of gaseous and particle emissions from the operations associated with airports, e.g. aircraft engines, auxiliary power units (APUs) and ground support equipment (GSEs). The potential negative impact on human health due to the growth of aviation emissions has prompted a series of studies to better understand the formation and quantification of several pollutants, with the primary focus on aircraft engine Particulate Matter (PM) emissions. The physical and chemical characterization of PM emitted by gas turbine engines have received attention under several recent research programs, e.g. the NASA (National Aeronautics and Space Administration) EXCAVATE (EXperiment to Characterize Aircraft Volatile Aerosol and Trace-species Emissions) (Anderson et al.) and APEX1 (Aircraft Particle Emissions eXperiment) (Wey et al., 2006) programs, and the European PartEmis (Measurement and prediction of emissions of aerosols and gaseous precursors from gas turbine engines) project (Wilson et al., 2004). The Delta-Atlanta Hartsfield Study was the second study conducted following APEX1. This study was conducted through the Partnership for AiR Transportation Noise and Emissions Reduction (PARTNER) – an FAA-Transport Canada-NASA-sponsored Center of Excellence, in partnership with the aviation industry.

Under the Clean Air Act (CAA), EPA has the authority to designate areas that are not in compliance with outdoor clean air requirements promulgated in the National Ambient Air Quality Standards (NAAQS). A large number of airports, especially the major airports across the country, are located in urban areas designated by EPA as non-attainment areas. Because of the potential need to mitigate PM from all sources, including aviation, in order to bring these areas back into compliance with NAAQS, these affected airports are in dire need for an accurate assessment of aviation contribution, as compared to other sources, to the local and regional air shed. FAA co-funded the Delta-Atlanta Hartsfield Study, as well as other follow-on studies, to collect data for developing tools and databases that airports could use to make these assessments.

Major pollutants emitted from aircraft engines such as nitrogen oxides, carbon monoxide and hydrocarbon are regulated; however there are currently no US regulations on PM. Because current understanding seems to point to PM as a potential health risk, and because there is potential for PM emissions to increase as the growth of aviation continues, it is necessary to develop the technical and scientific basis to support considerations of various options for appropriately addressing the identified health risk attributable to aviation related PM emissions. The main purpose of this study is to acquire PM data on some of the engines that are represented in a majority of aircraft that make up the current fleet. From this and other follow-on studies, the aviation community will be able to better assess aircraft PM emissions and their impact on the local, regional and global scale. Ultimately, the collected data will help to support decision making on mitigation including streamlined ground operations to reduce delays, use of alternative fuels or low sulfur fuels to reduce emissions.

The data from the Delta-Atlanta Hartsfield study were collected using best engineering practices and only provided snapshots of emissions levels of the tested engines under certain ambient conditions. Further analyses beyond what was made in this report may be required for application of the collected data.

1.2 Delta-Atlanta Hartsfield (UNA-UNA) Study

In September 2004, mobile laboratories operated by University of Missouri-Rolla (UMR), Aerodyne Research, Inc. (ARI), and the National Oceanic and Atmospheric Administration (NOAA) were deployed at Hartsfield Jackson Atlanta International Airport to conduct two series of measurements of aircraft engine generated PM emissions. Testing was divided into two phases: (1) Dedicated aircraft engine tests under controlled operations, with the cooperation of Delta Airlines; and (2) Non-dedicated aircraft under routine take-off operations, with the cooperation of the Atlanta-Hartsfield International Airport.

Engine technology comparisons were performed by various groups, combined into a single team. The team consisted of individuals from Federal Aviation Administration (FAA), National Aeronautics and Space Administration (NASA), John Volpe National Transportation Systems Center (Volpe), University of Central Florida (UCF), National Oceanic and Atmospheric Administration (NOAA), Aerodyne Research, Inc. (ARI)., and the University of Missouri-Rolla (UMR).

The first phase of the study was conducted at the maintenance facilities of Delta Airlines between 10:00pm and 5:00am on 21-25 September, and focused on PM emissions in the vicinity of the exhaust nozzle of several different aircraft whose engines were cycled through a matrix of reproducible engine operating conditions. Measurements were made at the engine exhaust nozzle exit with state-of-the-art rapid response instrumentation at a range of engine power conditions, including the four International Civil Aviation Organization (ICAO) power points The aircraft tested were selected from those scheduled to be overnight at the airport. The exhaust plumes of each aircraft were investigated using both extractive probe sampling at the engine exhaust nozzle exit (UMR/ARI) and remote sensing using non-intrusive LIDAR (NOAA) at a point in the plume close to the exhaust nozzle exit thus permitting comparisons of measurement techniques. A secondary objective was to acquire PM emissions data from engines on in-service commercial transport aircraft. The airframes studied included B757s, B767s and MD88s.

The second phase of the study was conducted by placing the mobile laboratories adjacent and downstream of the "break-release" (i.e. starting point) end of an active take-off runway. In these measurements advected exhaust plumes generated by a broad mix of commercial transport aircraft departing the airport during normal operations were detected and analyzed. The optimal sampling location for these measurements was dependent on prevailing wind direction. Both taxi/idle emissions and those during take-off were measured for several in-service commercial aircraft during routine operation.

Again, the focus was on measuring particles emitted from the aircraft, with supporting ancillary measurements to make complete emissions measurements. These tests were performed on a non-interference basis, so that normal airport operations can continue without being affected by the measurement teams' activities. As with the dedicated engine study, LIDAR measurements were also performed as part of this study.

This study was originally subject to non-disclosure agreements between the research team and Delta Airlines and until December 2006 was referred to as the Un-named Airline - Un-named Airport (UNA-UNA) Study. In November 2006, a meeting was arranged between the test coordinators, test team and representative from Delta Airlines and the Atlanta Hartsfield Airport to secure the release of the data and rescind the non-disclosure agreement. An overview of the test campaign along with analyzed data was presented at this meeting. Shortly thereafter, legal representatives of Delta Airlines agreed to terminate the non-disclosure agreement, permitting the public release of the data, and asked that the study be henceforth known as the Delta-Atlanta Hartsfield Study. This study represents the achievement of one of the first milestones on the PM National Roadmap. It represents one of the first opportunities to measure PM emissions from in-service commercial transports and blazed the trail for the subsequent studies JETS APEX2 and APEX3.

1.2.1 Dedicated Engine Study

In the fall of 2004, the mobile laboratories operated by UMR, ARI and NOAA were deployed at the maintenance facilities of Delta Airlines. The use of a mobile laboratory platform to sample aviation related plumes has been documented (Hagen et al., 1992; Schmid et al., 2004; Whitefield et al., 2005; Herndon et al., 2004, 2005, 2006) previously. The purpose of the first week of measurement activities was to characterize the particulate emissions at the exit plane of the engine exhaust nozzle for wide-bodied commercial aircraft at known power conditions using state of the art research instrumentation (see UMR and ARI sections for details on instrumentation deployed at this test). These measurements were performed during the early hours of September 22-25, 2005. The aircraft engines tested along with the associated airframes are listed in Table 1.

Table 1: List of aircraft engines and associated airframes tested

Date	Aircraft Number	Airframe	Engine	Thrust (kN)
September 22, 2004	908	MD-88	JT8D-219	93
September 23, 2004	918	MD-88	JT8D-219	93
September 23, 2004	134	B767-300	GE CF6-80A2	217
September 24, 2004	1816	B767-400ER	GE CF6-80C2B8F	258
September 24, 2004	635	B757-200	PW 2037	166
September 25, 2004	640	B757-200	PW 2037	166

1.2.1.1 Experimental Description

Custom-designed probes and extensive support equipment were used to sample jet exhaust in the on-wing position. Particle-laden exhaust is extracted directly from the engine exhaust flow through probes and supplied to the measurement devices. The primary probe for collecting exhaust samples (Fig. 1) is positioned within 1 meter of the exhaust nozzle exit plane, as this position is representative of the engine signature and the certification data in the ICAO database (ICAO, 2006)

Figure 1: Probe stand used to sample jet exhaust

The PM probes are designed to provide both probe tip and upstream (0.09 meters from tip) dilution flows, thereby reducing and/or eliminating probe effects. The rake quadrant and probes are water cooled to protect them from thermal degradation during testing. The dilution flows are drawn from particle-free, dry air sources located in the mobile laboratory and conducted to the probes through 0.006-meter (inside diameter) flexible gas lines.

The PM samples were conducted to the mobile laboratories through sample lines for which line losses had been calibrated. The mobile laboratories were typically located near the aircraft wing tips, less than 30m from the engine.

Data was acquired for a typical cycle involving the following engine power conditions – 4%, 7%, 30%, 50%, 70%, 85% and 100%. In case of the 767s and 757s, the total number of engine conditions visited was limited to the low to mid power conditions because the probe stand appeared to be unstable at the higher power settings.

The LIDAR performed repeated scans behind a stationary aircraft. These measurements were used to evaluate a new method for determining total aerosol emission rates from the LIDAR data. For these tests, the LIDAR was located relatively close to the exhaust exit plane and the total aerosol at this point is primarily soot.

1.2.2 Airport Study

The UMR, ARI and NOAA mobile laboratories were positioned with assistance from airport operations staff just downwind of an active runway at a major US airport. Two locations were selected to perform these measurements based on the prevailing wind direction on a given day. On September 27, 2004, the prevailing wind was from the N/NE and UMR and ARI were collocated on the western end of the airport's southern runways, and on September 28 and 29, 2004 the prevailing wind shifted to the W/NW direction and UMR and ARI moved to the eastern end of the southern runways. In this work, ambient air was continuously analyzed through a sample port located near the roof on the front of the ARI truck (facing the runway) on the driver's side and delivered to various instruments on board the mobile laboratory. The UMR mobile laboratory sampled air through a port located at the back of the cabin (facing the runway). With the exception of the data acquired on 26 September it was not possible to collocate the LIDAR and the UMR-ARI measurement systems.

Exhaust pollutant emission ratios relative to exhaust CO_2 were determined for various gas-phase and particulate metrics by looking at the concomitant rise in the measurement of a target pollutant above background with increased CO_2. These emissions ratios can be converted to fuel based emissions indices using above ambient CO_2 as an internal exhaust plume tracer (Anderson et al., 1998; Fahey et al., 2005; Schäfer et al., 2003). An overview of the kinds of experiments which have been performed using a mobile laboratory platform has been published by Kolb et al., 2004. The characteristic of advected plumes - plume rise and plume spread (horizontal and vertical) were measured using the LIDAR technique. These measured parameters are key variables in dispersion modeling and are being used to help in model development.

During the daylight hours, aircraft tail numbers were recorded which allows an unambiguous identification of the airframe and engine. When the weather precluded a visual identification, the Volpe Transportation Center and the Federal Aviation Administration provided tower logs as well as AQSP databases to identify the specific engine in use for the given flight.

2.0 Methodology

2.1 UMR Methodology

UMR has developed a mobile diagnostic facility and a sampling methodology which are optimized for jet engine exhaust characterization using extractive sampling techniques. Over this time the mobile sampling facilities have been used in numerous test campaigns at airports with parked aircraft, NASA and industrial facilities having combustor and engine test stands, and at venues having altitude chambers (Hagen et al., 1992, 1999; Whitefield and Hagen, 1995; Whitefield et al., 1997, 2001; Lobo et al., 2007). An overall review of the UMR facility and methodology has been reported elsewhere (Schmid et al., 2004).

The instrumentation onboard the UMR mobile laboratory included the Cambustion DMS 500, a fast particulate spectrometer (Biskos et al., 2005), to gather real–time size distribution information and total concentration of engine exhaust particulates over the full particle size spectrum from 5nm to 1000nm; a differential mobility analyzer to develop number, surface area and volumetric size distributions; two TSI Condensation Particle Counters (CPC) to measure total number concentration; a fast response CO_2 detector to establish emission factors; a deliquescence system to measure the total soluble mass fraction and a weather station to monitor ambient conditions like temperature, relative humidity, pressure, and wind speed and direction.

From the size distributions acquired during equilibrium engine operating conditions, parameters like Dgeom (number based geometric mean diameter), Sigma (geometric standard deviation) and DgeomM (mass based geometric mean diameter) can be obtained. Using the CO_2 data and assuming a density of 1 for the jet exhaust, EIn (number based emission index) and EIm (mass based emission index) can also be determined.

2.1.1 PM Parameters

The characterization of the exhaust aerosol is accomplished using the following parameter set.

(1) The size distribution is described by a differential concentration function $N(D_p)$, dependent on particle diameter (D_p), which specifies the concentration of particles, dn, having the logarithm of their diameters between $\log D_p$ and $\log D_p + d\log D_p$ to be $N*d\log D_p$. The logarithmic scale is used since aerosol diameter covers such a large size range.

$$dn = N * d \log D_p \qquad\qquad\qquad (\text{Eq. 1})$$

(2) Number-based geometric mean diameter (Dgeom), defined by the equation

$$\log Dgeom = \frac{1}{n_0} \int_0^\infty \log Dp * dn = \frac{1}{n_0} \int_0^\infty \log D_p * N * d \log D_p \qquad \text{(Eq. 2)}$$

where $\mathbf{n_0}$ denotes the total particle concentration,

$$n_0 = \int_0^\infty N * d \log D_p \qquad \text{(Eq.3)}$$

(3) Geometric standard deviation (Sigma), defined by

$$\log \sigma_g = \left(\frac{\int_0^\infty \left(\log\left(Dp / Dgeom \right) \right)^2 Nd \log D_p}{n_0 - 1} \right)^{\frac{1}{2}} \qquad \text{(Eq. 4)}$$

(4) Mass-based geometric mean diameter (DgeomM), defined by

$$\log DgeomM = \frac{1}{\int_0^\infty D_p{}^3 * N * d \log D_p} \int_0^\infty \log D_p * D_p{}^3 * N * d \log D_p \qquad \text{(Eq. 5)}$$

(5) Number based emission index (EIn), the number of particles per kilogram fuel burned can be calculated by

$$EIn = EI_{CO_2} \frac{N_0}{M(CO_2)} \qquad \text{(Eq. 6)}$$

where EI_{CO_2} denotes the mass emission index of CO_2 (for aircraft engines $EI_{CO_2} = 3160$ g/kg; (Schulte and Schlager (1996)). $M(CO_2)$, the mass of CO_2 per volume exhaust sample, is calculated by multiplying measured CO_2 mixing ratios with $(44/29)\rho_{air}$, where ρ_{air} is the air density and 44/29 is the molar mass ratio of CO_2 and air. Strictly speaking, in Eq. 6 both N_0 and $M(CO_2)$ have to be values above ambient, i.e. enhancements over the background signal. However, for measurements close to the engine exit plane of gas turbine engines, the background signals are negligibly small.

(6) Mass-based emission index (EIm) is the mass of particles per kilogram fuel burned and its calculation is analogous to that for EIn and is given by

$$E\,Im = EI_{CO_2} \frac{M(N_0)}{M(CO_2)} \qquad \text{(Eq. 7)}$$

where $M(N_0)$ is the mass of aerosol per unit volume of exhaust sample.

2.1.2 Soluble Mass Fraction

The evolution of combustion particles in the atmosphere is strongly influenced by their ability to interact with water vapor. This characteristic was investigated with a deliquescence technique (Alofs, 1978; Alofs and Trueblood, 1981; Li et al., 1992), where a tandem DMA with an intermediate saturator was used to measure the particles' dry and wet diameters.

The UMR Deliquescence apparatus (DDMA) is designed to determine the fraction of soluble mass in the average aerosol particle of a given, predetermined dry size. It utilizes two Differential Mobility Analyzers (DMA) with a humidifier in between them. The first DMA selects a narrow band of diameters and passes these particles on to a region of precisely controlled, high relative humidity or saturation ratio (typically SR=0.93). If these aerosol particles contain any soluble mass, then they will take on liquid water, i.e., they will deliquesce or grow to some new equilibrium diameter. This new equilibrium diameter is a function of the dry diameter, the saturation ratio in the humidifier, and the fraction of soluble mass in the particle. The deliquesced aerosol then passes through the second DMA (The sheath air for this DMA is also brought to SR = 0.93). Here a computer controlled size sweep is performed and the wet diameter is obtained. As stated earlier, knowledge of the dry diameter, the saturation ratio, and the wet diameter is sufficient to determine the Soluble Mass Fraction (SMF) for that aerosol.

SMF increases with distance from engine exit plane as the time allowed for the aerosol particle to scavenge soluble species like H_2SO_4 increases. The average aerosol particle contains essentially no soluble material if captured by the probe at the engine exit plane, since the sample is diluted while it is still very hot, i.e., chemical reactions are quenched.

2.2 ARI Methodology

The measurements of gas-phase and particulate emissions for the take-off mode of operation are the primary focus of this section. The primary gas-phase species measured were CO_2, NO, NO_2, CO and HCHO. The total particle number count was measured using a condensation particle counter (CPC). Total black carbon mass was measured using the Multi-Angle Absorption Photometer (MAAP). Various non-refractory particulate constituents were measured using the Aerosol Mass Spectrometer (AMS). Size resolved particulate number measurements were performed with several different instruments, including two Scanning Mobility Particle Sizers (SMPS) and the Cambustion DMS 500. The measurements of HCHO and NO emissions were performed using Tunable Diode Laser Differential Absorption Spectroscopy (TILDAS). NO_2 and CO were measured using a similar TILDAS approach, but with a dual channel quantum

cascade laser based instrument (Jimenez et al., 2005). Carbon dioxide, CO_2 was measured using a commercial non-dispersive infrared absorption technique (Licor 6262).

2.2.1 HCHO, HCOOH and NO measurement

The TILDAS instrument has been described thoroughly elsewhere (McManus et al., 2005), and has been employed in several field measurement campaigns(Zahniser et al., 1995; Horii et al., 1999; Li et al., 2003) but details specific to the instrument deployed in these measurements are described here. HCHO and HCOOH were detected using a multiple absorption lines at 1765 cm^{-1}. A relatively weak water line is present in this feature and was fit as well. The diode used for NO was operated at approximately 1915 cm^{-1}. As operated during these measurements, the 1 s rms precisions for HCHO (diode 1) was normally less than 0.7 ppbv. For NO (diode 2) the 1s rms precision was 1.1 ppbv.

The accuracy of the concentrations measured by TILDAS is largely determined by how well the line strengths are known. For the absorption lines used in the two instrument channels, the band strength for HCHO is known to within 7% (Herndon et al., 2005; Volkamer, 2005). The bandstrength for NO is known to within 6% (Smith et al., 1985).

2.2.2 NO$_2$ and CO measurement

The quantum cascade laser based instrument (QCL) has been deployed in previous field campaigns (Yelvington et al., 2007; Wormhoudt et al., 2007) and studied in the lab (Jimenez et al., 2005). Briefly, NO_2 was detected via absorbance at 1606 cm^{-1} and the bandstrength is known to within 4% (Smith et al., 1985). CO was detected with two different absorption lines during the campaign at 2179.8 cm^{-1} and 2183.2 cm^{-1}.

2.2.3 CO$_2$ Measurement

The Licor-6262 non-dispersive infrared absorption instrument detects CO_2 absorption in the 4.3 μm band. Additional details regarding its performance in this application can be found elsewhere (Herndon et al., 2004). The response time of the Licor instrument was measured by flooding the inlet tip with CO_2 free nitrogen gas. The response time of the Licor was found to be 0.9 seconds.

2.3 NOAA Methodology

The LIDAR was used previously to measure the time-evolving geometry of exhaust plumes from commercial jet aircraft 17-24 May 2001 at Los Angeles International Airport (LAX) (Wayson et al. 2003; Eberhard et al. 2005). For this campaign, the LIDAR was used to measure the growth and rise of the exhaust plume behind the aircraft due to the initial dynamics of turbulent mixing of the high-speed, warm exhaust jet for

airfield measurements and also to explore the measurement of total mass flux during the dedicated engine tests. Particles generated by the engine usually provided enhanced backscattering detectable by the LIDAR above the backscattering from ambient molecules and aerosol particles. The results were used to provide more accurate plume initial conditions to an air quality model, which then used conventional winds and turbulence to transport and further disperse the exhaust plume. This led to more accurate estimates of the effect of jet aircraft on air quality in the area of the airport (Hall et al. 2003).

During those measurements it was observed that that the total backscatter (although uncalibrated) tended to be greater for larger aircraft, for more visually distinct plumes, and for aircraft of older design. Those qualitative observations were a motivation to develop a method to quantify soot emission rates using calibrated LIDAR backscatter.

2.3.1 LIDAR Description

A LIDAR transmits a pulse of light, which undergoes scattering and absorption as it propagates away from the system. A small part of the scattered light travels straight back to the LIDAR, where it is gathered and focused by a telescope onto a detector. The detector voltage is digitized as a function of time, and recorded as a function of range from the LIDAR.

After calibration and other factors are applied, the LIDAR signal can be expressed as:

$$P = C\left[\beta_p(R) + \beta_m(R) + \beta_h(R)\right] \qquad \text{(Eq. 8)}$$

$$\times \exp\left\{-2\int_0^R \left[\sigma_p(R') + \sigma_m(R') + \sigma_h(R')\right]dR'\right\}$$

where C is the calibration factor, R is range, β is volumetric differential backscatter cross-section, σ is volumetric extinction coefficient, and subscripts p, m, and h refer to particles in the exhaust plume, air molecules, and ambient aerosol (haze) particles, respectively. Both scattering and absorption contribute to the extinction coefficient.

The laser we selected for jet exhaust measurements was a Nd:YAGx3 transmitting at 355-nm wavelength. Eyesafe operation was easy to achieve in the ultraviolet with simple precautions. The light is invisible, so there was no interference with pilot vision night or day. The 355-nm wavelength is also close to optimum for detecting the particles in the jet exhaust in the presence of scattering from molecules and from ambient particles. We used our OPAL (Ozone Profiling Atmospheric LIDAR, Fig. 2), but operated only with the "aerosol channel" (see Table 2 for specifications). The LIDAR could scan in elevation angle but had a fixed azimuth. The elevation angle precision was an order of magnitude better than at LAX, permitting measurements much closer to the surface than before. The elevation angle accuracy was somewhat less at $\approx 0.1°$. Real-time data displays helped the experimenters optimize sampling strategy, but raw data were recorded on Digital Audio Tapes (DAT).

Figure 2: LIDAR system for plume geometry and emission rate measurements. The enclosure on top contained the elevation-scanning mirror.

Data processing after the experiment used techniques previously developed for LIDAR and standard meteorological data to solve Eq. 8 to obtain $\beta_p(R)$. By scanning the elevation angle, i.e., the LIDAR's pointing direction; repeatedly up and down the cross-sectional profile of β_p was obtained in polar coordinates. These data were interpolated to a rectangular coordinate system in the scan plane. Fig. 3 shows a typical cross section from an aircraft with substantial particulate emissions. The MD88 started takeoff roll about 10s earlier, and the exhaust nozzles of its engines were $\approx$ 80 m away from the LIDAR's scan plane at the time of these measurements. The color scale shows calibrated plume signal above the signal from the ambient air in units of $Mm^{-1}sr^{-1}$, where Mm is megameters and sr is steradians.

Table 2: Specifications of LIDAR used to measure jet engine exhaust plumes

Parameter	Value
Wavelength	355 nm
Pulse energy	5 mJ
Pulse repetition rate	$10 \ s^{-1}$
Pulse length	10 ns
Range gate length	5 m
Telescope diameter	0.2 m
Elevation angle precision	0.02°
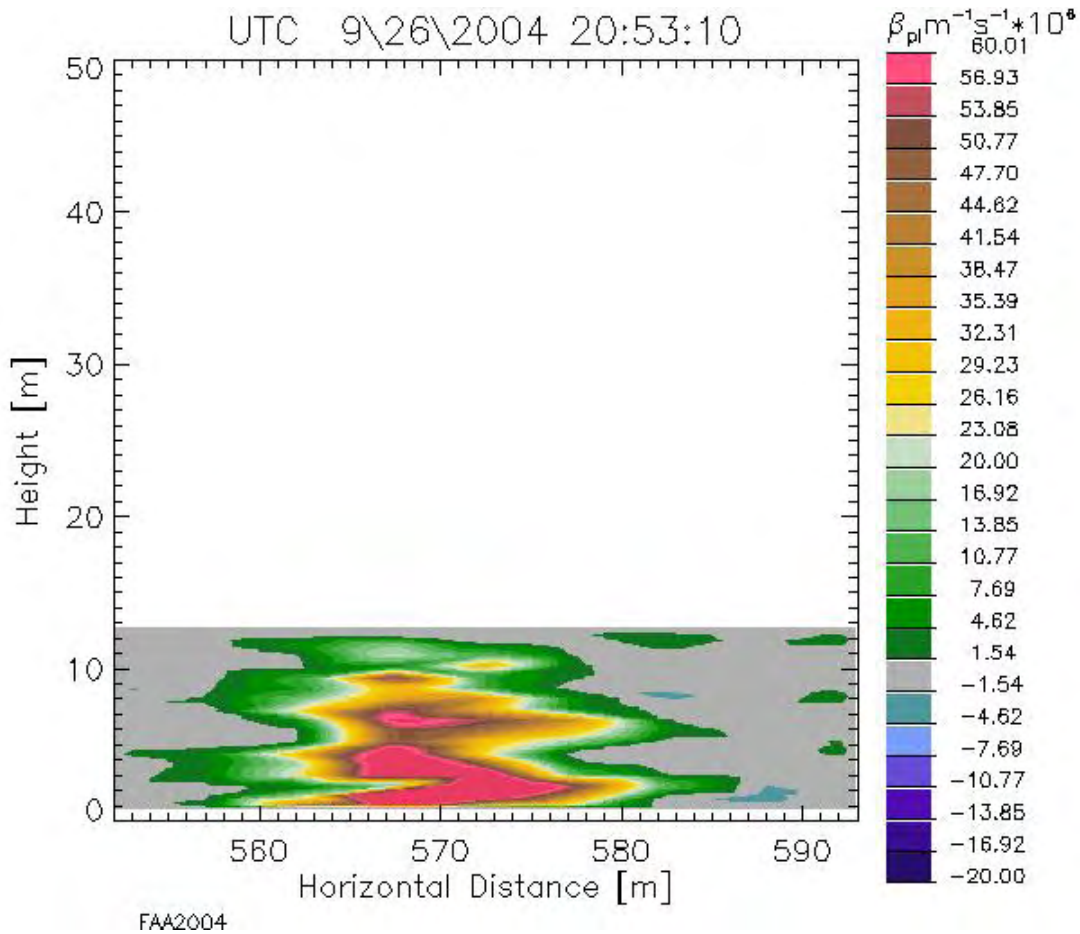
Figure 3: LIDAR cross section of an MD88's exhaust plume showing backscatter enhancement above ambient. The height is above the runway, the horizontal distance is measured from the LIDAR, and enhanced backscatter is given by the color scale. Time and date are UTC.

It is important to keep in mind the spatial resolution of the LIDAR while interpreting the data. The range or along-beam resolution, i.e., the horizontal resolution at the elevation angles typically used for plume measurements, is 5 m. The data system integrates all the backscatter received over each 5 m range gate. At the low elevation angles used for plume scans, the vertical resolution depends mainly on the vertical size of the beam spot. The spot size increased proportionally with range and was ≈ 0.1 m for the stationary tests (Fig. 4) and ≈ 0.2 m for the runway tests. The scans for the stationary tests were slow enough so that the vertical distance between beams at the plume was smaller than this resolution. However, when scanning more quickly for the runway tests, adjacent beams were ~1 m apart and the plume was only spot-sampled in the vertical.
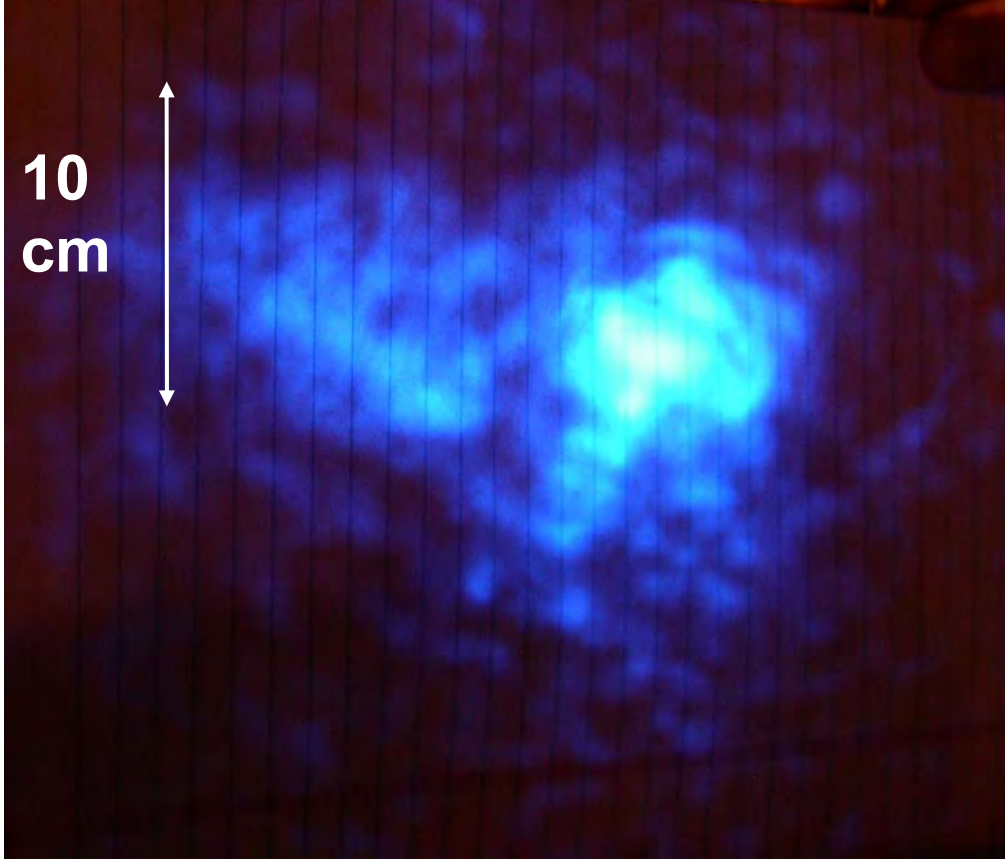
Figure 4: Fluorescence from tablet paper from one pulse of the ultraviolet laser at 300-m range. The mottled pattern is due mostly to optical turbulence, and changes from one pulse to the next.

For both stationary and runway measurements, the elevation angle scan rate was adjusted to take ≈ 5 s for each one-way sweep, so each sweep contained ≈ 50 pulses. At LAX the sweeps were half as long and typically included ≈ 25 pulses. The LIDAR's finer angle precision at UNA allowed finer measurements in elevation angle and measurements closer to the ground than at LAX.

2.3.2 LIDAR equation

The LIDAR equation for received signal for one pulse is:

$$X_0(r) = C \, E \, G(V) \, f(R) \, R^{-2} \, [\beta_m(R) + \beta_h(R) + \beta_p(R)] \, t_m^2(R) \, t_h^2(R) \, t_p^2(R) + B + EMI(R) + N(r), \tag{Eq. 9}$$

where:
X_0 = raw signal level
R = range (in discrete form, r is range to the middle of the gate)
C = lidar calibration constant, consistent with the units of E.

E = pulse energy monitor reading
G = PMT gain
V = PMT bias voltage
f = overlap function and any other non-signal dependent artifacts
β_m = backscatter cross section from molecules
β_h = backscatter cross section from haze particles, i.e., ambient aerosol
β_p = backscatter cross section from aircraft-generated particles (in humid cases where the exhaust causes a signal deficit by apparently drying the ambient aerosol, β_p will be negative)
t_m = one-way transmission due to molecular extinction = $\exp[-\int_0^R \sigma_m(R')dR']$
t_h = one-way transmission due to extinction by haze particles = $\exp[-\int_0^R \sigma_h(R')dR']$
t_p = one-way extinction due to the extinction by plume particles = $\exp[-\int_0^R \sigma_p(R')dR']$
B = background light and DC offsets in receiver
EMI = EMI (electro-magnetic interference) noise
N = Shot noise, Nyquist noise, and discretization "noise"

N from shot and Nyquist noise is random. The discretization noise, arising out of the fact the analog-to-digital converter has a finite number of digital steps, has the general effect of adding more uncertainty to the signal. However, discretization was a minor factor in the UNA-UNA data set, because analysis did not depend on ranges where the raw signal became very weak. One cannot correct for these random noise terms, but we try to keep them small compared to other imperfections in the data. They lead to noisy results, i.e., random peaks and valleys in the gridded data and the profiles, and beam-by-beam distortions therein due to noise in the fore- and post-plume regions.

The DC signal from any electronic offsets in the amplifiers and digitizer and from background light reaching the detector was measured by pre-triggering the data acquisition before the pulse was transmitted. For each pulse, the signal was averaged in range over the pre-trigger portion of the data to find B, and then B was subtracted from the signal at all ranges.

EMI was determined by acquiring data while a shutter was closed in front of the detectors. For step-stare data, e.g., for calibrations, EMI data were measured at the end of each elevation angle's stare. For RHI (Range Height Indicator, i.e., the traditional name for radar or LIDAR scanning in elevation angle at fixed azimuth) data on exhaust plumes, EMI data were recorded at the end of each file, but for practical reasons, the EMI data from the previous file were used to correct the LIDAR data from the atmosphere.

The G (V) relationship was found from a special test that was performed two times, with excellent agreement between the two. The LIDAR stared at zenith and the PMT voltage V was changed in steps. The signal change from the atmosphere at an appropriate range (beyond overlap and any saturation, but where SNR was still adequate), assuming the atmosphere wasn't changing, gave the relative functional relationship between V and G.

The calibration factor C was determined several times during the project using the "clean" layer reference method. The signal was measured from a layer in the upper

troposphere with evidence there of very little aerosol backscatter. The molecular backscatter is well known, giving the calibration point. The main complication is estimating the amount of aerosol extinction between the lidar and the clean layer. This was done using the Klett method, first with an assumed lidar ratio (extinction-to-backscatter ratio), and then fine-tuned using extinction coefficient estimates from slant path measurements and, in one case, optical depth measurements from a spectral sun photometer. Obtaining C for a known V, and having the change in G with V, gave the calibration factor C G (V).

$t_m(R)t_h(R)$ was obtained by assuming homogeneity of ambient aerosol backscatter along the beam when there was no aircraft plume present. By plotting the logarithm of the background- and EMI- corrected signal versus R and performing a least squares fit, the value of $\sigma_e = \sigma_m + \sigma_h$ was obtained. This process was done many times, because the haze extinction is always changing, usually in a gradual way.

$f(R)$ was determined using a similar method as for the ambient extinction, where the logarithm of the signal is linear at farther ranges where f=1, but the signal deviates from at closer ranges where f < 1. This was only for R < 325 m and was needed only for the stationary aircraft measurements.

The values of β_m and σ_m were calculated from airport measurements of pressure and temperature, giving air density, and the known molecular cross sections for backscatter and extinction at 355 nm. The β_h was found by averaging the backscatter in the fore-plume region (see next section) and subtracting the molecular component β_m .

It should be noted that these calculations assume the jet exhaust adds particles to the ambient air and no other modification. However, there are three probable deviations from this assumption:
1) The molecular and ambient aerosol backscatter (and less so, their extinction) may become smaller in the plume region because of the hot air from the exhaust, which makes the air and aerosol concentration less dense.
2) The ambient particles in the air that passed through the engine's combustion chamber are probably volatized.
3) In humid conditions, ambient particles mixing into the hot exhaust in the plume behind the aircraft might decrease in size as water evaporates from them. These factors have little effect on plume geometry measurements, but can contribute to the plume having no enhanced backscatter above ambient backscatter, or even a "negative" plume where backscatter from the exhaust is actually less than ambient backscatter.

2.3.3 Processing for Plume Geometry

This section describes the processing performed to obtain plume geometry measurements. This included solving the LIDAR equation for system and atmospheric effects and calibrating the LIDAR backscatter. Interactive editing was essential for quality control and to specify the region containing plume and the associated fore-plume and post-plume regions in order to extract dependable products for plume geometry and for soot emission rate estimates. Finally, we developed and applied automatic methods to calculate the plume's location and size from the data in digital form as displayed in Fig. 3. We did not obtain such plume parameters for LAX data; rather this was done interactively by Roger Wayson and assistants using displays as in Fig. 3, an option which can still be applied to the UNA-UNA data.

2.3.3.1 Region Selection and Pulse Screening

The data were presented to the operator in an RHI display (color-coded signal magnitude in polar coordinates of range and elevation angle) of each individual sweep of interest (Fig. 5). A sweep contains a set of contiguous pulses when the elevation angle changed from the bottom to top of a scan, or vice versa. Sweeps with inadequate data, e.g., plume not detected or plumes from two aircraft merging, were discarded from the data set.
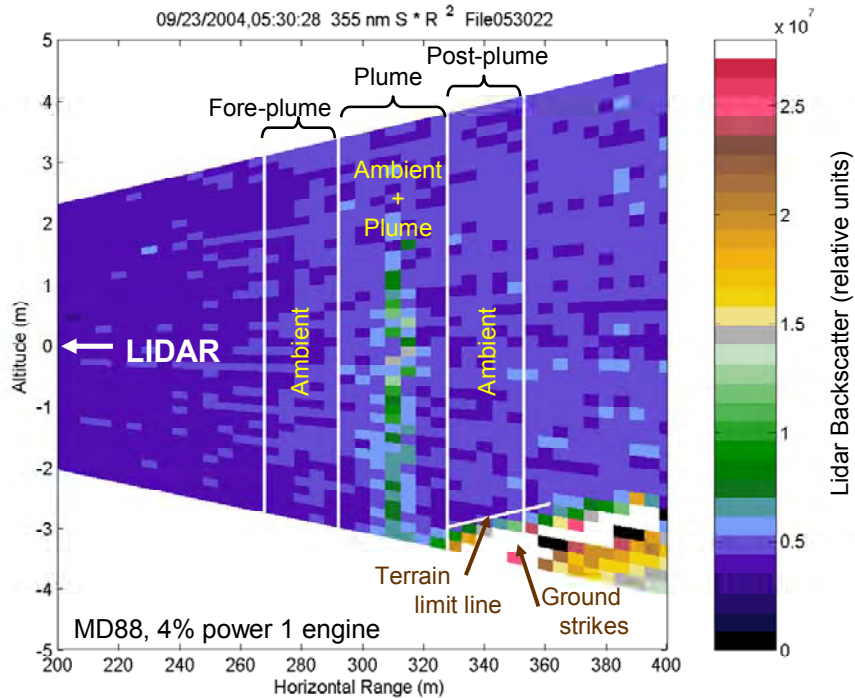
Figure 5: Example of a display for sweep selection and editing**

** The operator deleted several beams at the bottom of the sweep, eliminating them from the display, because they had ground signal in the plume or fore-plume region. The

operator also clicked four times with a cursor to position the four vertical white lines that define the three regions, and clicked twice with the cursor to define the terrain limit line.

The operator selected for each sweep 4 horizontal distances (Fig. 5) to define 3 regions: near or post-plume region (containing ambient air on the LIDAR side of the exhaust plume), plume region (containing the observable plume and a little bit of extra space), and the far or post-plume region (containing ambient air beyond the plume). The effects of along-beam variations in plume backscatter and extinction in the plume were accounted for by comparing beam-by-beam the average signal in the post-plume region with that in the fore-plume region. When they were unequal, the signal in the plume region was adjusted linearly with LIDAR range between the fore-plume and post-plume regions so as to make the average signal in the post-plume region equal to that in the fore-plume region. The data reported as plume backscatter were from within the plume region only.

The operator also flagged beams in each sweep that were excluded from the plume region in later processing. Beams at the bottom of the sweep were edited to prevent any contamination from the very strong signals from the ground. Pulses with any ground return within the fore-plume region were removed from the data set. The operator defined a straight, diagonal line, which marked the height below which there was some signal from the ground in the plume and post-plume region. The locus of the intersection of this line with the beam was calculated. When this point was within the plume region, the data in the plume region were not flattened, and the enhanced signal at range gates beyond the intersection were set to zero. When this point was within the half of the post-plume region nearest the LIDAR, there was no flattening, but the computed enhanced signal in the beam across the entire plume region was included. When this point was beyond the midpoint of the post-plume region, flattening was performed with the post-plume region shortened to the data before the terrain signal.

The operator also clicked the cursor in the display (not shown in Fig. 5) to direct later processing regarding the position of the top of the plume. Clicking on a beam below the top indicated that beams above it did not include any plume signal, excluding them from the final plume region data, and avoiding contamination there due to varying ambient aerosol. Clicking on the top beam included all the displayed beams in processing for plume data. Clicking in the white region above the sweep set a flag in the output indicating that the plume likely extended above the top of the sweep.

This interactive flagging of pulses allowed data to be processed much closer to the ground than at LAX and improved the accuracy of the plume results when the sweep extended much higher than the top of the plume. The interactive processing is labor intensive, but a necessary step to ensure dependable results for further analyses of plume geometry or emission rates.

2.3.3.2 2-D Interpolation from Polar to Rectangular Coordinates

The processed LIDAR data within the plume region were interpolated to a rectangular grid. The results are denoted by $s(y_i, z_j)$, where y is the distance from the LIDAR, z is the height above the ground and i and j are the horizontal and vertical array coordinates of the data, respectively. Grid coordinates refer to the center of the pixel of data. The grid element lowest in height and closest to the lidar is at y_0, z_0. The size of the array is N_y in the horizontal and N_z in the vertical, and the size $N_y \times N_z$ is varied to include the plume region. We chose fixed grid spacings of $\Delta y = 1$ m and $\Delta z = 0.1$ m for static tests and $\Delta z = 0.2$ m for runway tests. These were chosen to be smaller than the inherent resolution of the data, because otherwise the interpolation to y-z coordinates would smear the data to lower peak s and to larger geometrical size.

The coordinates of data up to the interpolation were relative to the LIDAR's scanner, which was on top of the trailer. We determined the height of the LIDAR scanner above the runway height (and tarmac height for static tests) based on LIDAR elevation angle with ground strikes at the runway's distance. This procedure also accounts for any small errors in setting the elevation angle encoder's absolute angle. The offsets were:

> Stationary tests 21-25 September 2004: 3.8 m
> Runway tests 26 September 2004: 3.2 m
> Runway tests 29 September, 2004: 3.3 m
> Runway tests 30 September 2004: 3.6 m

The data were adjusted for this offset immediately after the interpolation. The adjustment for LAX data as not done later in analysis by adjusting the plume height data. Data grid points from 2004 and later data are therefore height above the ground, whereas for LAX they were height relative to the scanner.

2.3.3.3 Plume Profiles

Based on the gridded plume data, vertical and horizontal profiles were calculated as follows and stored in ASCII files. The profiles are called marginal profiles, because they are calculated at the "margins" of the gridded array.

The horizontal profile is $S_h(y_i)$, given by

$$S_h(y_i) = \Delta z \sum_{j=0}^{j=N_z-1} s(y_i, z_j) \qquad \text{(Eq. 10a)}$$

The vertical profile is $S_v(z_j)$, given by

$$S_v(z_j) = \Delta y \sum_{i=0}^{i=N_y-1} s(y_i,z_j) \qquad \text{(Eq. 10b)}$$

Plume Parameters
The plume rise and size can be characterized by just a few parameters. There are a number of ways to calculate these, each with its advantages and disadvantages for particular situations and purposes. As is common practice, the horizontal and vertical profiles were used as a basis for these calculations. Several methods were used, which allowed comparison to see how representative they might be, allowing the user to choose the most appropriate. The experience gained in applying these methods to actual data, may eliminate, modify, or add to these schemes.

Geometrical or statistical parameters
The usual measures of plume position and size were calculated and archived. The total signal is the integral of the values in the gridded array, which is equal to the integral of either of the profiles. The position measurements are the mean for each of the vertical and the horizontal profiles. The standard deviations describe the size of the plume in the vertical and horizontal. We use N rather than N-1, where N is the number of elements in the profile vector, in the standard deviation calculation.

Equations for these parameters are given for calculations in the horizontal – the equations for vertical parameters are analogous.

The total signal is given by

$$S_T = \Delta y\, \Delta z \sum_{i,j=0}^{\substack{i=N_y-1 \\ j=N_z-1}} s(y_i,z_j) = \Delta z \sum_{j=0}^{j=N_z-1} S_v(z_j) = \Delta x \sum_{i=0}^{i=N_y-1} S_h(y_j) \qquad \text{(Eq. 11)}$$

The mean location in the horizontal is found from

$$y_{mean} = (\Delta y/S_T) \sum_{i=0}^{i=N_y-1} y_i\, S_h(y_i) \quad , \qquad \text{(Eq. 12)}$$

with a corresponding expression for z_{mean}.

The plume dispersion parameter is the standard deviation σ_{hor} of the plume profile found from the square root of

$$\sigma_{hor}^2 = (\Delta y / S_T) \sum_{i=0}^{i=N_y-1} (y_i - y_{mean})^2 \, S_h(y_i) \quad . \qquad \text{(Eq. 13)}$$

With noisy or uncontaminated data, σ_{hor}^2 can sometimes be negative. To handle this case and flag this condition, we used:

$\sigma_{hor} = (\sigma_{hor}^2)^{0.5}$ if $\sigma_{hor} \geq 0$; $\sigma_{hor} = -(1\sigma_{hor}^2)^{0.5}$ if $\sigma_{hor} < 0$.

By plugging the total, mean, and standard deviation values from the geometrical statistical values into the Gaussian equation, we have one form of a Gaussian fit to the data. The resulting Gaussian is given by

$$S_{ssh}(yx_i) = \frac{S_T}{\sqrt{2\pi} \, \sigma_{hor}} \exp\left[-0.5 \left(\frac{y_i - y_{mean}}{\sigma_{hor}} \right)^2 \right] \qquad \text{(Eq. 14)}$$

We computed two versions of an error statistic for this approximate Gaussian, and also for each of the other fits below. These error statistics will be important in deciding which fit method is the best. The first error statistic is the normalized average absolute difference between fit and data, given for the horizontal by

$$\varepsilon_{1ssh} = \left(\frac{\Delta y}{S_T} \right) \sum_{i-0}^{N_y-1} \left| S_{sh}(y_i) - S_h(y_i) \right| \quad , \qquad \text{(Eq. 15)}$$

where the subscript 1 denotes first-moment type of error statistic, and ss in the subscript stands for simple statistics.

The second error statistic is the square root ε_{2sh} of the normalized least square difference ε_{2sh}^2 between fit and data, which for the horizontal profile is given by

$$\varepsilon_{2ssh}^2 = \left(\frac{\Delta y}{S_T} \right)^2 \sum_{i-0}^{N_y-1} \left[S_{sh}(y_i) - S_h(y_i) \right]^2 \quad , \qquad \text{(Eq. 16)}$$

where the subscript 2 denotes second-moment type of statistic.

A similar substitution into a Gaussian was done for the vertical to obtain $S_{ssv}(z_j)$, and then ε_{1ssv} and ε_{2ssv} were calculated for the vertical with expressions analogous to the horizontal versions above.

Median and absolute deviation

The median is where half the signal in the profile is on each side. The median location y_{median} was found by integrating $S_h(y_j)$ from i=0 until reaching the first data point $i = I_{\frac{1}{2}}$) where the integral equals or exceeds $S_T/2$. Then, to be as precise as we can, we estimated the position within the cell where the exact ½ point is. In equation form, $I_{\frac{1}{2}}$ is found for the first i, starting with i=0, where

$$S_h' = (\Delta y/S_T) \sum_{i=0}^{i=I_{\frac{1}{2}}} S_h(y_i) \geq 0.5 \quad . \tag{Eq. 17}$$

The intracell correction is

$$\Delta y' = \Delta y \, (S_h' - 0.5) / [S_h(I_{\frac{1}{2}}) \, \Delta / S_T] . \tag{Eq. 18}$$

The coordinates are for the center of the grid cells, so the median horizontal location is

$$y_{median} = y_0 + \Delta y \, (0.5 + I_{\frac{1}{2}}) - \Delta y' \quad , \tag{Eq. 19}$$

with a corresponding expression for z_{median}. [If the coordinates were for the side of the cell near (opposite) the lidar, the factor 0.5 would become 1 (0).]

The corresponding dispersion parameter is the absolute deviation

$$d_{hor} = (\Delta y/S_T) \sum_{i=0}^{i=N_y-1} |y_i - y_{median}| \, S_h(y_i) \quad . \tag{Eq. 20}$$

The equations for z_{median} and d_{ver} are analogous to those just given for the horizontal.

The relationship between σ and d for a Gaussian is $\sigma = (\pi/2)^{\frac{1}{2}} d$. By plugging in the values S_T for the total, the median values instead of the mean, and $\sigma_{medh} = (\pi/2)^{\frac{1}{2}} d_{hor}$ and $\sigma_{medv} = (\pi/2)^{\frac{1}{2}} d_{ver}$ for the σ's, we produced another Gaussian approximation with S_T, y_{median}, σ_{medh}, z_{median}, and σ_{medv} as the Gaussian parameters. The error statistics were calculated similar to above, giving us ε_{1mdh}, ε_{2mdh}, ε_{1mdv}, and ε_{2mdv}.

Median and width to 68% of the signal

A method to obtain an approximate Gaussian fit similar to that with the mean and standard deviation but focusing more on the center of the profiles and with less dependence on the shape in the wings was to use the median as the center and assign the distance between the points that bracket 0.6826 of the total signal as 2σ. This is because the area between 1 standard deviation on each side of the center of a normalized Gaussian curve is 0.6826.

The value of total signal S_T and the locations of the medians y_{median} and z_{median} are the same as for the section on Median and Absolute Deviation.

Each marginal profile was integrated outward from each side of its median until the integral value reached $0.3413S_T$. The distances between these two points was considered to be 2σ. The equation for the integration from y_{median} toward y_0 was performed as follows (referring to the section on median and absolute deviation for some of the parameters already calculated there:

$$S_{near}' = S_T^{-1} \left\{ (\Delta y - \Delta y') S_h(I_{1/2}) + \Delta y \sum_{i=I_{1/2}-1}^{i=I_{near}} S_h(y_i) \geq 0.3413 \right., \qquad \text{(Eq. 21)}$$

where $I_{near} < I_{1/2}$. The intracell correction is $\Delta y_{near}' = \Delta y (S_{near}' - 0.3413) / [S_h(I_{near}) \Delta y / S_T]$. The equation for the integration on the far side of the median is:

$$S_{nearh}' = S_T^{-1} \left\{ \Delta y' S_h(I_{1/2}) + \Delta y \sum_{i=I_{1/2}+1}^{i=I_{far}} S_h(y_i) \right\} \geq 0.3413 , \qquad \text{(Eq. 22)}$$

where $I_{near} > I_{1/2}$. The intracell correction is $\Delta y_{far}' = \Delta y (S_{farh}' - 0.3413) / [S_h(I_{far}) \Delta y / S_T]$. The equivalent value of σ_{68h} is

$$\sigma_{68h} = 0.5 [(I_{far} - I_{near} + 1)\Delta y - (\Delta y_{near}' + \Delta y_{far}')]. \qquad \text{(Eq. 23)}$$

A corresponding expression for σ_{68v} was calculated using z_{median}, $J_{1/2}$, z_0, Δz, and $\Delta z'$ instead of y_{median}, $I_{1/2}$, y_0, Δy, and $\Delta y'$, respectively.

By plugging into the Gaussian equation the values S_T, x_{median} instead of the mean, and σ_{68h} for the standard deviation, we have another approximate fit in the horizontal, and similarly in the vertical using S_T, z_{median}, and σ_{68v}. The error statistics were calculated similar to above, giving us ε_{168h}, ε_{268h}, ε_{168v}, and ε_{268v}.

[An additional approximate Gaussian fit could be added by increasing the 68% to 90% (1.645 standard deviations) or 95.4% (2 standard deviations). Or, if one of these more inclusive fits is found to better, it could replace the 68% fit. The algorithm would be the same, except 0.3413 would be replaced by 0.90 (for 90%) or 0.4722 (for 95.4%).]

Peak and tenth of peak

In processing data from LAX, Roger Wayson viewed the false-color 2-D GIF images and used the location of the peak signal as the "center." He subjectively determined where the signal dropped (sometimes sharply) to a low value and used that as a width marker. He assumed the distance from the location of the peak to this width marker was equivalent to a Gaussian from the center to where the signal declines to 10% of the center or peak

value. This distance is $2.146\sigma \approx 2.15\sigma$. It is very hard to automatically mimic his approach. However, we applied one scheme which is based on the concept of finding the peak and the point where the profile drops to 0.1 of the peak value. This scheme found the peak in each of the horizontal and vertical profiles instead of the location of the peak value of $s(x_i,z_j)$ in the 2-D array as Roger did. Also, this scheme finds the actual location where the signal drops to 10% of the peak value, instead of judging this location by eye.

For the horizontal profile, we used the IDL max tool to find $S_{hmax}(i_{max})$, which returns the maximum value and, with the max_subscript option, its array index i_{max}. The location of the peak is thus at $y_{peak} = y_0 + \Delta y \, i_{max}$. We then searched the array from the i=0 end and found the first time $S_h(i) > 0.1 \, S_{hmax}$, noting the index $i_{neartenth}$. Next we searched the array from $i=N_y-1$ and found the first time $S_h(i) > 0.1 \, S_{hmax}$, noting the index $i_{fartenth}$. Assuming the crossing of the 0.1 value was midway between array points, we calculated the equivalent Gaussian width according to $4.92\sigma_{pth} = (i_{fartenth} - i_{neartenth}+1)\Delta y$, or $\sigma_{pth} = (i_{fartenth} - i_{neartenth} +1)\Delta y/4.92$. The subscript pt refers to peak-tenth.

The analogous calculations were performed on the vertical profile to obtain S_{zmax} , z_{peak} , and σ_{ptv}.
A Gaussian-shaped estimate was found from these parameters. Since the peak of the horizontal (vertical) profile is S_{hmax}, the corresponding value for total signal for substitution into the equation is $S_{Tpth} = (2\pi)^{\frac{1}{2}} \sigma_{pth} S_{hmax}$. For the vertical, $S_{Tptv} = (2\pi)^{\frac{1}{2}} \sigma_{ptv} S_{vmax}$, which in general is not the same as S_{Tpth} . The parameters defining the equivalent Gaussian profile are therefore S_{Tpth} , y_{peak} , and σ_{pth} substituting for S_T , y_{mean} , and σ_h , respectively. A fit was similarly made in the vertical. The error statistics ε_{1pth} , ε_{2pth} , ε_{1ptv} , and ε_{2ptv} were calculated, using the S_T from the data rather than S_{Tpth} or S_{Tptv} to normalize.

Least-squares fit of a single Gaussian to extended profile

The plume horizontal and vertical profile can also be characterized by fitting a Gaussian shape to the profile based on minimizing the least squares difference between fit and data. This works well for profiles with approximately Gaussian shape, but can become unstable if the shape deviates strongly. When the profile shape is very different than a Gaussian, or signal-to-noise is very poor, the plain Gaussian fit to the data can give erroneous and even unphysical results. For example, for a uniform profile, the Gaussian fit will have dispersion parameter approaching infinity. For a profile monotonically decreasing with height, the Gaussian fit will have mean height below the surface. In order to constrain the width of the fit in such situations, we extend the marginal profiles in the horizontal and the vertical on both sides with values of zero. We choose to enlarge the size of the horizontal array to approximately double the original size, with $N_y/2$ elements (rounded down to the nearest integer) added on each side, so the new array has size $N_y' = 2 N_y$ if N_y was even and $N_y' = 2 N_y-1$ if N_y was odd. The distance to the new first element in the array is $y_0' = y_0 - 0.5(N_y' - N_y)\Delta y$, and $S_h(y_i) = 0$ is assigned to each new element. The vertical array is increased in size in similar manner using N_z , z_0, Δz. The new elements at the ends of the array are assigned a value $S_v(z_j) = 0$. GAUSSFIT was used to

fit the data in the extended horizontal and vertical profiles. The equation for the parameters is, for a horizontal profile,

$$S_{Gh(ext)} = \frac{S_{TGh(ext)}}{\sqrt{2\pi}\ \sigma_{Gh(ext)}} \exp\left[-0.5\left(\frac{y - y_{Gh(ext)}}{\sigma_{Gh(ext)}}\right)^2\right],\qquad \text{(Eq. 24)}$$

GAUSSFIT was also run for the vertical profile, obtaining $S_{TGv(ext)}$, $z_{Gv(ext)}$, and $\sigma_{Gv(ext)}$.

The error parameters between the fit and the data were calculated as above. The resulting error parameters are $\varepsilon_{1Gh(ext)}$, $\varepsilon_{2Gh(ext)}$, $\varepsilon_{1Gv(ext)}$, and $\varepsilon_{2Gv(ext)}$, using the S_T from the data rather than $S_{TGh(ext)}$ or $S_{TGv(ext)}$ to normalize. These error statistics are calculated using only the original N_y or N_z data points.

Double Gaussian fit in the horizontal – future

Aircraft with wing-mounted engines often produce horizontal profiles with two peaks. A double Gaussian has potential for a much better fit to the horizontal profiles. We hope in the future to develop an *ad hoc* fitting scheme to produce this product.

The algebraic expression for this double Gaussian is

$$S_{DG} = \frac{0.5\ S_{TDGh}}{\sqrt{2\pi}\ \sigma_{DGh}}\left\{\exp\left[-0.5\left(\frac{y - y_{DGh1}}{\sigma_{DGh}}\right)^2\right] + \exp\left[-0.5\left(\frac{y - y_{DGh2}}{\sigma_{DGh}}\right)^2\right]\right\}\quad \text{(Eq. 25)}$$

Error parameters of fit compared with data would be defined as ε_{1DGh}, ε_{2DGh}, using the S_T from the data rather than S_{TDGh} to normalize.

We attempted to do this with the IDL LIMFIT and CURVFIT functions, but found that the nonlinear fit iteration rarely converged. The output was not removed from the data set, so results are flagged as bad.

Least-squares fit of a single Gaussian to vertical profile without extension

We also fitted a Gaussian equation to the vertical profile without extending on both sides with zero data values. The purpose was to provide an indication of how much the profile deviated from a Gaussian shape. If the data formed a full Gaussian curve, the two results would be nearly identical. If the profile was not Gaussian, e.g., a vertical profile in the shape of half a Gaussian with maximum at the surface and decreasing monotonically with height, the fit with extended data would have a positive mean height and the fit without extension would have mean height at zero and a larger standard deviation. The

parameters are defined as for the Gaussian fit to the extended profile, except the (ext) in the subscript is dropped.

Folded Gaussian fit in the vertical – future

Vertical profiles of pollutants released near the ground typically have a shape much closer to a folded Gaussian than a simple Gaussian. The concept is that the turbulence mixing "reflects" at the surface. The expression, which has 3 varying parameters, is

$$S_{FG} = \frac{S_{TFGv}}{\sqrt{2\pi} \, \sigma_{FGv}} \left\{ \exp\left[-0.5 \left(\frac{z - (z_{FGv} - 0.5\Delta z)}{\sigma_{FGv}} \right)^2 \right] + \exp\left[-0.5 \left(\frac{z + (z_{FGv} - 0.5\Delta z)}{\sigma_{FGv}} \right)^2 \right] \right\}, \qquad \text{(Eq. 26)}$$

where, if z is the height above the ground, the folding or "mirror" height (the surface) is at $z_{FG} - \Delta z/2$ when the z coordinate applies to the center of the grid cell.

We attempted to use IDL's LMFIT and CURVEFIT functions, but failed to obtain convergence. We hope in the future to develop an *ad hoc* method to perform these fits.

Negative plume

If $S_T < 0$, then we have a "negative plume," "subambient plume," or "void" case. One can still process the data, and the above plume parameter relationships are still be valid.

Parameters related to optical extinction

The plume-total inferred extinction through the plume is given by:

$$T_p = \Delta z \sum_{j=0}^{j=N_z-1} \tau_p(z_j) \quad . \qquad \text{(Eq. 27)}$$

The associated plume-average extinction-to-backscatter ratio L_p is given by

$$L_p = T_p / S_T , \qquad \text{(Eq. 28)}$$

where S_T is from the data and not from any of the fits.

Plume Parameter Outputs

The plume parameters with associated aircraft information are provided on a CD accompanying this report. Data are stored in EXCEL files, one for each of the three experimental days, named as xxSeptember2004_FinalReport.xls, where xx is the day of the month. The results for one sweep are listed on one row and sweeps in chronological order. The first two rows are headings with parameter and physical units where applicable. They headings are similar to the algebraic parameters listed in this document. The key for these columns is given in more detail in the UNAPlumeParameterKey_FinalReport.xls file on the CD.

All times and dates in this report are UTC. For local time (EDT) subtract 4 hours, and for EST subtract 5 hours.

Comments on Plume Parameters

For plumes possessing strong signal and a full Gaussian shape, the plume parameters using the several methods are similar. However, when profiles of backscatter deviate from these conditions, differences do occur among the methods, sometimes severely. The choice of which method is best for a particular parameter depends on the goal in using the parameter and on how well the inferred profile fits the data. The ε parameters indicate the goodness of fit. The ε_1 parameters are believed better to use, because compared to ε_2 parameters they are less sensitive to outliers, depend less strongly on noise, and depend more strongly on differences between the shapes of the data profile and the inferred fit.

For total signal in the plume the S_T parameter is recommended as the simplest and most direct. The total signal derived from other methods will depend on the shape of the fitted profile and hence is less dependable for this purpose. The soot emission rate calculations use S_T.

The geometrical or statistical parameters (subscript ss) for plume center location use the traditional statistical method, but given the noisiness of the data, are probably not as robust as the median method. Likewise, the plume size estimates using the geometrical or statistical parameters are sensitive to noise and nonsmooth behavior at the ends of the profiles. The absolute deviation or 68% of total signal methods should be more robust and preferred.

The peak and distance to 1/10 of peak method is closest to the interactive method used for the LAX data, but is not expected to be very stable. I recommend against using it routinely.

The Guassian fit to extended profile simulates most closely what most people would do if they were to hand-draw a Gaussian curve to fit the data.

The Gaussian fit to the nonextended vertical profile should not be used for its plume parameters, but rather was included only as an indication of how non-Gaussian the profiles are by comparing it to the Gaussian fit with extended profiles.

With a goal of determining plume rise and plume size as input to a dispersion model, the best choice should generally be from among the two median methods and the Gaussian fit with extended profile method. Perhaps an optimum method would be to check the ε_1 values for each sweep for these three methods and use the plume location and size from the method with the smallest ε_1.

Sometimes when profiles are very noisy due to weak signal or have convoluted shapes, the plume parameters become unphysical, e.g., negative width parameters or possessing impossible plume locations. We have not screened out such examples, so the user of the data must define and apply acceptable criteria. Lessons learned from such screening might be applied automatically to data processing in the future.

2.3.4 Basic Method for Measuring Soot Emission Rates

The basic method to determine soot emission rates is the LIDAR measures the flux F of soot through a perpendicular plane scanned by the LIDAR behind the aircraft. For a stationary aircraft and assuming particle mass is conserved between the exit nozzle and the scan plane, the emission rate $Q = F$. The pulsed LIDAR measures optical backscatter β as a function of range along the beam. By scanning in elevation angle the distribution $\beta_p(y,z)$ in the scan plane is obtained and extracted as described above. The distribution of soot mass concentration c is computed from $c = \eta\,\beta_p$, where η is found using scattering calculations as described below. The experimental layout and coordinate system for test measurements at UNA-UNA is shown in Fig. 6. The flux for this situation is given by

$$F = \iint_{y,z} c(y,z)\, v_x(y,z)\, dy\, dz \qquad\qquad \text{(Eq. 29)}$$

where, v_x is the component of air velocity in the direction perpendicular to the scan plane. The y-z extent of c and v_x increase downstream as the exhaust mixes with ambient air.

According to our funding agreements with University of Missouri-Rolla and the Department of Transportation VOLPE Center, one or both were to provide us with the plume velocity profiles at the location of the LIDAR scan plane. The search of literature and reports made by the latter were not successful. The website of Boeing Aircraft Company shows contour plots of velocity and temperature behind some of their aircraft, but the purpose is for safe ground operations and the values appear to be extremes rather than the means needed for the flux calculations. We had also hoped an engine or aircraft manufacturer might have models that would suffice. These hopes all proved to be vain, forcing us to consider other approaches. After much thought and discussion with Roger Wayson and some checking in the literature on high Reynolds number jets, we

determined that a theoretical approach based on simple physical principles and engine specifications would suffice. The simplicity of this approach actually proves to be an advantage.

We instead estimated v_x (y, z) by applying conservation of mass and momentum, meaning the velocity "plume" had the same shape and cross-sectional area as $c(y, z)$. The effects of the ambient wind can be neglected for measurements so close behind the engines. The equation for the flux then becomes

$$F = \frac{Th}{Q\rho_{amb}} \iint_{y,z} [c(y,z)]^2 \, dy\,dz \quad , \tag{Eq. 30}$$

where:
Th = engine thrust (i.e., the momentum of the exhaust air generated by the engine)
ρ_{amb} = density of the ambient air.

The LIDAR measured the area integral of c using η, Th was determined from engine specifications and power setting, and ρ_{amb} was calculated from airport temperature and pressure data. Details of the measurements and theory for determining emission indexes are described in the next section.
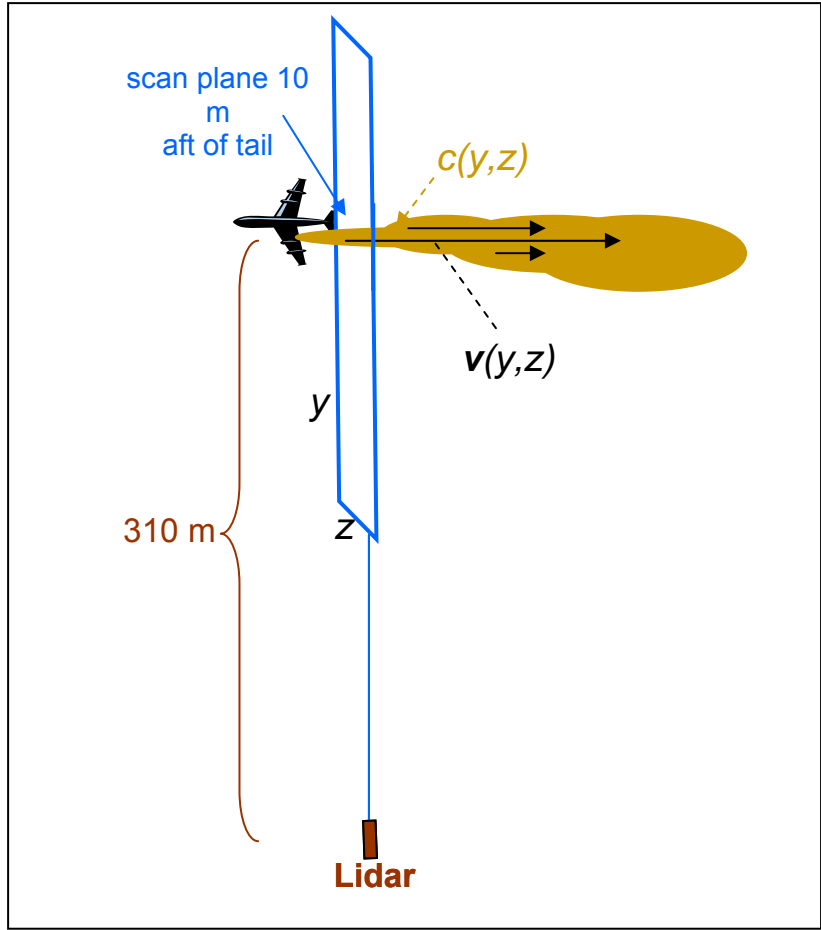
Figure 6: Experimental layout for trial soot emission measurements by LIDAR from a stationary aircraft with one engine operating. For higher power settings of wing-mounted engines, the starboard engine was also operated at equal or less power than the primary engine on the port side.

For tail-mounted engines with the plume still separated from the surface, the LIDAR system measured the plume's vertical profile (Fig. 7 left frame) and the horizontal profile was assumed the same, i.e., $\sigma_y = \sigma_z$. The LIDAR's vertical resolution is much better than the horizontal resolution, and the horizontal width close behind the engine couldn't be resolved. For a single, wing-mounted engine, the plume was in close contact with the ground and had an asymmetric profile, for which we assumed more width than height, i.e., $\sigma_y = 2\sigma_z$. At higher throttle settings, both wing-mounted engines had to be running (Fig. 7 right frame), so the output from just one engine was calculated from the data for two engines.

Static Test Plume Cross Section Examples – Strong Backscatter

JT8D-219 -- Tail Mount One Engine -- 100% Power	PW2037 – Wing Mount Two Engines – 70% Power

Vertical profile is ≈ Gaussian

Vertical profile is ≈ ½ Gaussian

assume $\sigma_y = \sigma_z$	**assume σ_y = 2 x full-Gaussian σ_z**
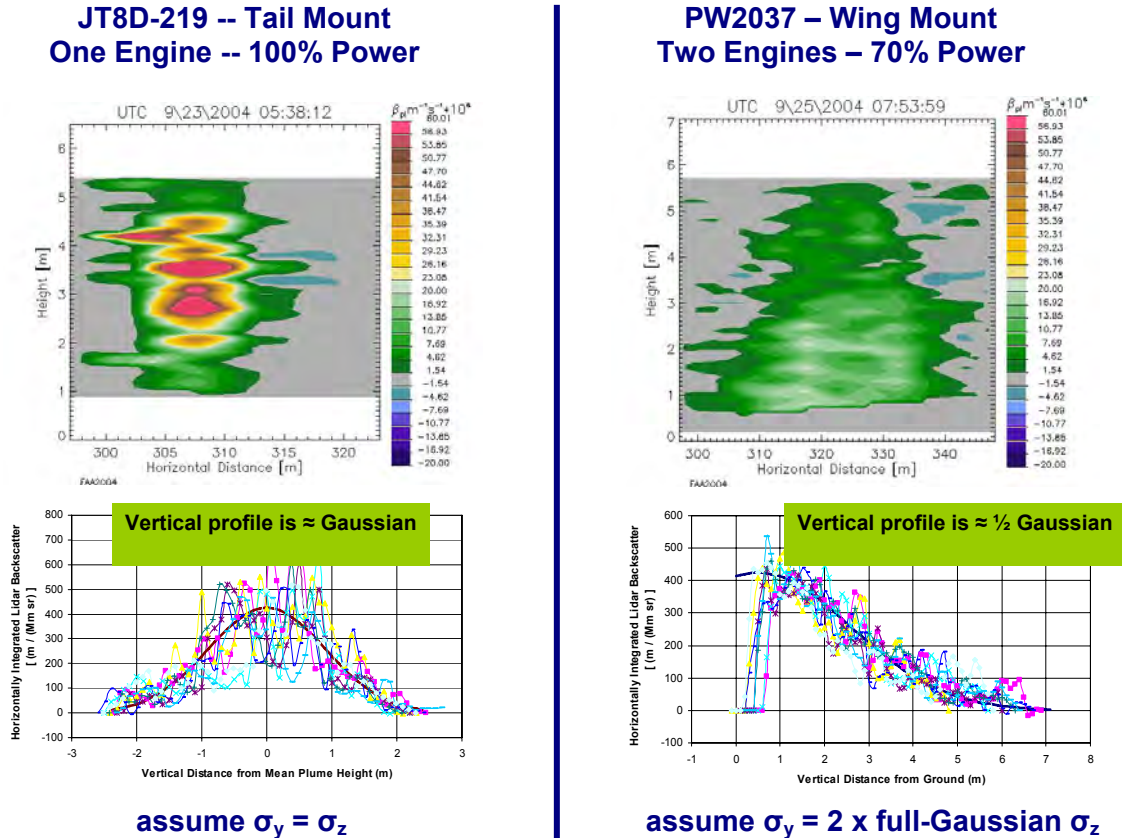
Figure 7: Difference during Single Engine and Two Engine Testing

2.3.5 Mass from Backscatter

The relationship between the observed plume backscatter and the mass concentration of soot (total aerosol) is given by

$$c = \eta\,\beta_p \qquad\qquad\text{(Eq. 31)}$$

where the units we use are g m^{-3} for c, m^{-1} sr^{-1} for β_p, and g sr m^{-2} for η. Scattering calculations or measurements in controlled conditions are required to determine η accurately. For this initial attempt at soot measurements we chose a simple and convenient method to calculate η. We elected to apply Mie scattering theory and the volume mixing rule, which are often used, and produced the data in Fig. 9. Because soot particles are decidedly nonspherical, the limitations of these assumptions must be kept in mind. The refractive index and density of soot must be known for these calculations. After reviewing the literature, which reports a variety of refractive index values, many without the associated data on particle density, it was decided to follow Horvath (1993). Lognormal size distributions were assumed, which are widely reported in the literature as describing jet engine particles, and calculated for a variety of mass geometric mean

diameters and particle density using the volume mixing rule. In consultation with Roger Wayson and Rick Miake-Lye a particle density of 1 g cm^{-3} was assumed for this project. Based on the literature, a typical value of 0.07 μm for the mass geometrical mean diameter was assumed. This gave $\eta = 9.35$ g sr m^{-2} (Fig. 19).
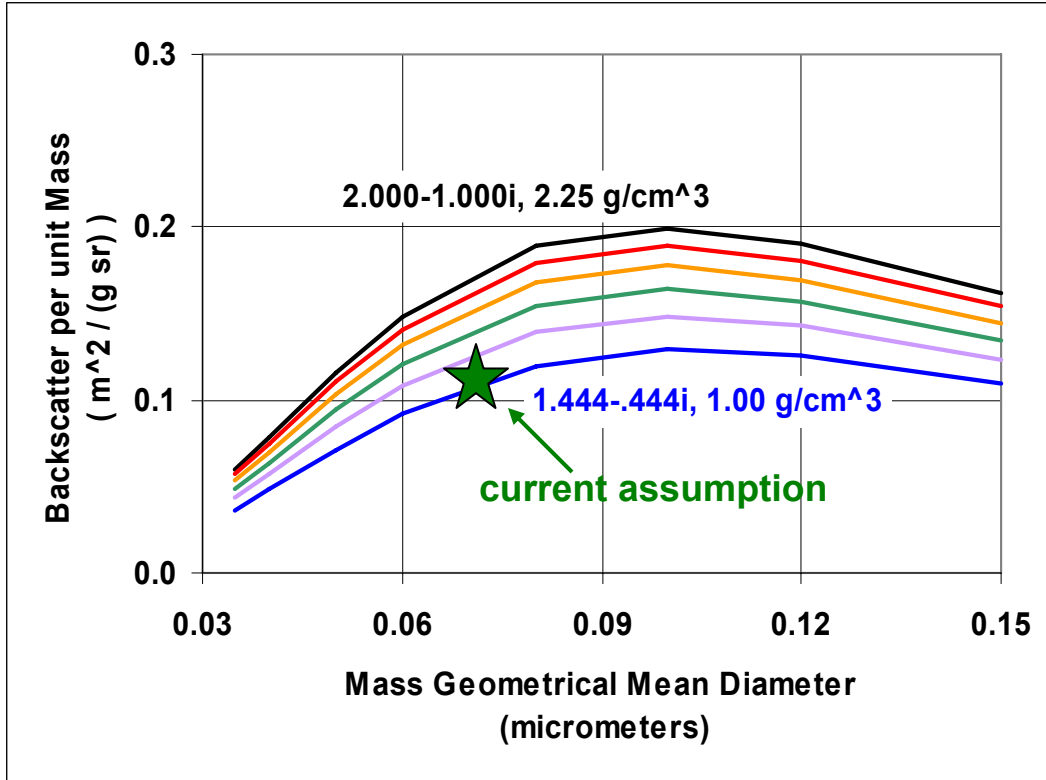
Figure 8: LIDAR backscatter per unit mass of soot (η^{-1}) at 355-nm wavelength versus geometrical mean diameter for lognormal size distributions of spherical soot particles with geometrical standard deviation of 1.65 at the indicated values of particle density and associated refractive index using the volume mixing rule. The unlabeled curves are for steps in density of 0.25 g cm^{-3} and corresponding changes in refractive index.

2.3.6 Engine Parameters

The data and calculation to determine the values of *Th* and other parameters for each engine and power setting are listed in the StaticEngineParameters.xls file on the CD, and calculations for power settings for each stationary aircraft are in the "Eng" worksheets in the aircraft files.

ICAO data on fuel flow (*FF*) were available at 7, 35, 80, and 100% throttle for each engine, and were interpolated and extrapolated to the other power settings experienced during the tests. Thrust at 100% throttle was obtained from ICAO, and air mass flow Φ_0 through the engine at 100% was obtained by George Noel from the Jane's data base.

Thrust was assumed proportional to throttle setting, an assumption verified by industry experts as very reasonable. Velocity of air at the exit nozzle was calculated from

$$v_0 = Th / \Phi_0 \qquad \text{(Eq. 32)}$$

at 100% throttle. Both mass flow and velocity at the exit nozzle were assumed to vary with the square root of the thrust, ie., Eq. 25 holds at power settings below 100% with the proportionality between v_0 and Φ_0 constant. The temperature of the air exiting the nozzle was calculated from the net heat of combustion of the fuel $H_c = 43.2 \times 10^6$ J kg^{-1} (which is a typical value), the fuel flow rate, and assuming all the energy not used for accelerating the air mass flow through the engine increased the temperature of the exhaust. The equation for temperature increase above ambient is

$$\Delta T = \left[FF\, H_c - 0.5\Phi_0 v_0{}^2 \right] / \left[\Phi_0 c_p \right] , \qquad \text{(Eq. 33)}$$

where ΔT is in °C or °K and $c_p = 1005$ J kg^{-1} °K^{-1} is the specific heat of dry air at constant pressure. The values of bypass ratio BPR, also used in the emission index calculations, was obtained from the ICAO data base.

The accuracy of these calculations could be checked if good measurements were performed of exhaust temperature and velocity at the *in situ* probe used in the tests.

2.3.7 Emission Index from Enhanced Backscatter

The emission index derived from Eq. 23 assuming a Gaussian profile in both vertical and horizontal directions for concentration (and velocity) is

$$EI_{enh}\,(g\,/\,kg) = \frac{\eta B}{FF} \left[\frac{Th}{4\pi\sigma_y \sigma_z \rho_{amb}} \right]^{1/2} \qquad \text{(Eq. 34)}$$

where
$\eta =$ the inverse of the mass backscatter LIDAR efficiency $= c/\beta$
$c =$ soot concentration (g/m^3)
$Th =$ thrust
$FF =$ fuel flow rate
$Pamb =$ ambient air density
$\sigma_y, \sigma_z =$ standard deviation of c(y,z)

B is the enhanced backscatter integrated over the cross section of the plume

$$B = \iint_{y,z} \beta_p (y,z)\, dy\, dz . \qquad \text{(Eq. 35)}$$

For the half Gaussian in the vertical, the 4π changes to $2\pi/(1\text{-}2/\pi)^{1/2}$ which is 17% smaller than 4π. Eq. 34 was first derived assuming constant velocity and air density across the exhaust nozzle. It was derived again assuming the core and bypass air were separated and had different velocities, with the same result. The derivation was also performed assuming higher pressure at the exhaust nozzle than ambient, but when the plume was allowed to expand perpendicular to the axis, which it will quickly do, the result was as listed in Eq. 34. As mentioned above, the derivation applies conservation of mass and momentum, which are fundamental principles in high speed jet theory (Schlichting and Gersten, 2000). Thus, Eq. 34, with 4π or other appropriate form factor depending on plume shape appears to be robust as well as simple.

The EI_{enh} results from the experiment are listed in the "Emit" worksheet (column AI) for each aircraft.

This equation assumes the engine adds soot to the air and does not otherwise alter the LIDAR scattering properties of the air passing through the engine. However, there are changes, which are discussed and accounted for in the next section.

2.3.8 Adjustments to Emission Index for Secondary Effects

Three physical effects in the plume will alter the measured backscatter and the emission index. One is the destruction of ambient particles in the extremely hot air passing through the core of the engine where the fuel is burned, causing a loss of backscatter. A second is the dilution of the air density, because the plume is warmer than ambient, which also decreases backscatter. The third is loss of adsorbed water from particles in the bypass air and also as the exhaust mixes with particles in the ambient air, also causing a decrease in backscatter. The proof that these type of mechanisms occur is that the LIDAR has observed a "negative" plume, i.e., the signal where the plume should be was consistently less than ambient, on a number of occasions, particular when humidity was high. In fact, slightly negative plumes were observed at some power settings during the stationary tests, but not nearly as dramatic as some runway examples, particularly at LAX. A theory accounting for the first two is described next. Funding limitations have required postponement of theoretical examination of the loss of adsorbed water for future research.

The current assumption is that all the ambient particles passing through the engine core are volatized to gas, and all particles in the bypass air are unchanged. The amount of soot that compensates to make up the LIDAR backscatter difference from ambient is

$$EI_{vol} = \frac{\eta \beta_h \Phi_0}{FF\, \rho_{amb}(1+BPR)} \quad .$$
(Eq. 36)

33

The amount of soot required to make up the LIDAR backscatter lost due to warm and hence lower density plume is

$$EI_{\Delta T} = \frac{\eta(\beta_m + \beta_h)\Phi_0}{FF \, \rho_{amb}} \left[\frac{\Delta T}{T + \Delta T} \right] \left[1 - \left(\frac{\beta_h}{(1 + BPR)(\beta_m + \beta_h)} \right) \right] .$$ (Eq. 37)

The results of the sum of these two adjustments are listed in the aircraft spreadsheets in column AL of the "Emit" worksheets on the CD.

A review of the meteorological data suggests that recirculation could also be a cause for some of occurrences of these negative plumes. The recirculation of particles in the area, which perhaps were larger after cooling and coagulation, presented a better "target" for back scatter.

3.0 Results and Discussion

3.1 Dedicated Engine Tests

The complete reduced dataset for the UMR and ARI component of the dedicated engine tests can be found in the attached spreadsheet – Engine Test Analysis – For Archive.xls. These data are summarized as a series of five plots associated with each airframe/engine studied and these represent the variation in parameters mentioned earlier as a function of engine power conditions.

3.1.1 Physical Characterization Results

Gas turbine engine emissions are influenced by engine power settings and ambient conditions at the engine inlet. Fig. 9 shows typical particle size distributions as a function of engine power acquired at the engine exit plane (1m) (Lobo et al., 2007). The mean diameter of the particle size distribution shifts to larger size as the engine power setting is increased. For discussions of the influence of test operating conditions on the exhaust aerosol, it is convenient to represent the size distributions with characteristic parameters: number based geometric mean diameter (Dgeom), geometric standard deviation (Sigma), mass based geometric mean diameter (DgeomM), and total concentration; and the derived parameters: number-based emission index (EIn) and mass-based emission index (EIm). All data presented here has been acquired using the DMS500 and has also been corrected for line loss using the function shown in Appendix B.
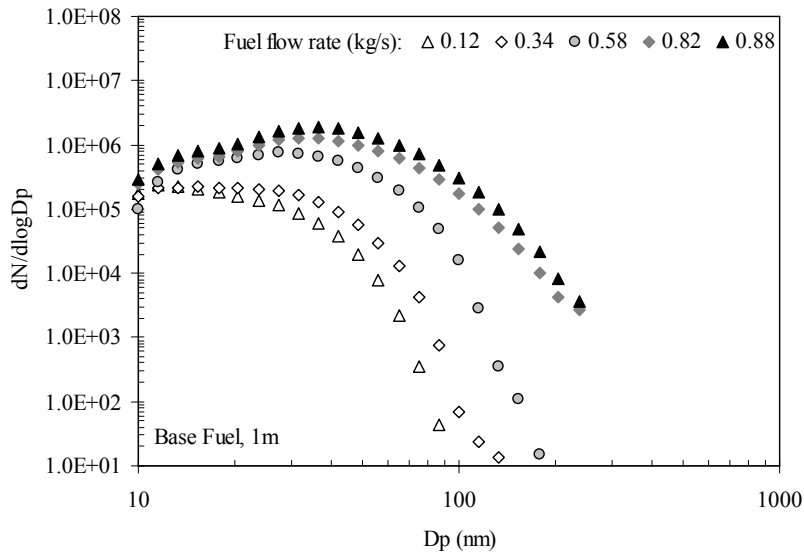
Figure 9: Typical particle size distributions acquired at the engine exit plane (1m)

Figs. 10-15 represent the variation of a given aerosol parameter as a function of engine power setting, for each engine studied.

A/C # 908 – Aircraft: MD-88, Engine: JT8D-219

Dgeom (nm) vs. Power
Aircraft: MD-88   Engine:JT8D-219

908

Sigma vs. Power
Aircraft: MD-88   Engine:JT8D-219

908

Dgeom M (nm) vs. Power
Aircraft: MD-88   Engine:JT8D-219

908
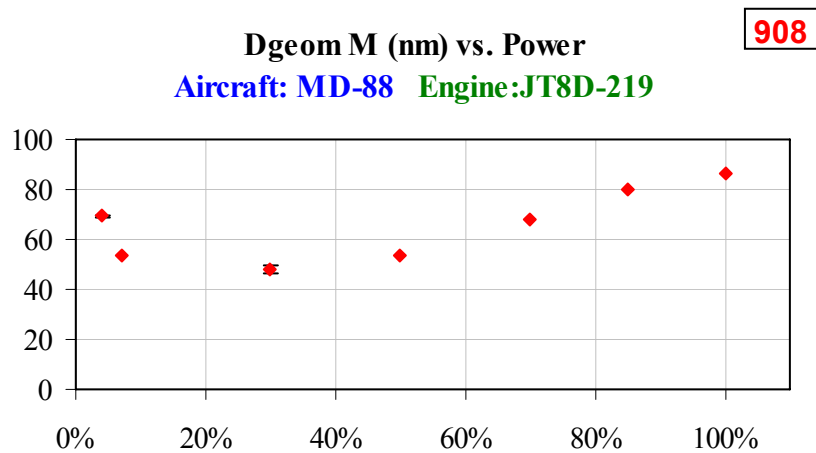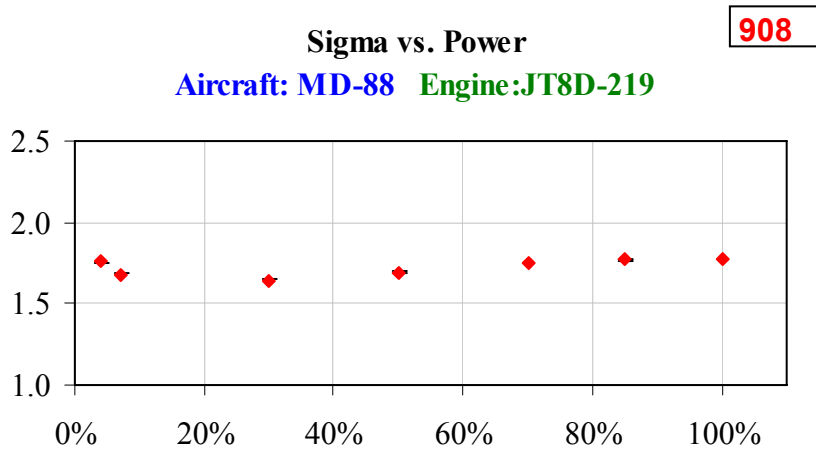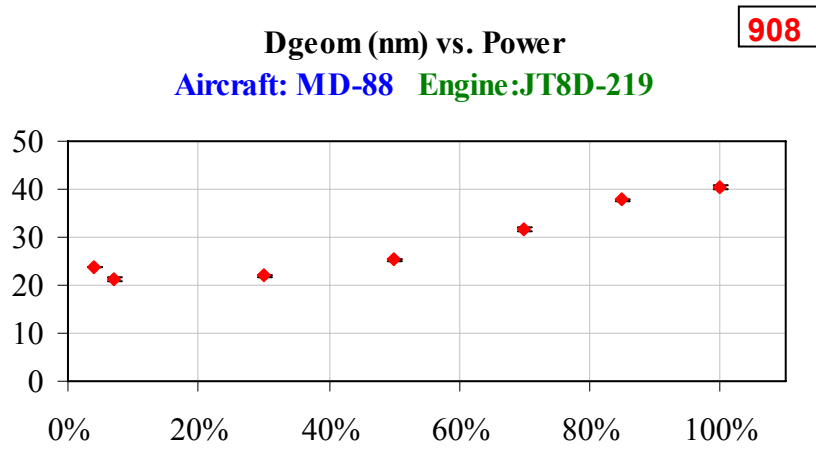
Figure 10a: Engine Emissions Parameters as a Function of Engine Power for AC # 908

EIn (1e15/kg_fu) vs. Power
Aircraft: MD-88   Engine:JT8D-219

908
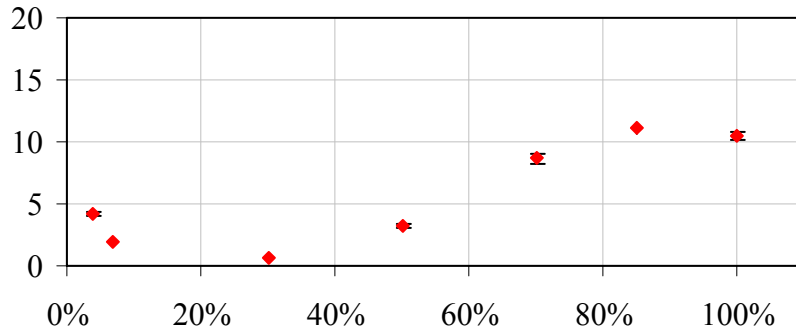
EIm (g/kg_fu) vs. Power
Aircraft: MD-88   Engine:JT8D-219

908
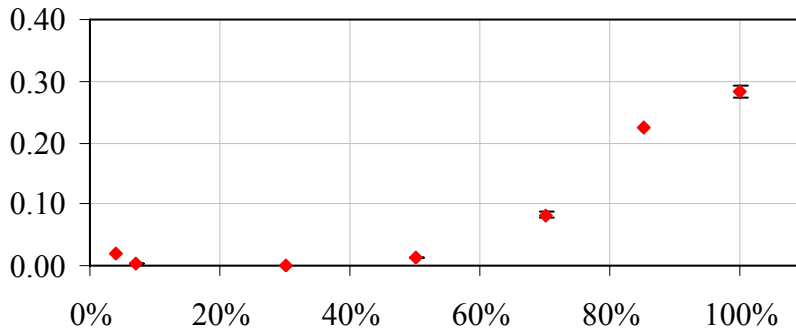
Figure 10b: Engine Emissions Parameters as a Function of Engine Power for AC # 908

Dgeom
Dgeom increases with engine power setting from a minimum of 21nm to a maximum of 40nm. This trend is consistent with behavior of the CFM56-2C1 engine studied in APEX campaign (Lobo et al., 2007)

Sigma
Sigma increases slightly with power from 1.7 at low power to 1.8 at high power.

DgeomM
DgeomM is initially higher at low power, goes through a minimum at 30% power and then increases with power.

37

EIn

EIn is higher at the low power conditions, exhibits a minimum at 30% power and then increases with power. Again this trend is consistent with that observed in APEX.

EIm

EIm is similar to EIn, higher at the low power conditions, exhibits a minimum at 30% power and then rapidly increases with power.

A/C # 918 – Aircraft: MD-88, Engine: JT8D-219

Dgeom (nm) vs. Power
Aircraft: MD-88   Engine:JT8D-219

918

Sigma vs. Power
Aircraft: MD-88   Engine:JT8D-219

918

Dgeom M (nm) vs. Power
Aircraft: MD-88   Engine:JT8D-219

918
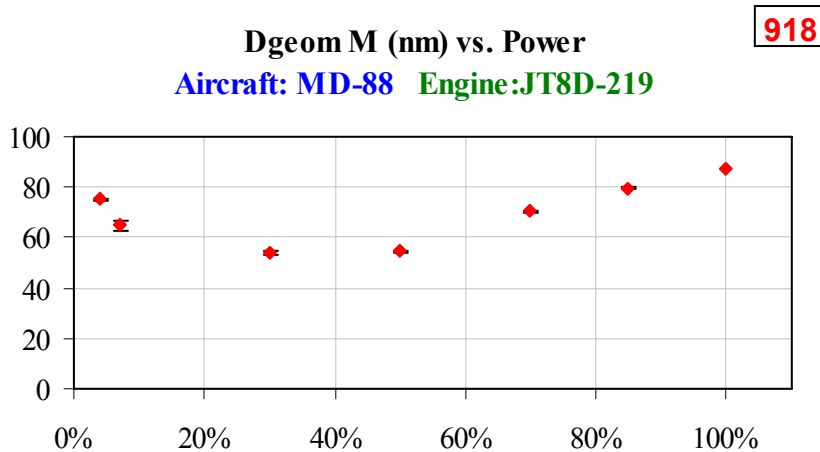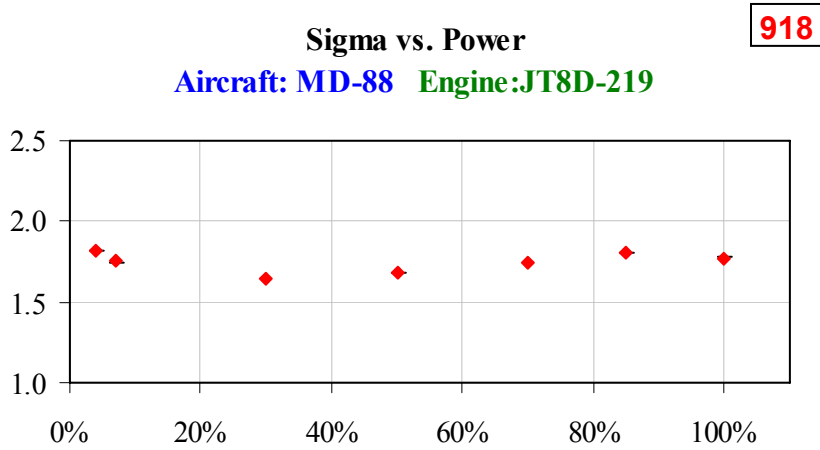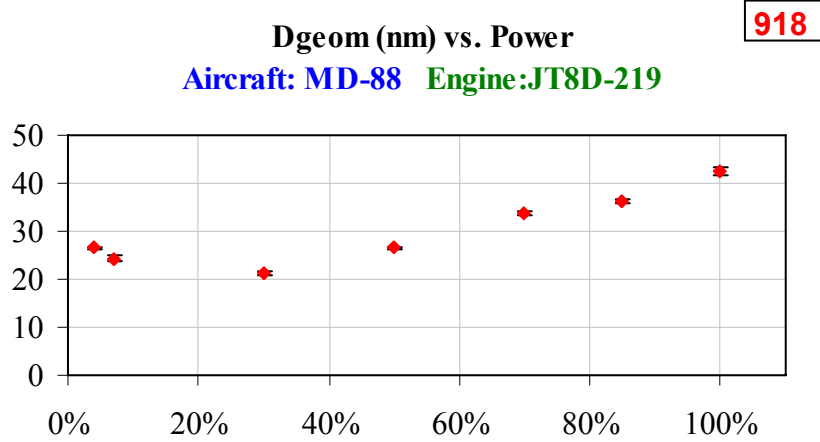
Figure 11a: Engine Emissions Parameters as a Function of Engine Power for AC# 918

EIn (1e15/kg_fu) vs. Power

Aircraft: MD-88   Engine:JT8D-219

918
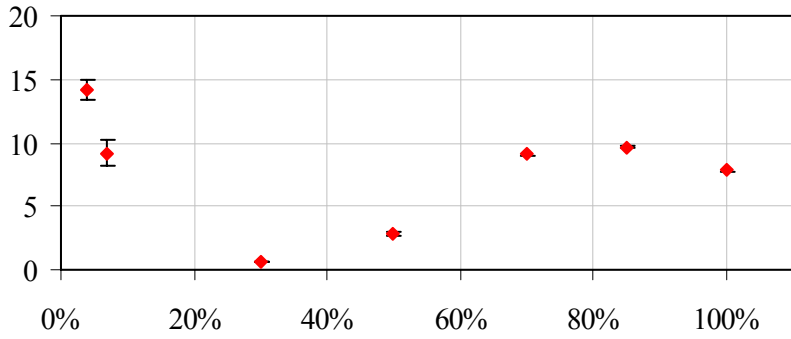
EIm (g/kg_fu) vs. Power

Aircraft: MD-88   Engine:JT8D-219

918
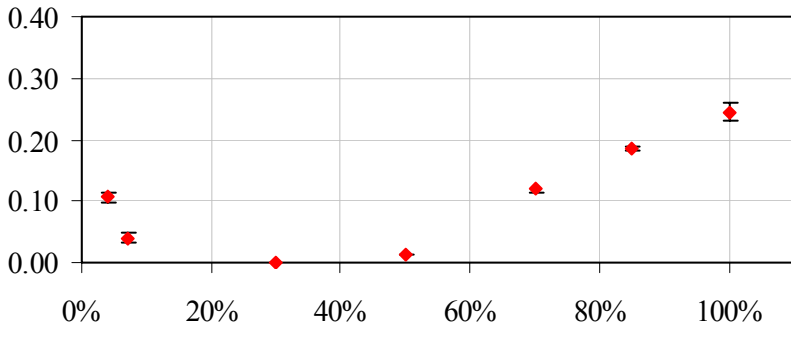
Figure 11b: Engine Emissions Parameters as a Function of Engine Power for AC# 918

This was the second aircraft with JT8D engines to be studied. The characteristic PM parameters and trends as a function of power were similar to those of first engine studied.

Dgeom
Dgeom increases with engine power setting from a minimum of 24nm to a maximum of 42nm.

Sigma
Sigma increases slightly with power from 1.7 at low power to 1.8 at high power.

DgeomM
DgeomM is initially higher at low power, goes through a minimum at 30% power and then increases with power.

EIn

EIn is higher at the low power conditions – 14×10^{15} particles/kg fuel burnt at 4% power, exhibits a minimum at 30% power and then increases with power. This behavior is consistent with the previous JT8D engine studied.

EIm

EIm is similar to EIn, higher at the low power conditions, exhibits a minimum at 30% power and then rapidly increases with power.

3.1.1.1 Comparison of PM emissions from JT8Ds

The average percent difference and rms percent difference between the two JT8D-219 engines studied is presented in Table 3. Two sets of data are presented – one with the percent difference for each parameter at all powers and the second with average percent difference for each parameter at all but the 4% and 7% power conditions. The 4% and 7% power conditions were excluded in the second average because the engine is usually not operating efficiently at these power conditions and there is greater variation in the measured parameters.

Table 3: Comparison of PM parameters from JT8D-219 engines studied

Engine	Dgeom		Sigma		DgeomM		EIn		EIm	
	Avg % Diff	RMS % Diff	Avg % Diff	RMS % Diff	Avg % Diff	RMS % Diff	Avg % Diff	RMS % Diff	Avg % Diff	RMS % Diff
JT8D-219 (all powers)	-5	5	-1	2	-6	9	-25	65	-45	83
JT8D-219 (w/o 4&7%)	-2	8	0	1	-3	5	12	16	-2	20

The results indicated that the differences observed between the two JT8D-219 engines are small. The second JT8D engine (AC#918) has smaller soot particles, and more of them, yet its mass-based emission index is lower on average. This can be attributed to that fact that these smaller particles have very little mass associated with them.

The inclusion of the data from the idle conditions, 4% and 7% power, does influence the percent difference.

A/C # 134 – Aircraft: B767-300, Engine: GE CF6-80A2

134

Dgeom (nm) vs. Power
Aircraft:B767-300   Engine:GE CF6-80A2

134

Sigma vs. Power
Aircraft:B767-300   Engine:GE CF6-80A2

134

Dgeom M (nm) vs. Power
Aircraft:B767-300   Engine:GE CF6-80A2
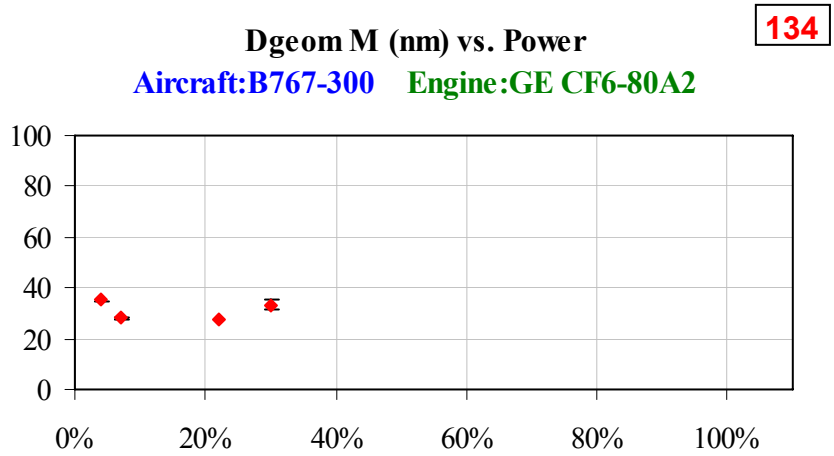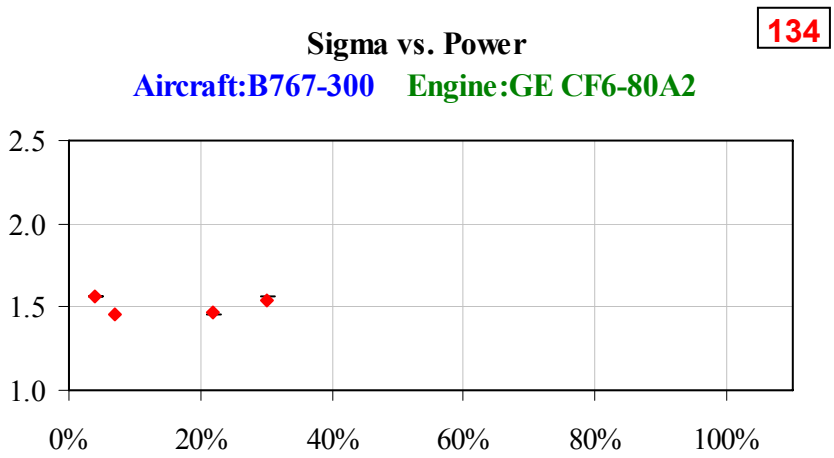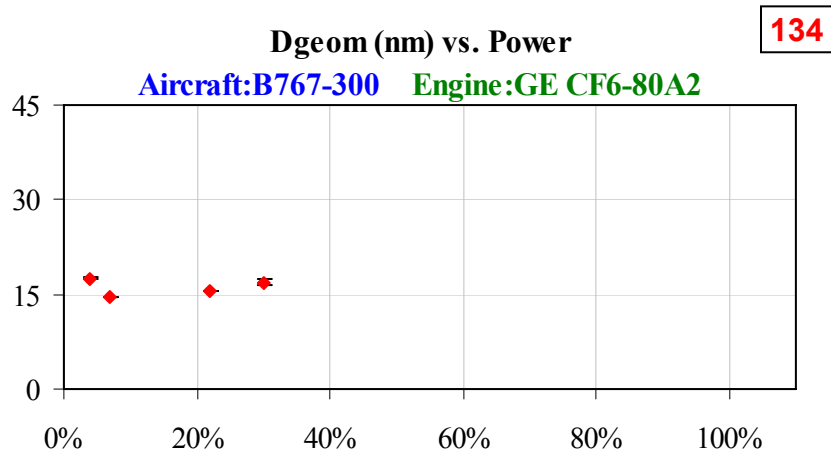
Figure 12a: Engine Emissions Parameters as a Function of Engine Power for AC# 134

EIn (1e15/kg_fu) vs. Power

Aircraft:B767-300   Engine:GE CF6-80A2

134

EIm (g/kg_fu) vs. Power

Aircraft:B767-300   Engine:GE CF6-80A2

134
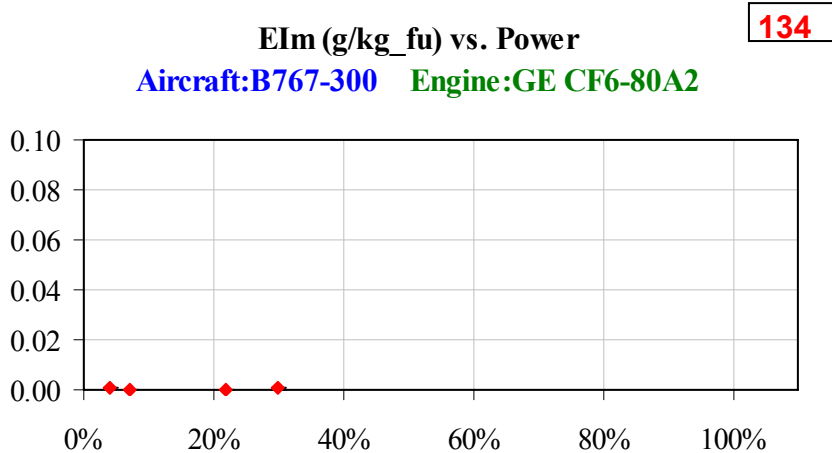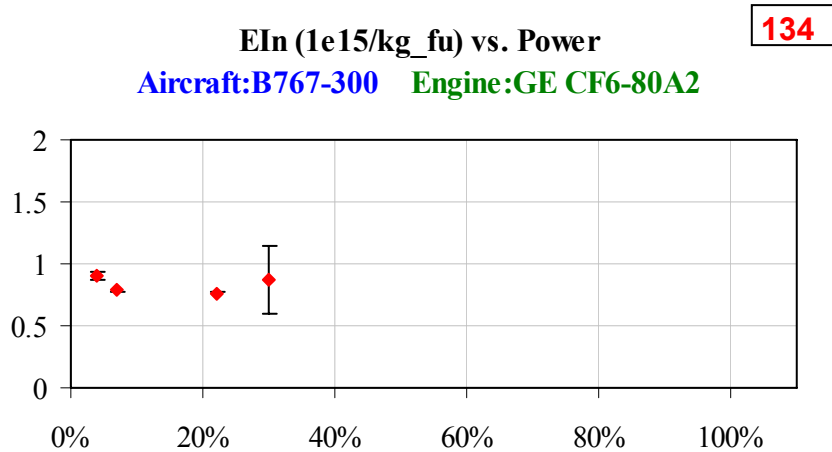
Figure 12b: Engine Emissions Parameters as a Function of Engine Power for AC# 134

This engine was the first of the high power engines studied. For this engine, PM emissions could only be acquired from idle to 30% power. At higher engine power conditions the probe stand assembly became unstable, thus limiting the extent to which exhaust sample could be acquired.

The data acquired is very limited and no trends with engine power condition can be discerned. However, the values of the PM parameters at these low power conditions are similar in magnitude to those of the JT8D engines studied previously.

A/C # 1816 – Aircraft: B767-400ER, Engine: GE CF6-80C3B8F

Dgeom (nm) vs. Power
1816
Aircraft:B767-400ER   Engine:CF6-80C2B8F

Sigma vs. Power
1816
Aircraft:B767-400ER   Engine:CF6-80C2B8F

Dgeom M (nm) vs. Power
1816
Aircraft:B767-400ER   Engine:CF6-80C2B8F
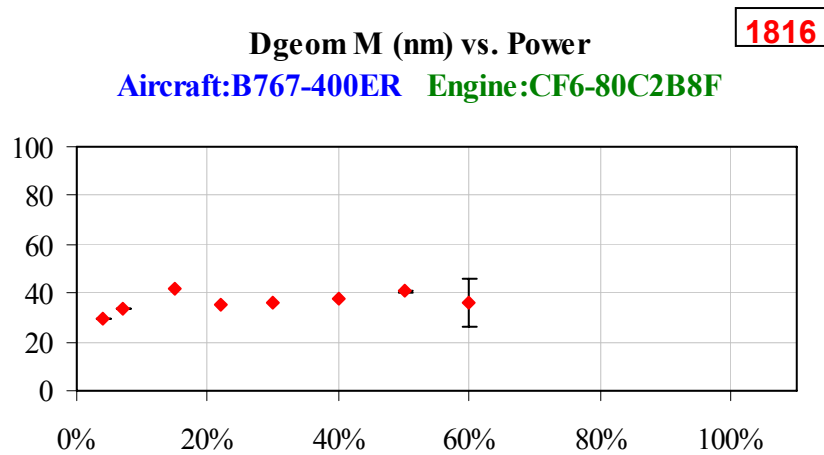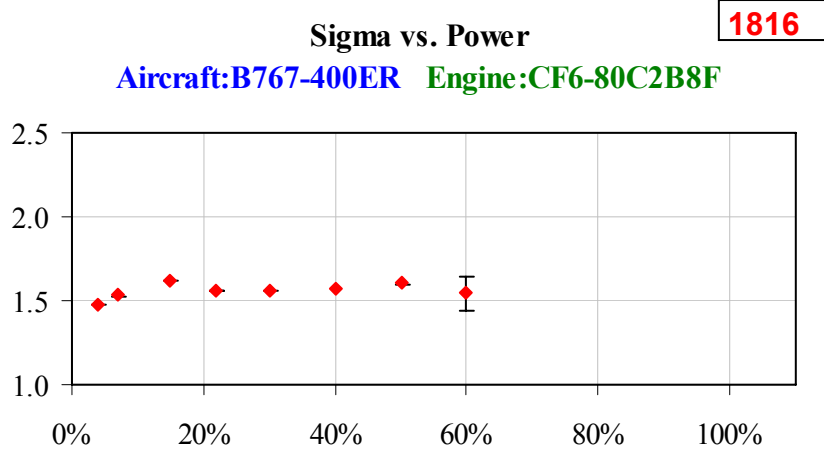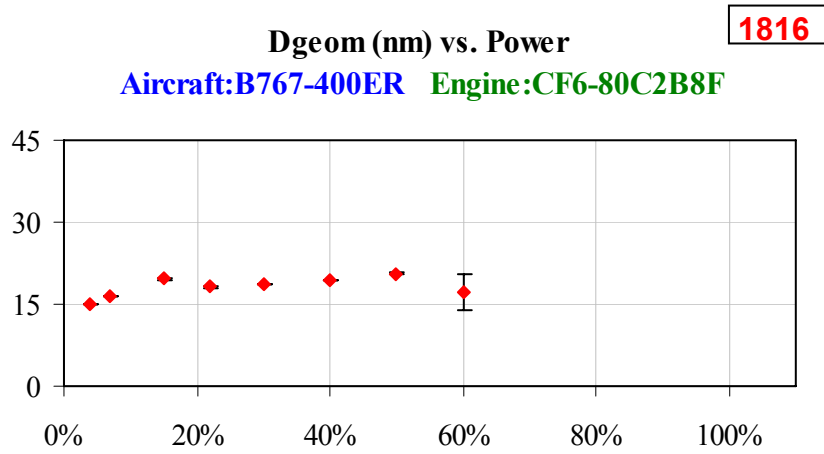
Figure 13a: Engine Emissions Parameters as a Function of Engine Power for AC# 1816

EIn (1e15/kg_fu) vs. Power

Aircraft:B767-400ER   Engine:CF6-80C2B8F
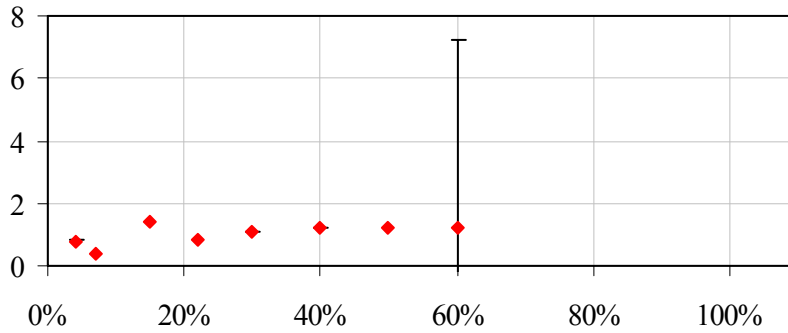
EIm (g/kg_fu) vs. Power

Aircraft:B767-400ER   Engine:CF6-80C2B8F
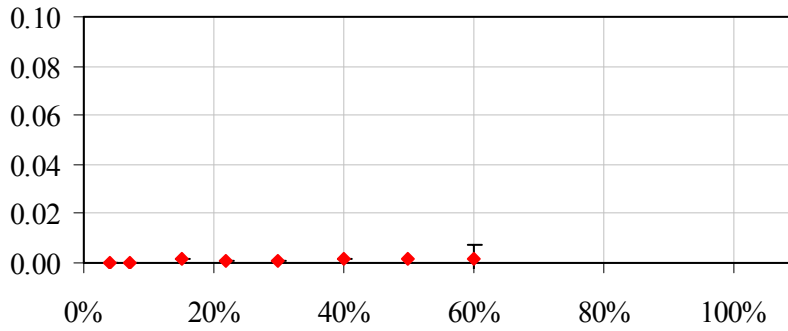
Figure 13b: Engine Emissions Parameters as a Function of Engine Power for AC# 1816

This engine is similar to the previous CF6-80 studied, but is a different model with about 20% more thrust. The probe assembly was modified so that a full range of PM emissions could be acquired. While modification did allow for exhaust samples to be collected from idle to the 60% engine power condition, the high power conditions were not able to be run. Once again, due to the limitations of this dataset, no meaningful trends can be inferred from the data acquired.

A/C # 635 – Aircraft: B757-200, Engine: PW 2037

635

Dgeom (nm) vs. Power
Aircraft:B757-200   Engine:PW 2037

635

Sigma vs. Power
Aircraft:B757-200   Engine:PW 2037

635

Dgeom M (nm) vs. Power
Aircraft:B757-200   Engine:PW 2037
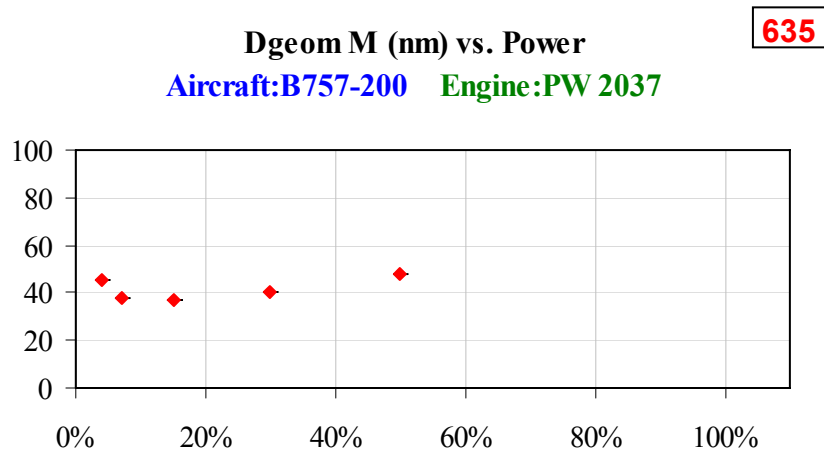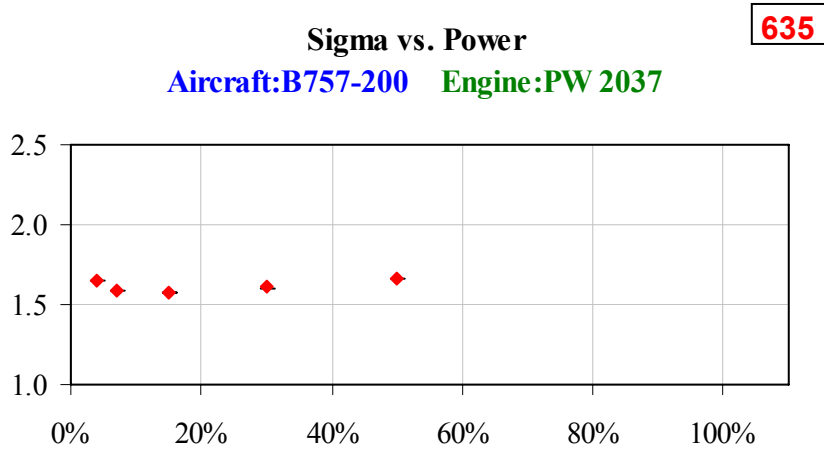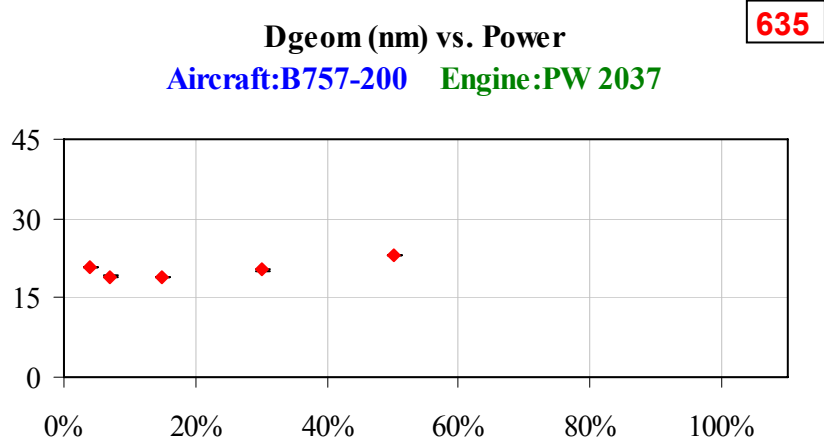
Figure 14a: Engine Emissions Parameters as a Function of Engine Power for AC# 635

EIn (1e15/kg_fu) vs. Power

Aircraft:B757-200   Engine:PW 2037
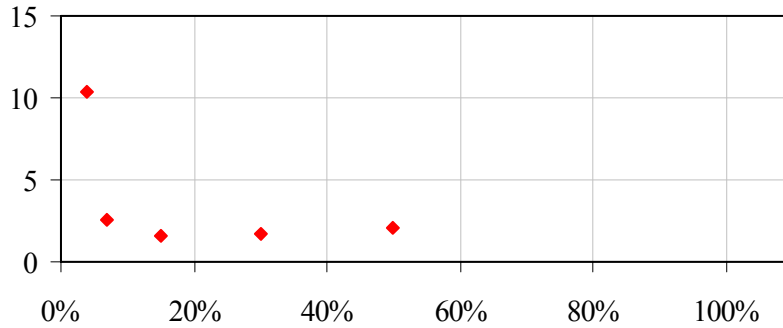
EIm (g/kg_fu) vs. Power

Aircraft:B757-200   Engine:PW 2037
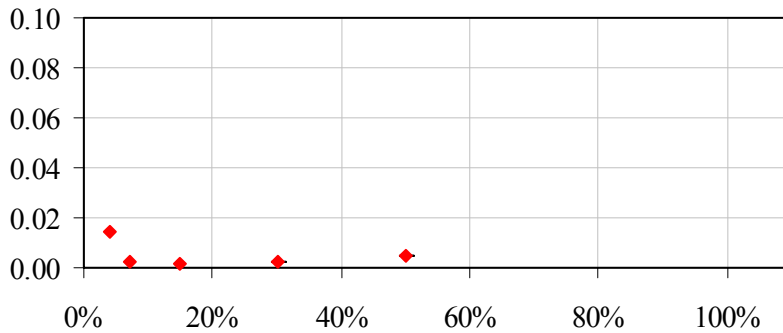
Figure 14b: Engine Emissions Parameters as a Function of Engine Power for AC# 635

This engine was the first of the PW2037 engines studied. For this engine, PM emissions could only be acquired from idle to 50% power. At higher engine power conditions the probe stand assembly became unstable, thus limiting the extent to which exhaust sample could be acquired. The data acquired is very limited and no trends with engine power condition can be discerned.

A/C # 640 – Aircraft: B757-200, Engine: PW 2037

Dgeom (nm) vs. Power

Aircraft:B757-200   Engine:PW 2037

640

Sigma vs. Power

Aircraft:B757-200   Engine:PW 2037

640

Dgeom M (nm) vs. Power

Aircraft:B757-200   Engine:PW 2037

640
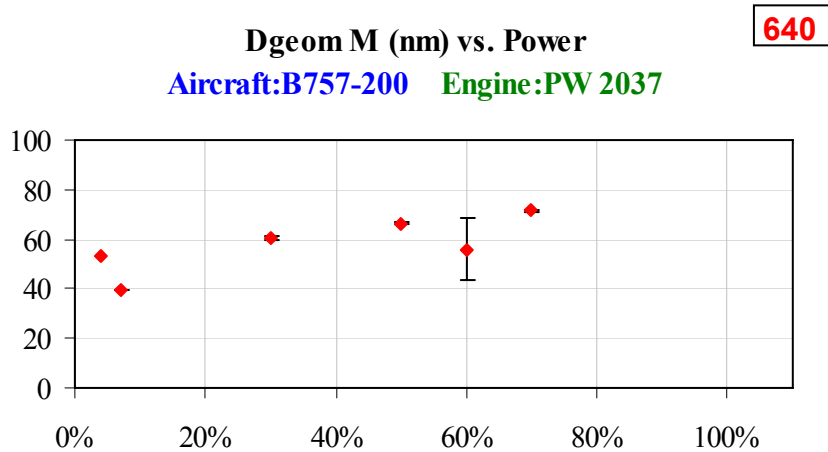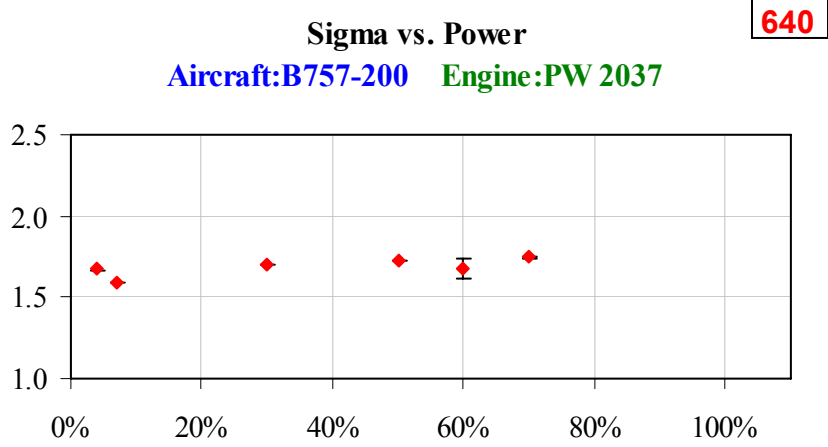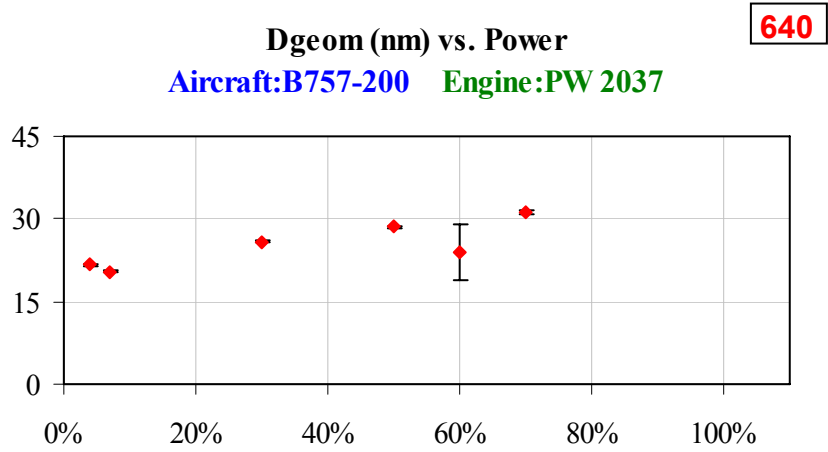
Figure 15a: Engine Emissions Parameters as a Function of Engine Power for AC# 640

48

EIn (1e15/kg_fu) vs. Power
Aircraft:B757-200   Engine:PW 2037
640
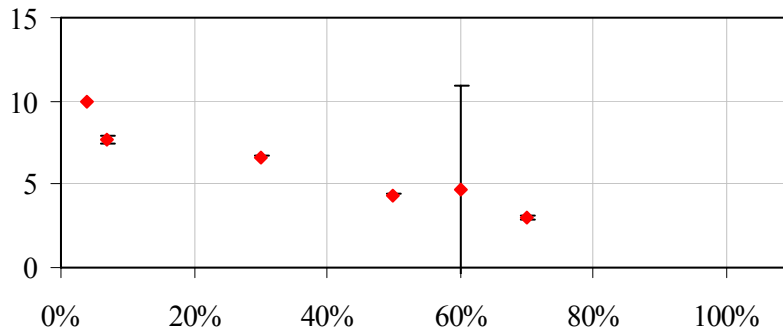
EIm (g/kg_fu) vs. Power
Aircraft:B757-200   Engine:PW 2037
640
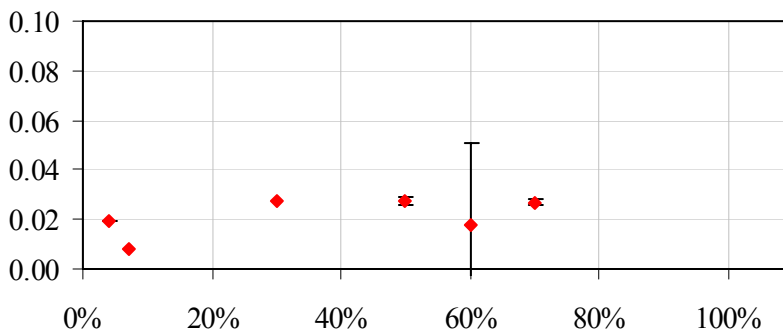
Figure 15b: Engine Emissions Parameters as a Function of Engine Power for AC# 640

This engine is similar to the previous PW2037 studied. Once again, the instability of the probe stand at the higher power limited the collection of exhaust samples from idle to the 70% engine power condition.

3.1.2 ARI Data

Due to the greater absolute thrust rating for the CF6 and 2037 engines and fears of the probe stand not being able to withstand the force, the higher engine settings were not sampled during this work. Despite this deficit, the particle mass loadings for black carbon (soot) appear to be similar to the APEX-1 result. Fig. 16 shows the black carbon mass loading emission index as a function of the nominal fraction of engine rated thrust for several engines studied. The APEX-1 data for the CFM56 engine is also on the figure as the grey points connected with the dashed line. The two JT8D engines in this study have the greatest black carbon emission indices. This is due to a prevalent soot mode at 40-80 nm (particle mobility diameter). The CF6 and PW2037 engines emit soot in a smaller size mode, < 50nm with overall less total black carbon mass. These engines, however, have a greater particle number emission index than the JT8D. Anecdotally, the JT8D emits fewer but larger particles while engines designed to reduce smoke number certification measurements emit more numerous quantities of smaller particles.
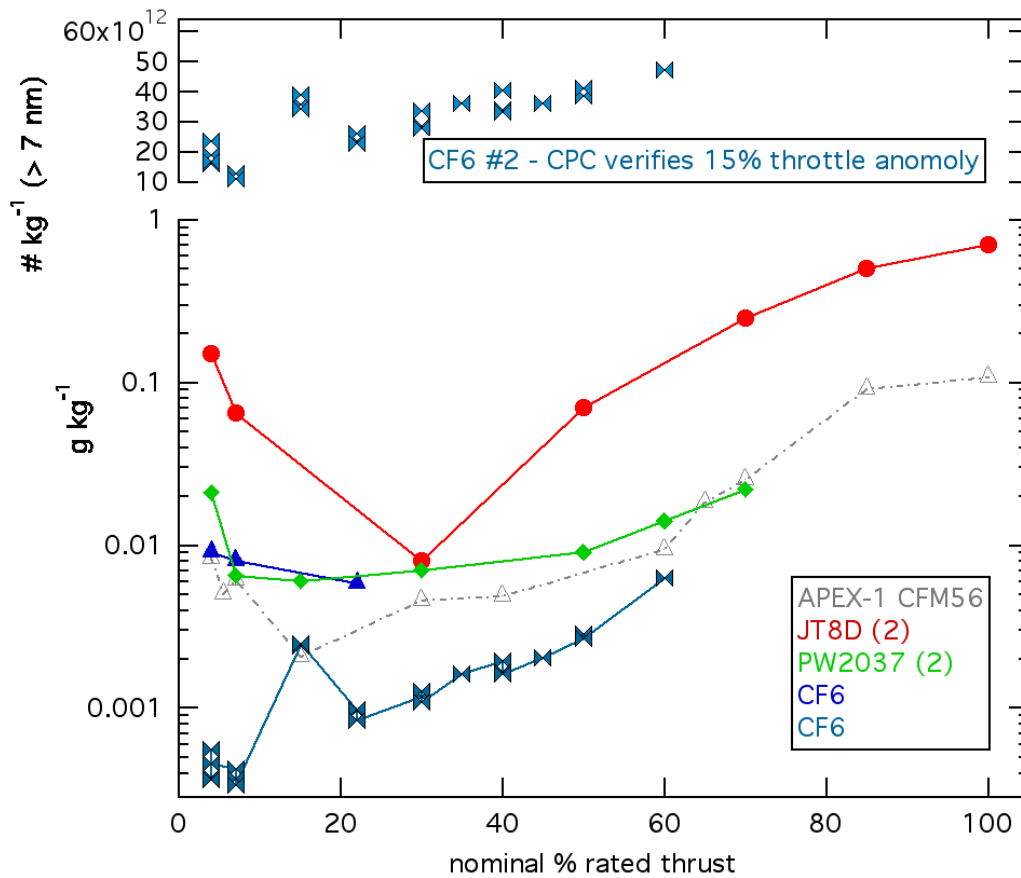
Figure 16: The lower panel portrays the black carbon mass loading emission index vs. the nominal fraction of engine rated thrust for several engines in this study. The upper panel shows the particle number emission index for one of the CF6 engines with an off- trend data point at 15% of rated thrust in the black carbon EI.

Because the exhaust for all engines was sampled at ~1m from the engine exit plane, it is too hot for condensable species to be present on the soot particulate. Fig.17, however, indicates that condensation is taking place in the probe. In the figure, the yellow and orange points are the lower throttle data points (ground idle ~4% and 7%). When looking at the yellow and orange points in this figure only, four bands emerge and are the pastel blobs. From least EIn to greatest, the trend for these clusters is CF6-80C2B8F, PW2037, JT8D-219 and CF6-80A2. The ICAO 7% certification point for each engine is indicated with an arrow to help guide the eye. The AMS Organic particulate loading qualitatively correlates with the ICAO UHC with a couple of outliers in the JT8D-219. This is somewhat sensible, when the engine emits unburned hydrocarbons, it is quite likely that the mechanism leading to incomplete combustion is producing partially combusted low volatility species which can either participate in nucleation or condense to available soot surface area. In the case of the JT8D-219 engine, the latter is quite likely due to the presence of a relatively greater black carbon emission index.
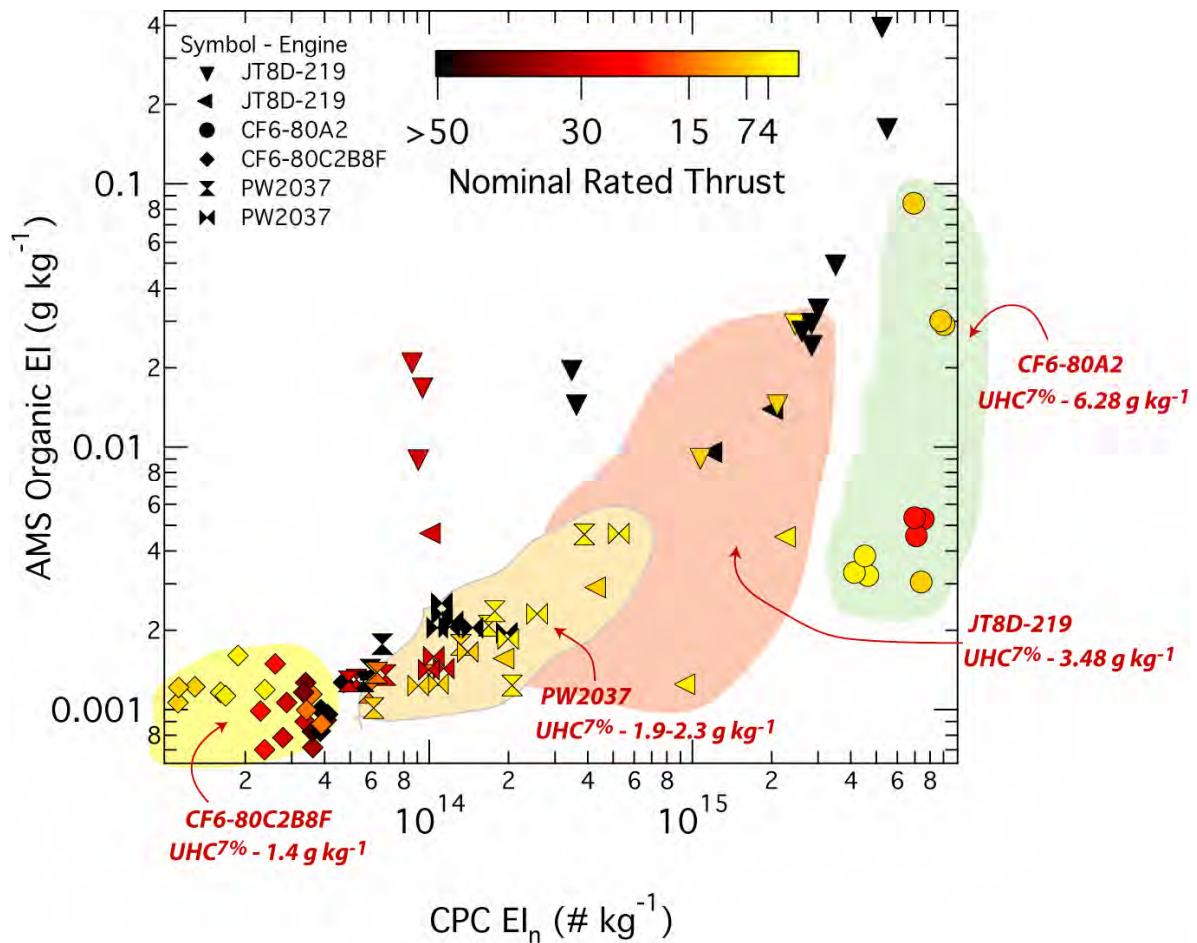
Figure 17: Organic Particulate loading vs. Particle number emission index. The results for all aircraft in this study are plotted, colored by the nominal fraction of rated thrust.

3.1.3 LIDAR Results

Measurements were performed on six different aircraft using the arrangement shown in Fig. 18. The LIDAR and its pointing azimuth were fixed, and each aircraft was positioned with its primary engine approximately 310 m away and with the aftmost part of the stabilizer 10 m from the scan plane. The distance from engine exhaust nozzle to the scan plane varied and was > 10 m. Table 4 lists pertinent facts for each aircraft event.

Table 4: Stationary Aircraft Measurements. Times are UTC

Date	Time Start	Time End	Aircraft Type	Engine Type	Primary Throttle Settings (%)	Secondary Engine?
9/22/2004	0614	0715	MD88 (a) [§]	JT8D-219	4, 7, 30, 50, 70, 85, 100	no
9/23/2004	0532	0655	MD88 (b)	JT8D-219	4, 7, 30, 50, 70, 85, 100	no
9/23/2004	1000	1054	B767-300 (A)	CF6-80C2A1	4, 7, 22	no
9/24/2004	0430	0613	B767-400ER (B)	CF6-802CB8	4, 7, 15, 22, 30, 40, 45, 50, 60	yes
9/24/2004	0833	0929	B757-200 (a)	PW2037	4, 7, 15, 30, 45, 50	yes
9/25/2004	0604	0802	B757-200 (b)	PW2037	4, 7, 30, 50, 70, 85, 100	yes

[§]*The letters in parentheses differentiate between like aircraft types in the graphs of results.*

The LIDAR performed repeated sweeps up and down through the exhaust plume, each one-way pass including ≈ 50 pulses. After typically 1-2 minutes at a steady power setting, the throttle was changed and the engines stabilized at the next power setting before data acquisition resumed. The throttle was usually cycled through the settings more than once. The "PP" worksheet in the spreadsheet files on CD for each aircraft in Table 4 has the measured plume parameters for each sweep. The "Ave" worksheet has the averages and sample standard deviations for the sweeps at each power setting. The detailed results are listed in spreadsheets with file names with the aircraft type and letter designator on the attached CD. When a power setting was used multiple times for an aircraft, these were averaged to form the final LIDAR result.

Fig.18 shows the enhanced backscatter for one sweep through the plume from a single tail-mounted JT8D219 engine, and Fig. 19 is for two wing-mounted engines both at the

same throttle setting. The patchiness in the plume is a result of the turbulent mixing with the ambient air, and also perhaps unsteady soot emission rates from the engine. The averaged vertical profile was close to Gaussian in shape. The LIDAR was able to resolve the vertical profile, but the horizontal resolution was too coarse to measure the true width of the plume. For the single, tail-mounted engine, the horizontal profile was assumed Gaussian with the same spatial standard deviation as the measured vertical profile. The vertical profile from the wing-mounted engines was approximately a half-Gaussian, i.e., a maximum near the ground and decreasing as a Gaussian curve above the maximum. An attempt to deconvolve the LIDAR range gate was not accurate enough to rely on. It was noted that the engines tilt downward slightly, so the plume from engines mounted low on the wings would be expected to spread faster horizontally than vertically. The horizontal profile from each engine was assumed Gaussian in shape with a spatial standard deviation twice the standard deviation of the standard deviation of the vertical Gaussian, an assumption consistent with the coarse deconvolution result and the expected spreading.
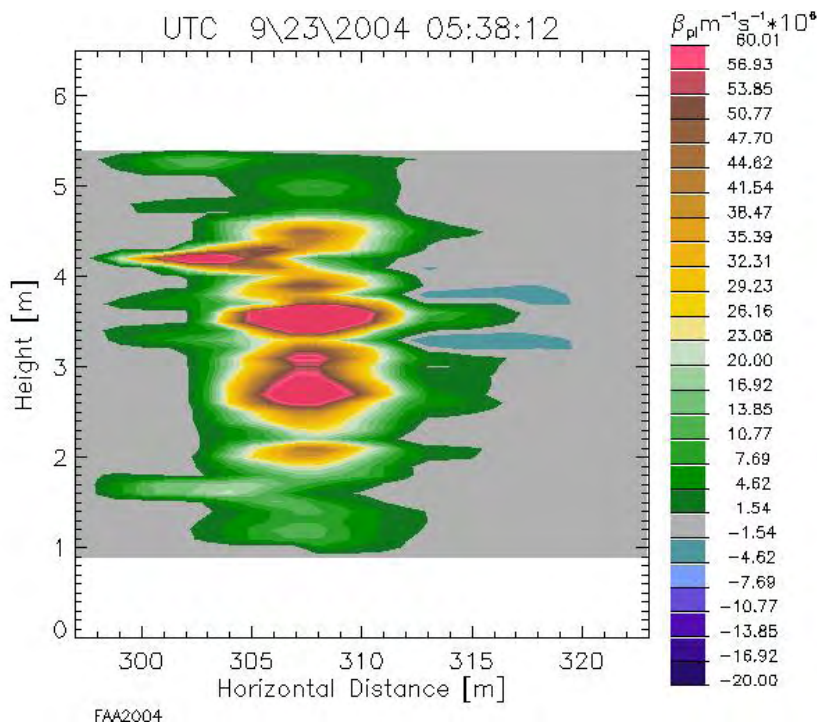
Figure 18: Enhanced backscatter for one sweep 10 m aft of the tail of an MD88 with a single, tail-mounted engine operating at 100% throttle. Note the vertical scale is expanded about 4 times.

For power settings with low emission rates and no plume contrast against background, the plume sizes were assumed identical to visible plumes at other power settings from the same aircraft.
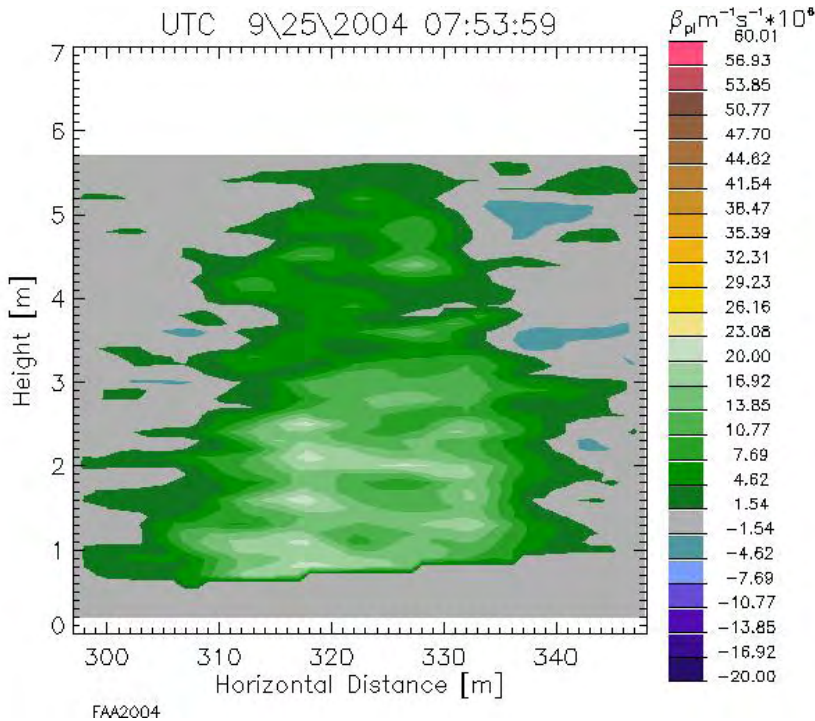
Figure 19: Enhanced backscatter for one sweep 10 m aft of the tail of a B757 with both wing-mounted engines operating at 70% throttle. Note the vertical scale is expanded about 7.5 times. The upward stepping of the plume at the bottom is due to a slight rise in height of the ground.

3.1.3.1 Emission Index Results

The final value for soot emission index is

$$EI = EI_{enh} + EI_{vol} + EI_{\Delta T} \; . \tag{Eq. 38}$$

When only one engine was running, Eq. 36 was applied directly. When two engines were operated at identical power setting, the *EI* for both engines was determined and the result divided by two to obtain the emission value corresponding to the primary engine. When the secondary engine operated at a different throttle setting than the primary engine, the *EI* was obtained for both engines, the emission rate from the secondary engine was determined from results of both engines at lower power settings, and the latter was subtracted to isolate the emission rate from the primary engine. This bootstrapping procedure was less accurate than if we had always had only the primary engine operating or two operating at identical throttle settings.

The experimental values of EI_{enh} for individual power settings ranged from -.138 to 0.662 g/kg. The value below zero is from a slightly "negative" plume, for which the noise in the data, non-uniform ambient conditions, and inadequacies in the theory or yield an unphysical result. The values for the sum of the second and third terms for single runs at

one power setting ranged from 0.006 to 0.036 g/kg, so these adjustments are very significant for engines with low emission rates but are minor for engines with strong soot emission.

The results for like power settings for each aircraft were averaged and are shown in Table 5 and Figs. 20-22. The MD88 aircraft exhibited strong emissions at high power settings, substantial emissions at idle (4%) and taxi (7%) power settings, and low emissions at other power settings. The B767's had low emissions, even negative values. (It is of course impossible to have negative soot emissions, but the noise in the data, non-uniform ambient, and imperfections in the theory could all contribute to negative values of *EI*. These negative *EI* values help indicate the limits of accuracy in the current LIDAR method). The B757's had emission index values that overall were between those of the MD88's and the B767's. Differences between the two aircraft of one type were smaller than differences between types of aircraft.

Table 5: Stationary aircraft parameters and emission index results from LIDAR

Aircraft	Throttle %	Fuel flow (kg/s)	Thrust (kNt)	Air mass flow (kg/s)	# cycles in average	Nozzle velocity (m/s)	Nozzle ΔT (°K)	Emission Index (g/kg)
MD88(a)	4	0.0980	3.861	44.20	2	87.3	91.5	0.080
"	7	0.1344	6.756	58.47	2	115.6	92.2	0.042
"	30	0.3817	28.96	121.1	2	239.2	107.1	0.019
"	50	0.6100	48.26	156.3	2	308.8	120.3	0.096
"	70	0.8650	67.56	184.9	2	365.4	134.7	0.328
"	85	1.085	82.04	203.8	2	402.7	148.2	0.554
"	100	1.354	96.52	221.0	2	436.7	168.5	0.618
MD88(b)	4	0.0980	3.861	44.20	1	87.3	91.5	0.309
"	7	0.1344	6.756	58.47	3	115.6	92.2	0.085
"	30	0.3817	28.96	121.1	3	239.2	107.1	0.044
"	50	0.6100	48.26	156.3	2	308.8	120.3	0.046
"	70	0.8650	67.56	184.9	2	365.4	134.7	0.238
"	85	1.085	82.04	203.8	2	402.7	148.2	0.373
"	100	1.354	96.52	221.0	3	436.7	168.5	0.542
B767(A)	4	0.142	10.30	160.4	3	64.2	36.0	-0.043
"	7	0.200	18.02	212.2	3	84.9	36.9	0.095
"	22	.0480	56.63	376.2	2	150.5	43.6	-0.033
B767(B)	4	0.144	10.68	160.4	4	66.6	36.4	-0.029
"	7	0.205	18.69	212.2	3	88.1	37.7	-0.009
"	15	0.366	40.05	310.6	3	128.9	42.4	0.009
"	22	0.510	58.74	376.2	3	156.2	46.1	-0.019
"	30	0.688	80.11	439.3	3	182.4	50.8	-0.025
"	40	0.910	106.8	507.2	3	210.6	55.1	-0.015
"	45	1.028	120.2	538.0	1	223.3	57.3	0.005
"	50	1.150	133.5	567.1	4	235.4	59.6	-0.018
"	60	1.410	160.2	621.2	1	257.9	64.5	0.026
B757(a)	4	.108	6.65	121.6	3	54.7	36.7	0.041
"	7	.152	11.64	160.9	2	72.4	38.0	-.004
"	15	.260	24.95	235.5	2	106.0	41.9	0.023
"	30	.458	49.91	333.0	2	149.9	47.9	0.122
"	45	.670	74.86	407.9	1	183.5	53.9	0.274
"	50	.750	83.18	429.9	3	193.5	56.4	0.293
B757(b)	4	.108	6.65	121.6	4	54.7	36.7	-0.077
"	7	.152	11.64	160.9	3	72.4	38.0	-0.057
"	30	.458	49.91	333.0	3	149.9	47.9	0.075
"	50	.750	83.18	429.9	4	193.5	56.4	0.256
"	70	1.060	116.4	508.7	4	228.9	63.5	0.259
"	85	1.307	141.4	560.5	1	252.2	68.6	0.190
"	100	1.571	166.4	608.0	1	273.6	73.8	0.202
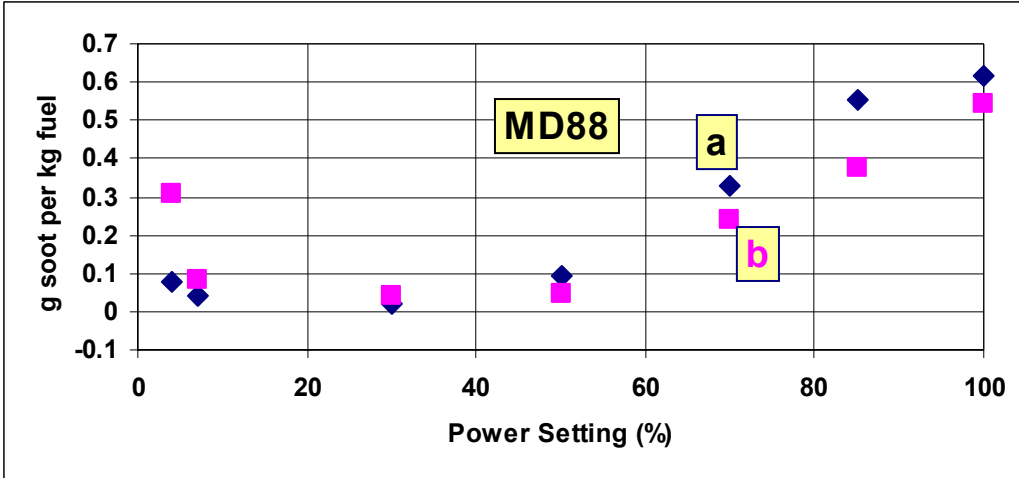
Figure 20: *EI* results from LIDAR for MD88 stationary aircraft.
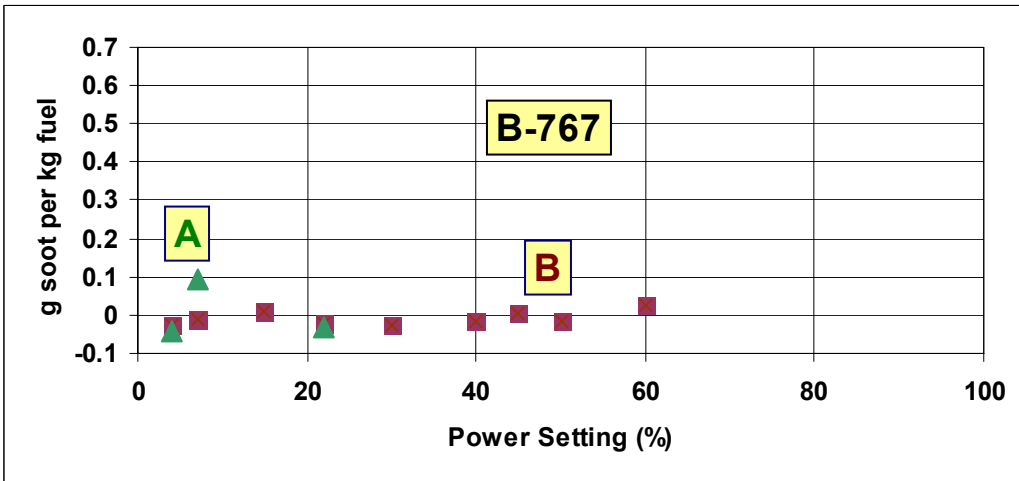
Figure 21: *EI* results from LIDAR for B-767 stationary aircraft.
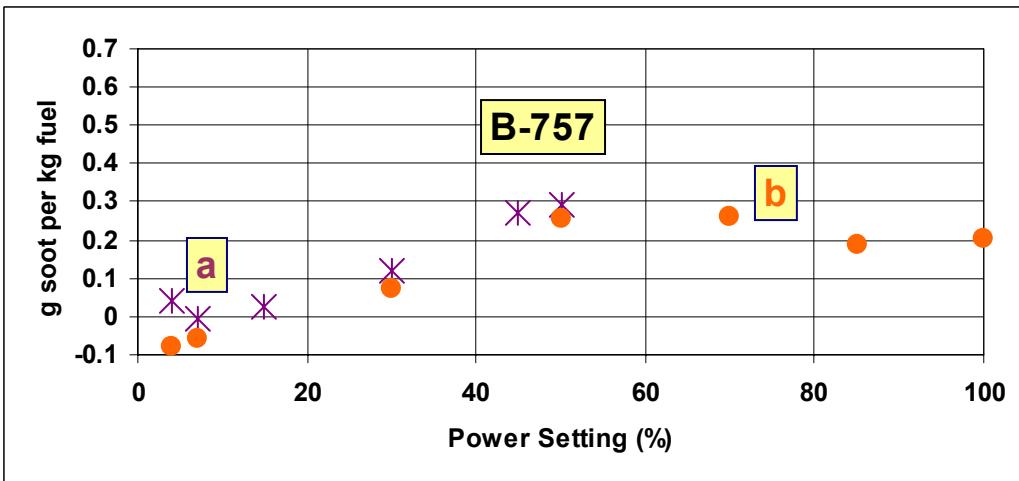
Figure 22: *EI* results from LIDAR for B-757 stationary aircraft.

3.1.4 Comparison of Emission Indices obtained from Probe sampling and LIDAR

LIDAR sampling was done concurrently with exhaust probe sampling, which permitted a direct comparison of PM mass measured from the probes (the "gold" standard) to the LIDAR system.

Table 6 lists the individual comparative data for each engine tested. The estimated root-mean-square uncertainty in LIDAR measurements, assuming its several sources of error are independent, is ± a factor of 2 with an additional ±0.05 g/kg. The factor of 2 uncertainty is principally from potential bias, especially the value of η. The ±0.05 g/kg is mostly from random measurement errors.

While the correlation with some engines as compared to others was better, it can be seen from this table that in general, the differences were substantial. However, the uncertainty in the analysis must be considered. If the probe samples are very near zero, as occurs for some engines, the error limits for both measurement techniques would have to be considered. In the best case, values varied by a factor of 0.3 (JT8D-219). For the worst case, values varied by a factor of almost 511. The average error was a negative factor of 17.3.

These errors are thought to have occurred for two reasons. First, too many assumptions had to be made. If further testing were to be done, these assumptions could be greatly limited by collection of specific data (e.g., temperature and wind parameters). The second problem may be related to understanding the true efficiency of the measurement. It was assumed that η was known. This parameter is crucial and could have a large impact on the reported results.

To further test the applicability of the LIDAR mass remote sensing, trends were analyzed. Figures 23 through 28 show scatterplots comparing LIDAR and probe sampling results for the engines tested. It can be seen graphically that some engines, such as the JT8D-219, show excellent correlation. Others, such as the PW2037, have almost no agreement. Even the same class of engines does not show the same agreement on occasion. The R^2 values for the two JT8D-219 engines are 0.966 and 0.959, while the values for the two PW2037 engines are 0.512 and 0.001.

There are two potential reasons for observing different results from the same engine types. The first is the size of the particulate matter being emitted. Engines vary and the LIDAR is working in the lower range of detectability, where small changes in particulate matter emissions can have tremendous impacts on the results. In the case of the PW2037, there was also a compounding factor. During the test with very low correlation, the wind was blowing from the tail to the front of the aircraft. Recirculation was occurring. While the probes were not tremendously affected, the LIDAR saw the entire ambient PM, resulting in much higher PM results. In addition, the recirculated PM was most likely larger due to growth of the particles that typically occur in the atmosphere and the condensation of volatile PM.

Table 6: EI Data Derived by LIDAR Compared to Probe Sampling by UMR

AC Engine	% Power Setting	EI, LIDAR (g/kg fuel)	EI UMR$_{DMS}$ (g/kg fuel)	Absolute Difference	Fractional Difference
CF6-80C2A1	4	-3.07E-02	5.64E-04	3.13E-02	54.5
	7	1.06E-01	2.08E-04	-1.06E-01	-510.7
	22	-2.45E-02	1.95E-04	2.47E-02	125.9
	30		4.49E-04	NA	NA
PW2037	4	5.75E-02	1.47E-02	-4.29E-02	-3.9
	7	1.71E-02	2.23E-03	-1.49E-02	-7.7
	15	3.31E-02	1.44E-03	-3.16E-02	-23.0
	30	1.49E-01	2.27E-03	-1.46E-01	-65.5
	45	2.79E-01		NA	NA
	50	2.99E-01	5.02E-03	-2.94E-01	-59.6
PW2037	4	-6.99E-02	1.97E-02	8.97E-02	3.6
	7	-4.71E-02	8.17E-03	5.53E-02	5.8
	30	8.18E-02	2.77E-02	-5.41E-02	-2.9
	50	1.05E+00	2.74E-02	-1.02E+00	-38.1
	60		1.80E-02	NA	NA
	70	2.64E-01	2.70E-02	-2.37E-01	-9.7
	85	1.94E-01		NA	NA
	100	2.06E-01		NA	NA
CF6-80-C2B8	4		2.76E-04	2.76E-04	
	7	2.28E-03	2.13E-04	-2.07E-03	-10.7
	15	1.84E-02	1.84E-03	-1.66E-02	-10.0
	22	-1.12E-02	6.50E-04	1.18E-02	17.2
	30	-1.83E-02	9.57E-04	1.93E-02	19.2
	40	-9.14E-03	1.34E-03	1.05E-02	6.8
	45	1.08E-02		NA	NA
	50	-5.22E-02	1.79E-03	5.40E-02	29.2
JT8D-219	60	3.03E-02	1.39E-03	-2.89E-02	-21.7
	4	7.06E-02	1.79E-02	-5.27E-02	-3.9
	7	4.40E-02	4.13E-03	-3.99E-02	-10.7
	30	2.40E-02	1.30E-03	-2.28E-02	-18.6
	50	7.66E-02	1.23E-02	-6.43E-02	-6.2
	70	2.40E-01	8.29E-02	-1.57E-01	-2.8
	85	3.99E-01	2.26E-01	-1.73E-01	-1.5
JT8D-219	100	4.44E-01	2.84E-01	-1.60E-01	-1.3
	4	2.33E-01	1.06E-01	-1.27E-01	-2.1
	7	7.39E-02	4.01E-02	-3.39E-02	-1.8
	30	4.10E-02	1.29E-03	-3.97E-02	-31.8
	50	4.11E-02	1.34E-02	-2.77E-02	-3.0
	70	1.76E-01	1.19E-01	-5.64E-02	-1.4
	85	2.71E-01	1.85E-01	-8.59E-02	-1.3
	100	3.90E-01	2.45E-01	-1.45E-01	-1.3
Average Error				-8.24E-02	-17.3

Additionally, the APEX series of experiments show that particulate matter sizes and numbers change with power setting (Wey et al., 2006; Lobo et al., 2007). Both of these parameters would have a large effect on the measured backscatter and η.

The next question analyzed was how LIDAR performed for all engines in an aggregated analysis. Fig. 29 shows a scattergram of all data compared to the power settings. Fig. 30 shows the correlation between the LIDAR and probe EIs. It can be seen that a definite trend occurs.
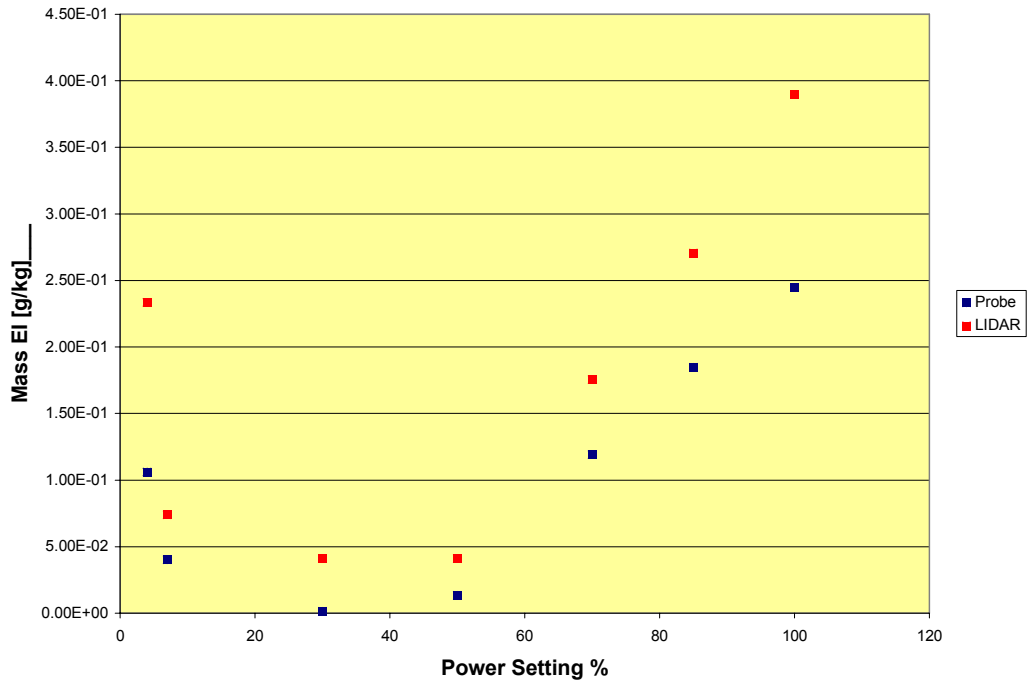
Figure 23: Comparison of LIDAR Results (Red) to Probe Sampling (Blue) for the JT8D-219 (one case)
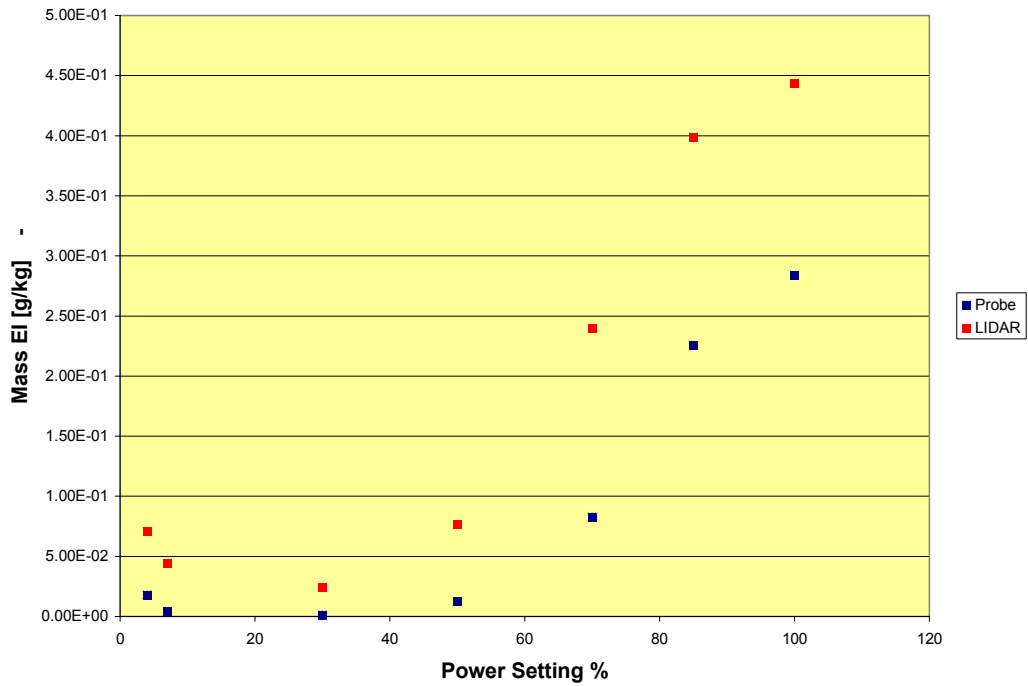
Figure 24: Comparison of LIDAR Results (Red) to Probe Sampling (Blue) for the JT8D-219 (second case)
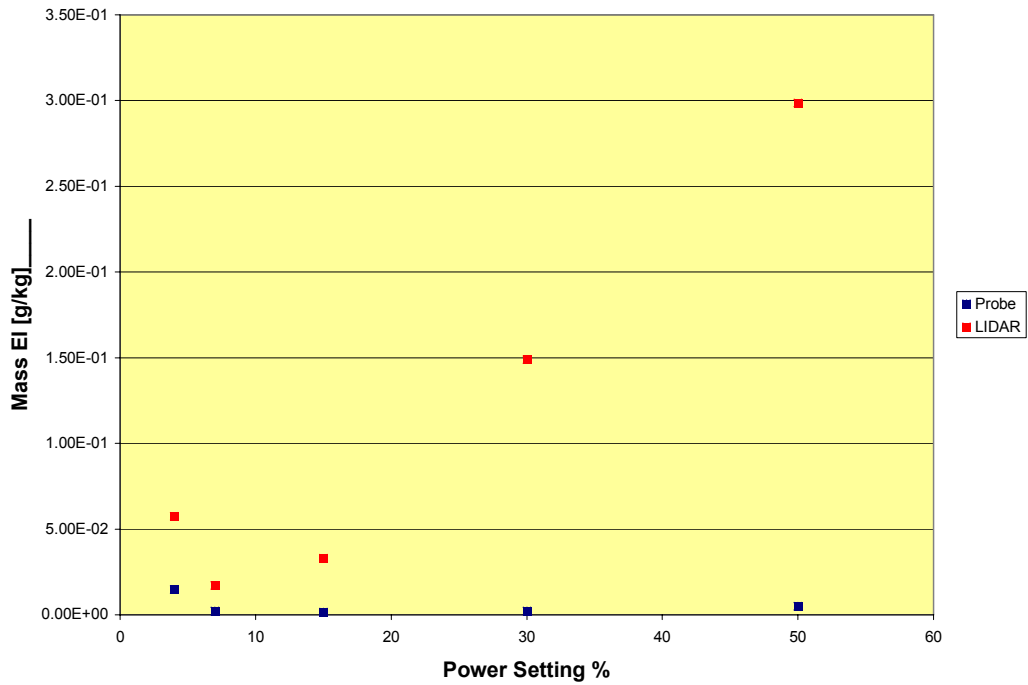
Figure 25: Comparison of LIDAR Results (Red) to Probe Sampling (Blue) for the PW2037 (one case)

61
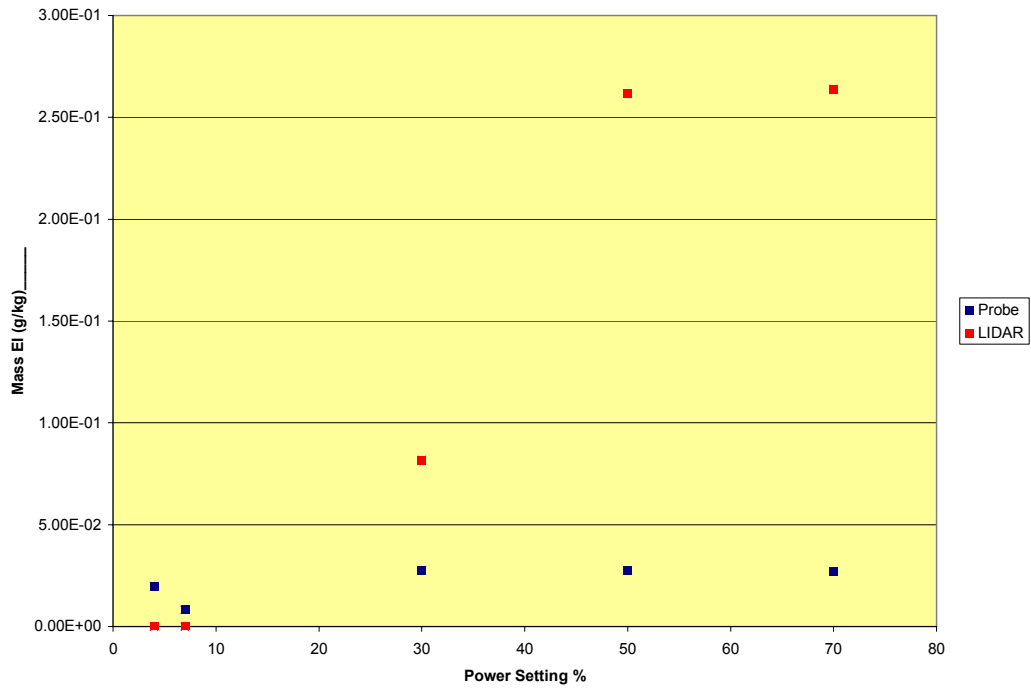
Figure 26: Comparison of LIDAR Results (Red) to Probe Sampling (Blue) for the PW2037 (second case)
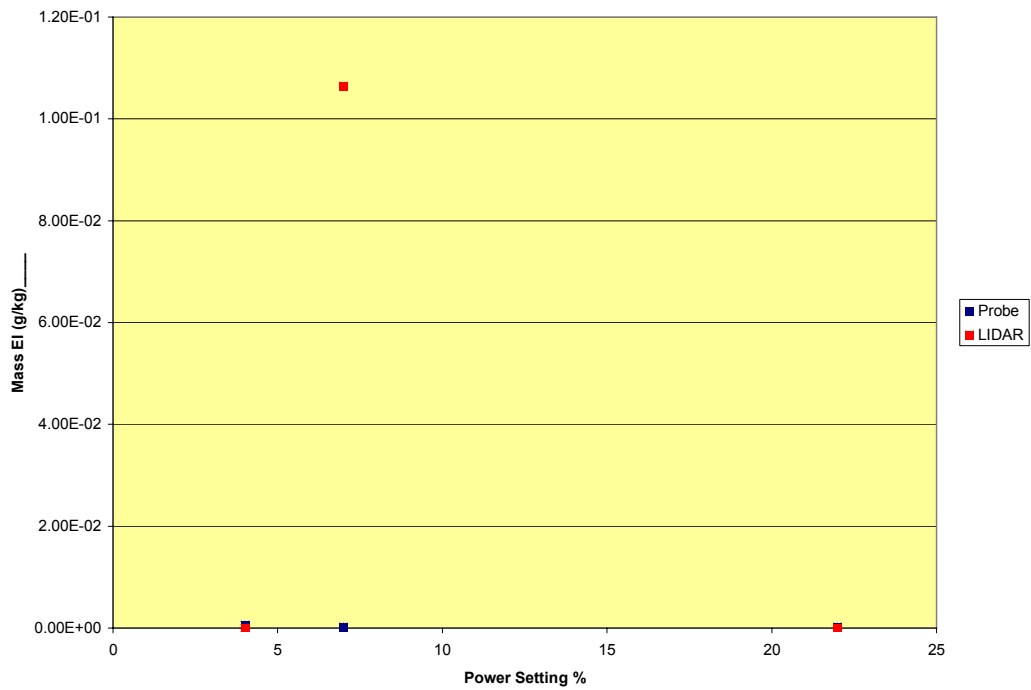
Figure 27: Comparison of LIDAR Results (Red) to Probe Sampling (Blue) for the CF6-80-C2A1
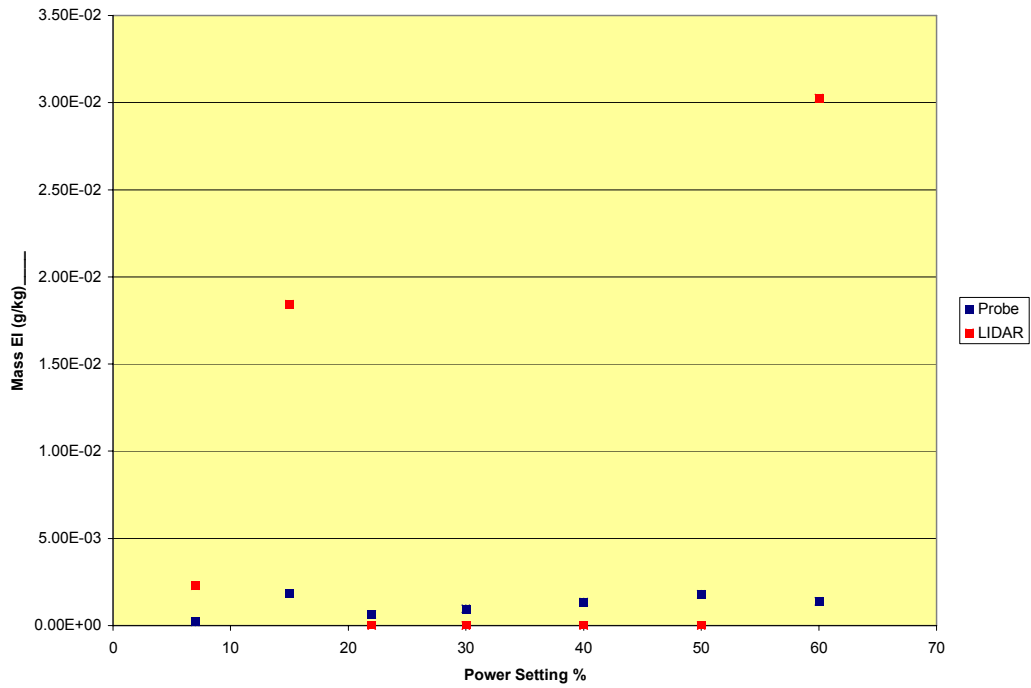
Figure 28: Comparison of LIDAR Results (Red) to Probe Sampling (Blue) for the CF6-80-C2B8
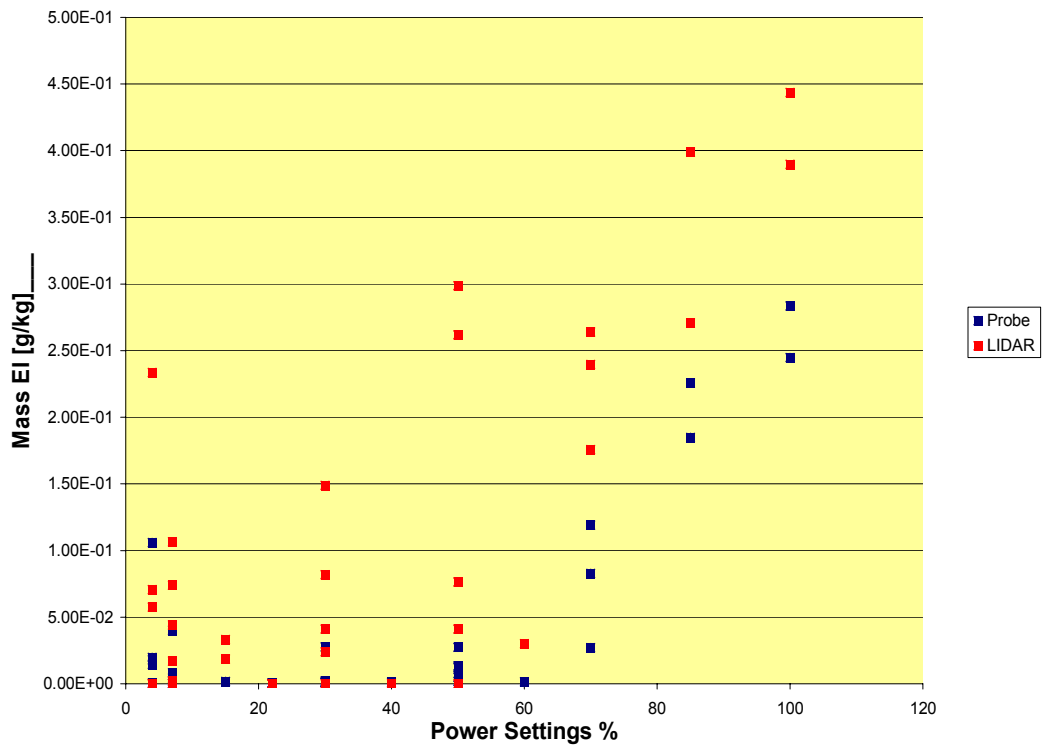
Figure 29: Scattergram of the LIDAR and Probe EIs as a function of Engine Power Setting

63
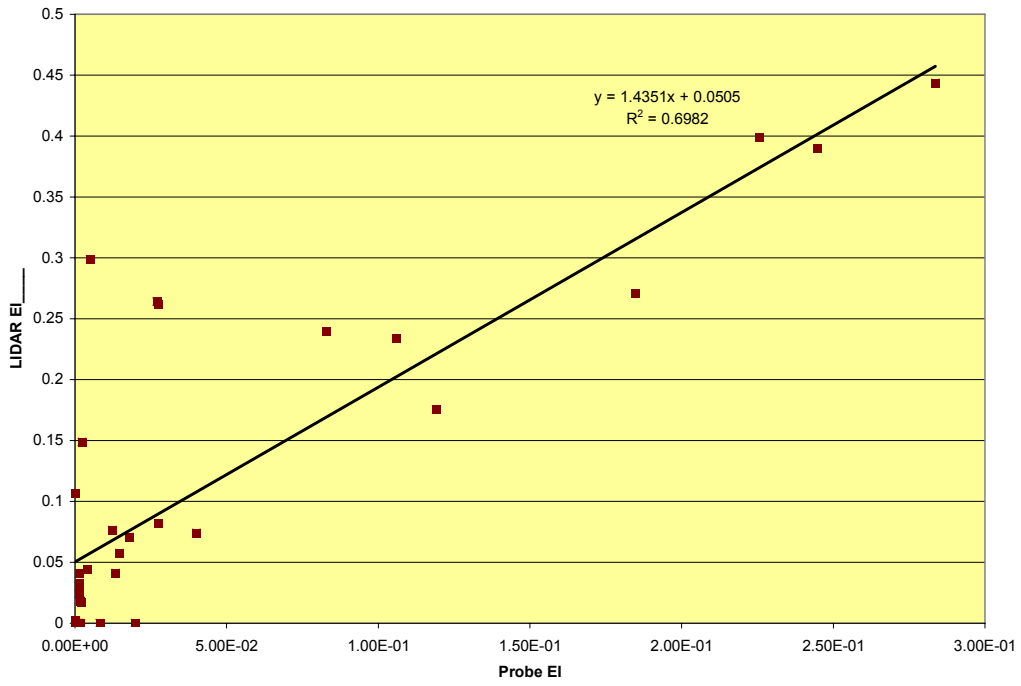
Figure 30: Correlation of the LIDAR and Probe EIs

3.2 Airport Study

Several aircraft engine plume events have been chosen and their preliminary results will be discussed. These 'showcase' events are meant to illustrate the tremendous promise a complete analysis of this data would yield. A number of questions are posed by these events and looking at the rest of the data would allow very significant statements to be made about the differences and similarities between engine technologies as well as differences and similarities to the International Civil Aviation Organization (ICAO) reference points.

3.2.1 Background Identification and Characterization

The airport environment is very dynamic in nature and there are a periods of relatively high and low frequency departures in addition to varying levels of activity at the main terminal area. Since throughout this study, the airport complex was immediately upwind of the sampling location, the background air was also changing throughout the day. This background must be quantified in order to ascertain the true emissions from aircraft related activities that were being investigated.

Background points were identified approximately every fifteen minutes by finding the relative minima of three PM quantities: average total concentration, total concentration standard deviation, and total concentration slope standard deviation. The above three quantities were calculated over 61 second time intervals with each interval matched to its midpoint. Sixty-one seconds was chosen for the width of the interval because such a duration would completely contain entire plume events (and possibly more than one event) leading to relatively higher values of all three quantities for these intervals. The quantities used for identification were chosen because the background corresponds to periods of relatively low concentration, periods of relatively small variation in the concentration, and periods of relatively small variation in the rate of change of the concentration. Figs. 31, 32, and 33 are graphs of these three quantities versus time. The six background points identified in this time interval are shown on these figures with diamond markers.

Average Total Concentration Vs. Time
(for 1 minute intervals)
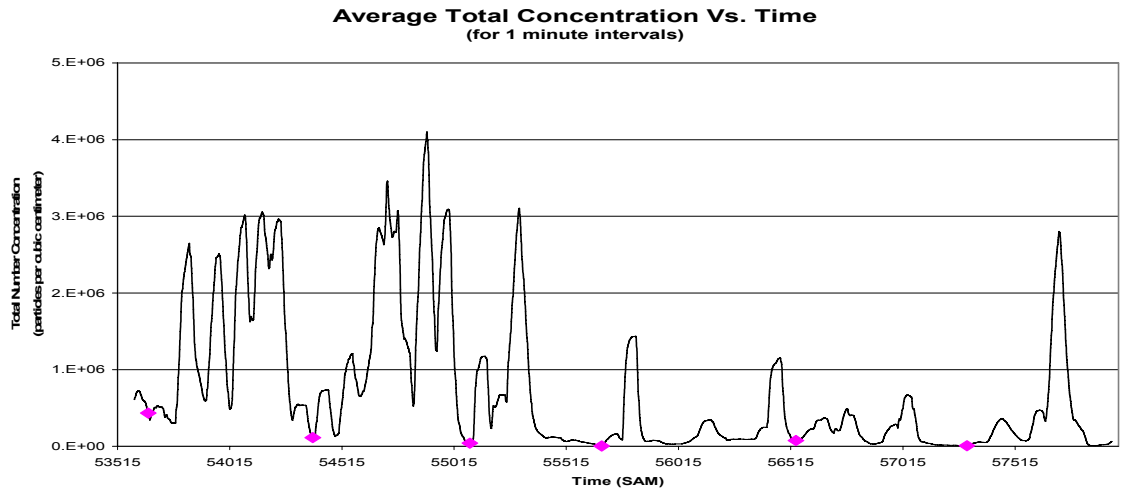
Figure 31: Average Total Concentration vs. Time (selected Background Points Shown as Pink Diamonds)

Normalized Standard Deviation of the Total Concentration V. Time
(for 1 minute intervals)
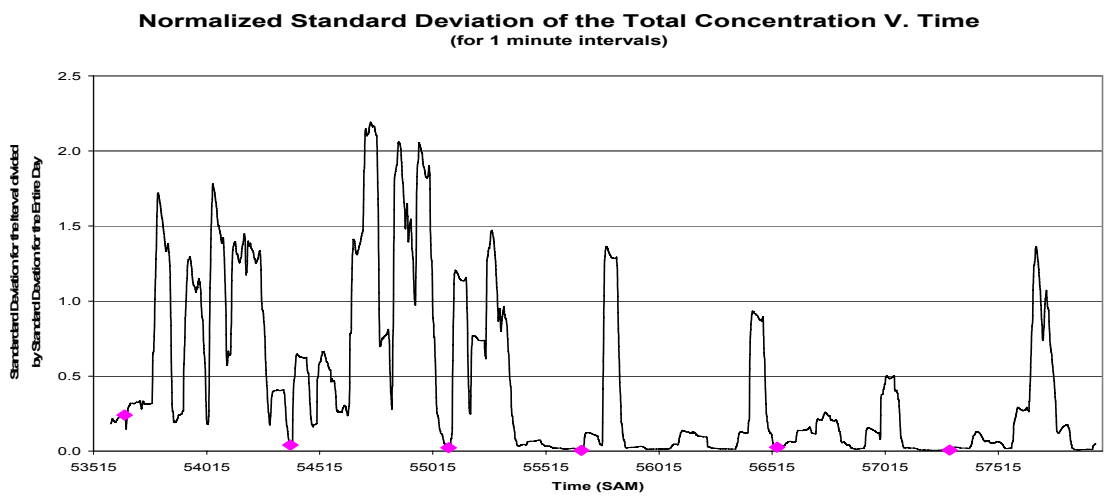
Figure 32: Normalized Standard Deviation of the Total Concentration vs. Time (selected Background Points Shown as Pink Diamonds)
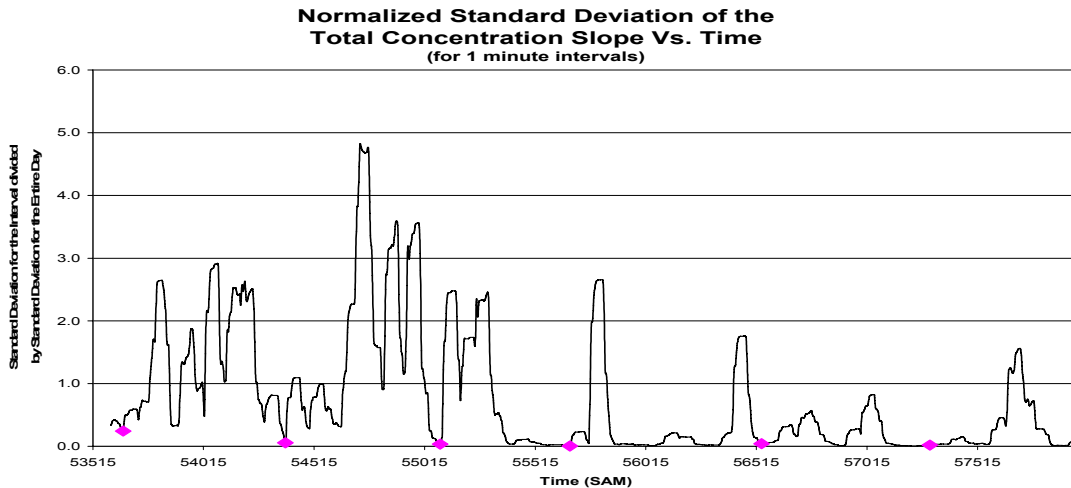
Figure 33: Normalized Standard Deviation of the Total Concentration Slope vs. Time (selected Background Points Shown as Pink Diamonds)

This same procedure was used to identify the background points for the other times and days. With all of the background points identified, the background was then characterized for each particle size measured by the DMS500. Sizes which contributed at least one-percent to the background by either number concentration or mass concentration at any point during a given day were considered a significant contributor to the background. For each of these significant sizes on an individual day, a least-squares polynomial curve fit was found as a function of time for the differential concentration of that size. The curve fitting algorithm used takes into account the uncertainty in the value at each point and can produce up to a tenth-order polynomial. Tenth through third order polynomials of the data points for a given size were compared to those data points and the order of the curve fit that was felt to best describe the data was used for that size. In other words, each significant size may have a different order polynomial describing it. All the curves corresponding to different significant sizes taken as a whole define the background for a given day and may be subtracted from the size distributions of the plume events to find each event's particulate signature as described in the previous section.

The total background concentration for a day may be found in two ways: either though a curve fit to the total background concentration data points or as a sum of the concentrations of all of the curves of the significant sizes for that day. Fig. 34 shows a comparison of these two methods and the mean of the two methods to the actual data for September 28, 2004. It can be seen that the average of the two methods reasonably closely resembles the actual data, so these values are used for the background total concentration.

67
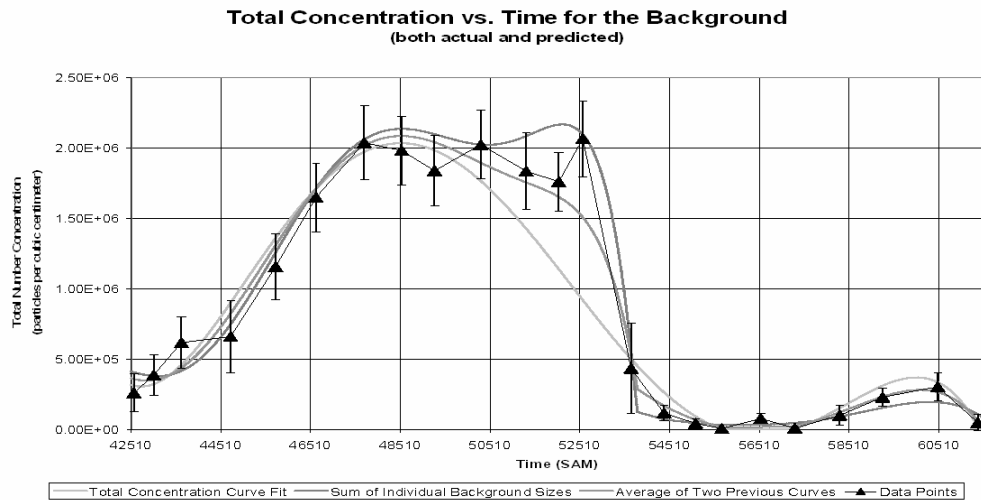
Figure 34: Background Prediction Summary as Compared to the Actual Data Points for September 28, 2004.

3.2.2 Plume Identification

In the airport portion of the study, data was acquired continuously in real-time for a period of several hours each day. From this multitude of data, events must be found and matched to the aircraft producing the emissions. Though on the surface this may seem a straight forward task, the multitude of data as well as the variance in take-off frequency necessitate a thorough strategy be developed that is more rigorous than simply "finding peaks."

Concentration profiles for a typical isolated take-off event are shown in Fig. 35. The concomitant rise in particle number and volume concentration and CO_2 concentration indicates that this event is caused by aircraft activity. From data recorded by the UMR weather station and mobile laboratory's location relative to the runway, a predicted drift time for the plume can be found for each event. This predicted drift time is then subtracted from the event start time to find an estimated take-off time for the aircraft producing the plume. This time is then compared to the recorded take-off times to correlate the plume to a particular aircraft.

This correlation of plumes to aircraft is trivial in the case of isolated events, but at a large commercial airport, the high frequency of departures and changes in the prevailing wind speed and direction make this task more difficult. In such cases, the technique employed to match plumes with aircrafts is to plot the total particle/volume concentration vs. CO_2 concentration (see Fig. 36). A regression analysis can then be performed and then slope of the line gives the emission ratio for a particular plume. For the isolated event shown in

Fig. 35, a regression analysis has been performed on the ascending as well as the descending side of the plume. In both cases, fits are quite good and indicate that this plume has not mixed with another.
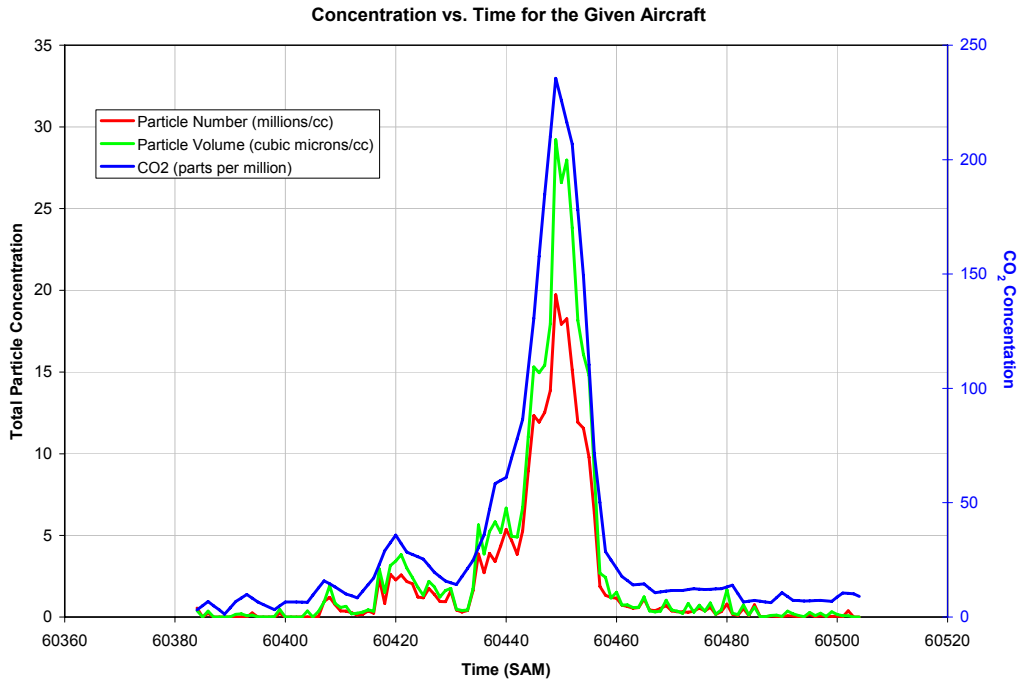
Figure 35: Concentration profiles for an isolated plume
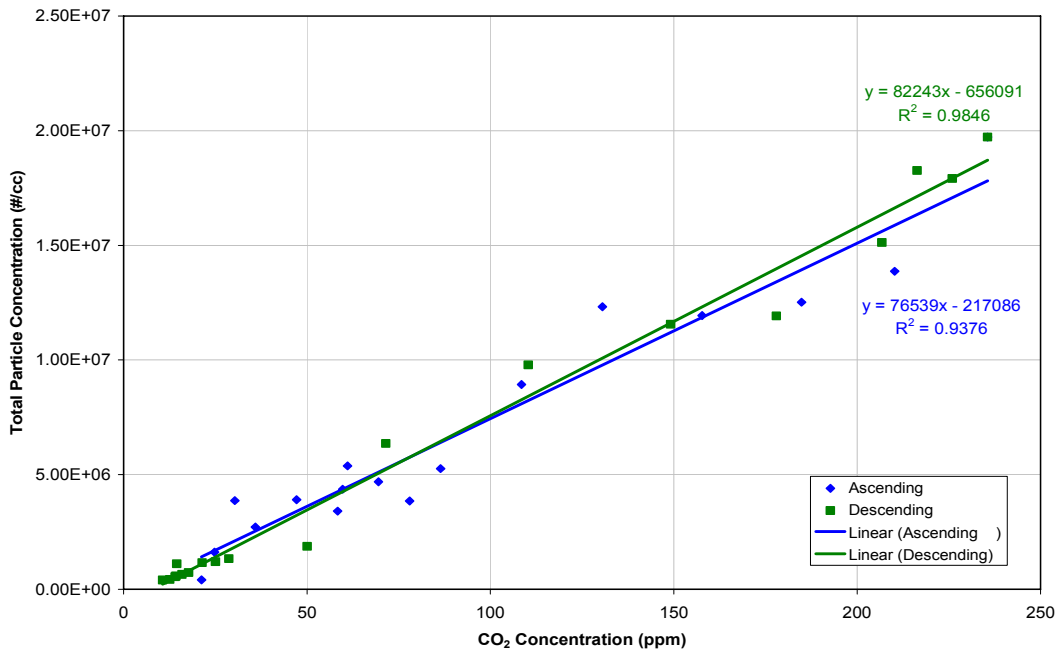
Figure 36: Total Number Concentration vs. CO_2 Concentration for a plume event shown in Fig 35.

Computation of EIn and EIm depend on the interplay between particle and CO_2 concentrations (see Fig. 36). EIn is given by the slope of the total number concentration vs. CO_2 concentration multiplied by a constant (see Eq. 6). Similarly, the EIm is given by the slope of the total mass concentration vs. CO_2 concentration multiplied by a constant (see Eq.7). The uncertainties in these emission indices are given by the standard deviations in the number (or mass) vs. CO_2 concentration points with respect to their linear fits (Fig. 36).

The correspondence between UMR and ARI of signal receipt times from departing or taxiing aircraft was good, with no definite lag in either direction between the two receipts; that is, neither UMR nor ARI consistently received a signal before the other. The use of two different methods to identify events gives more confidence in the event classification. The independent identification of plumes and their subsequent matching to aircraft by UMR and ARI yielded excellent agreement.

Those plumes which were matched to aircraft have been categorized by engine type. For all of these categorized events, the background has been subtracted from the signal in order to quantify the particulate emissions from aircraft activity on the taxiways and runways.

3.2.3 Selected Analysis

Over 500 aircraft plumes have been identified from this work. In order to evaluate the quality of this dataset, the following aircraft plume events have been selected for a preliminary analysis. The analysis teams (UMR and ARI) chose these events as representative of both datasets. They were chosen to cover a variety of engine technologies and conditions. In order to facilitate a discussion of the first results, however, the Engine Model category is represented by an alphabetic character and a number. The alphabetic character is indicative of a general class of engine such as a CFM56, a JT8D or an RB211, which the numeric character refers to a specific model within that 'class' of engine. They are listed in Table 7.

Table 7: Selected Events for Analysis

	Date	Begin Time	End Time	Airframe	Engine Model	Engine Designator	Assigned Activity
1	9/29/04	17:57:57	17:59:37			A1	Take-Off
2	9/29/04	16:20:02	16:20:49	B767-400ER	CF6-80C3B8F	A2	Take-Off
3	9/27/04	15:58:11	15:59:47	B767-300	CF6-80A2	A1	Take-Off[&]
4a	9/27/04	12:40:32	12:41:10	B747	CF6-80C2B1F	A3	Take-Off
4b		12:39:59	12:40:29			A3	Idle
4c							TaxiAccel
5	9/29/04	16:17:06	16:17:46	B737-800	CFM56-7	B1	Take-Off
6	9/27/04	12:53:22	12:54:08	B737-700	CFM56-7B20	B2	Take-Off
7a	9/29/04	16:17:48	16:19:28	A340-400	CFM56-5C4	B3	Take-Off
7b						B3	
8	9/27/04	12:33:03	12:33:34	B757-200	PW2037	C1	Take-Off
9	9/29/04	17:14:24	17:14:42	CRJ	CF34-3B1	D1	Take-Off
10	9/29/04	16:23:10	16:23:41	B717	BR715A1-30	E1	Take-Off
11	9/29/04	15:08:33	15:08:54	MD-88	JT8D-219	F1	Take-Off
12	9/27/04	16:40:02	16:41:47	MD-88	JT8D-219	F1	Take-Off
13a	9/27/04	15:14:56	15:15:35	MD-88	JT8D-217C	F2	Take-Off[&]
13b		15:13:21	15:14:15			F2	Idle

[&]These take-off plumes contain an interesting phenomenon identified by atypical emissions immediately prior to the arrival of the take-off plume. This is described more fully in the text and in this work is referred to as 'spool-up'.

3.2.3.1 Gas Phase Measurement Results

The analysis techniques are described first for the gas-phase data for the plume encounter for event #1. A time series is shown in Fig. 37. This figure depicts the mixing ratio measurements before the arrival of the plume, as the plume arrives and after it departs. The increase in carbon dioxide, CO_2 of ~ 70 ppmv (at the maximum point) is due to the

diluting plume passing by the sampling point. In addition to the increase in CO_2 this figure shows increases in carbon monoxide (CO), NO_2 and total NO_x as well as formaldehyde (HCHO). The only species shown on this figure which does not have a statistically significant increase is formic acid (HCOOH). The time response of each individual measurement is well matched with respect to each other; each has a response time less than 1.5 s. The plumes as defined by a full width half max event are much longer in duration (15 – 60 s) than the measured time responses of the various instruments (<1.5 s). These factors allow a direct determination of the emission ratio by plotting the time series data vs. CO_2. This approach to data analysis is shown in Fig.38. The data in Fig.38 shows remarkable correlation between the NOx and CO_2. The concomitant rise of both NOx and CO_2 is so good that two lines appear to emerge. The greater of the two is associated with the take-off of the aircraft in question, Event #1 (N126DL). The lesser of the two may be due to a previous take-off or a taxiway acceleration arriving during this plume event. The entire event emission ratio is (7.5 ± 0.3) ppbv ppmv^{-1} while the central plume value is $\sim 11\%$ greater, (8.3 ± 0.5) ppbv ppmv^{-1}. This underscores the need to very carefully regard this data in order to maximize the accuracy of the analysis. We are in the process of using multiple approaches in the analysis in order to flag anomalous results within an event. This will allow an automated analysis to process the very large number of plumes within this dataset as well as note which events require additional study for the greatest accuracy and understanding of the method.

Two of the particulate emissions measurements are shown vs. time in Fig. 39 for the same event discussed previously. This figure depicts the total particulate number as measured by the condensation particle counter (CPC) in the top panel. The middle panel shows the preliminary result for the Multi-Angle Absorption Photometer (MAAP) vs. time. In the lowest panel, the CO_2 concentration in the solid line as well as the CO_2 and NO_x from gas-phase inlet (dashed lines) are shown vs. time. An isokinetic split, within the mobile laboratory is used to minimize any biasing of the particle size distribution, however it is estimated that only ~90% of the particle greater than 7nm are transmitted to the CPC instrument. Particles smaller than 7nm are not detected by the CPC. The MAAP black carbon mass, and as a result it is estimated that 99% of the particle sizes which contribute to the mass measurement are transmitted from the inlet to the instrument within the mobile laboratory. None of these measurements has been corrected for the estimated losses within the truck. Note that a cyclone on the inlet prevented particles larger than 2.5 μm from reaching these instruments. Once the non-refractory components of the mass (as measured by the Aerosol Mass Spectrometer) are quantified, the sum of the two mass measurements in the mobile laboratory will very closely reflect a measurement of PM2.5.

The shaded region in Fig. 39 reflects a very different black carbon and total number count from the non-shaded portion. This corresponds to the same issue detected in the analysis of the gas-phase data. A detailed examination of the notes and video indicate that the plume from the previous take-off is influencing the initial portion of this 'event'. The time series data for these particulate measurements is plotted vs. the dilution fiduciary in Fig. 40. The 'hollow' points in this figure correspond to those points within the shaded

region in Fig. 39 and are not included in the least-squares fits. The results of these fits are presented for this event #1 together with all of the events identified for the selected analysis in Table 8. This table shows the Engine Model, the NO_x emission index, the inferred thrust, the CO emission index, the inferred ICAO CO emission index, the HCHO emission index, the CPC particle number based emission index and the MAAP black carbon emission index. The thrust column has been computed by comparing the measured NO_x emission index to ICAO reference points. This metric has been computed only to provide a simple basis for comparison. The data in this table is shown visually in Fig. 41. The lowest panel shows the NO_x emission index results. The thrust has been computed from ICAO-NO_x and this result might be regarded as a self-fulfilling trend. This figure demonstrates it usefulness is portraying the CO and HCHO data. The middle panel of Fig. 41 shows the emission indices for CO in green and HCHO in red. The top panel shows two of the particulate emission metrics, the CPC in magenta/pink and MAAP black carbon in black. Unlike the gas-phase data a clear trend does not immediately emerge in this figure. The MAAP black carbon data is shown in Fig. 42. In this case, the style of point marker indicates the engine type. Because engine type A and F each had over four occurrences within that class of engine covering the range of estimated thrust, trend lines have been included. This figure shows that engine technology may be the strongest driver for gauging mass-based emission indices.

The SMPS records a particle size distribution over its measurement interval. For this work, one minute sweeps were used to record number count vs. diameters covering 18-500 nm. Previous figures show that that timescale of plume arrival is not at all consistent for an entire minute. As a result, capturing a representative size distribution in a single plume using the SMPS is not feasible. This does not mean that it is not a useful measurement though. In Fig. 43, multiple plume encounters have been averaged and binned according to the 1s data for several hours of data on the 27th. Six different size distributions are calculated according to three concentration steps of excess CO_2 and a binary pair of HCHO emission indices. The size distributions shown by the triangles are those when the estimated HCHO emission index was greater than 50 mg kg^{-1}. The size distributions depicted with solid circles are when the HCHO emission index is less than 50 mg kg^{-1}. Due to the trend in Fig. 41, it is reasonable to assume that the excess CO_2 in the size distributions represented by triangles are due to 'idle' and the circles are 'take-off'. Fig. 43 reveals a qualitative difference in the averaged size distributions between these two modes of operation. The 'idle' plumes contain an actively nucleating 'ultrafine' mode at ~ 25 nm while the 'take-off' plumes appear to have a larger 'soot' mode at 50-70 nm. This is consistent with the findings published recently which used a different instrumentation package (Herndon et al., 2005). The algorithm used to generate this figure could benefit greatly from further refinement; however, the initial analysis indicates that important statements about the nature of the emissions under different operational conditions can be made.
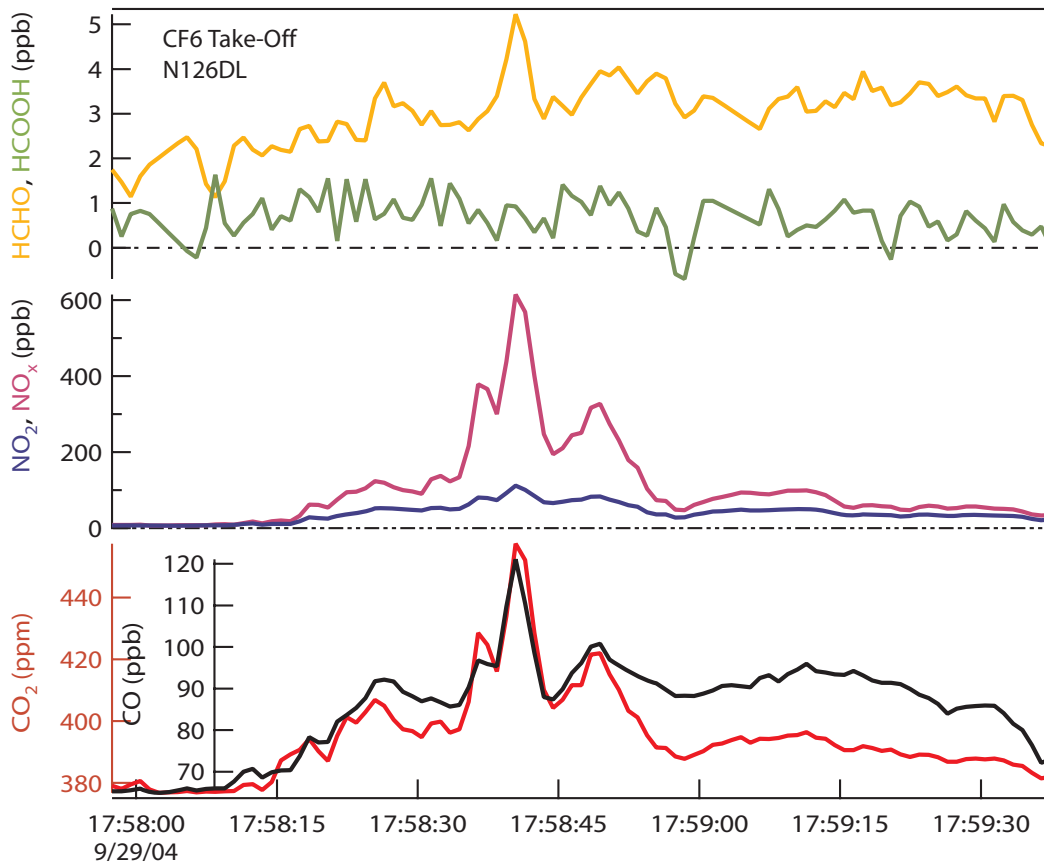
Figure 37: Gas-phase time series for a take-off plume

The data shows various gas-phase species before and after the take-off plume due to N126DL. The CO_2 and CO data is shown on the lowest panel in units of ppmv and ppbv respectively. On the middle panel, the direct NO_2 measurement is depicted in blue while the total of NO and NO_2, or NO_x is the magenta trace. Note that the NO_2/NO_x ratio is lowest during the heart of the plume. On the top panel, formaldehyde, HCHO (orange) and formic acid, HCOOH (green) are shown in ppbv.
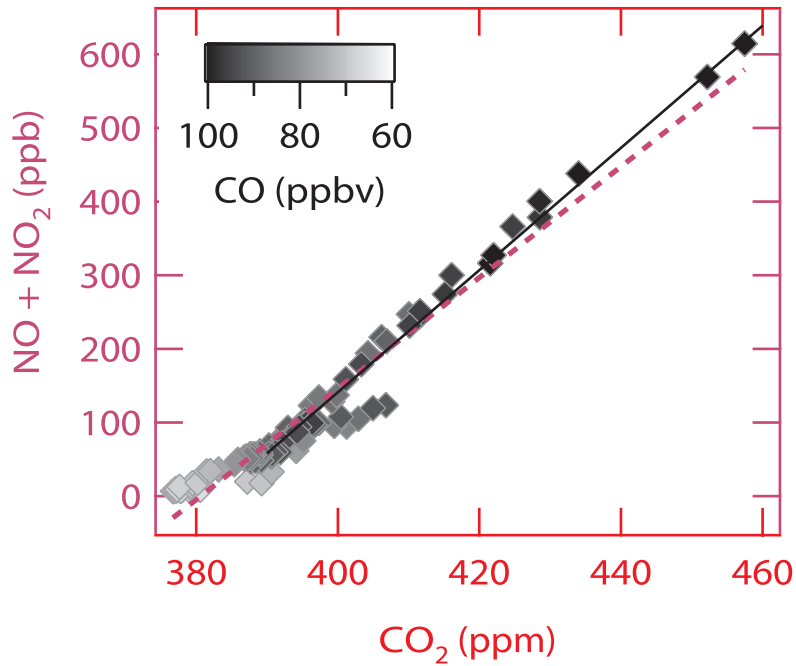
Figure 38: NOx vs. CO$_2$ for a take-off plume

The total NOx, computed by summing the 1s NO and NO$_2$ measurements is plotted vs the 1s measurements of CO$_2$ for the data shown in Figure 1. The NOx data points are shaded according to the 1s CO measurements. Two fits, one for the entire event (dashed magenta) and one for only the central plume (solid black) are shown. See text for additional details.
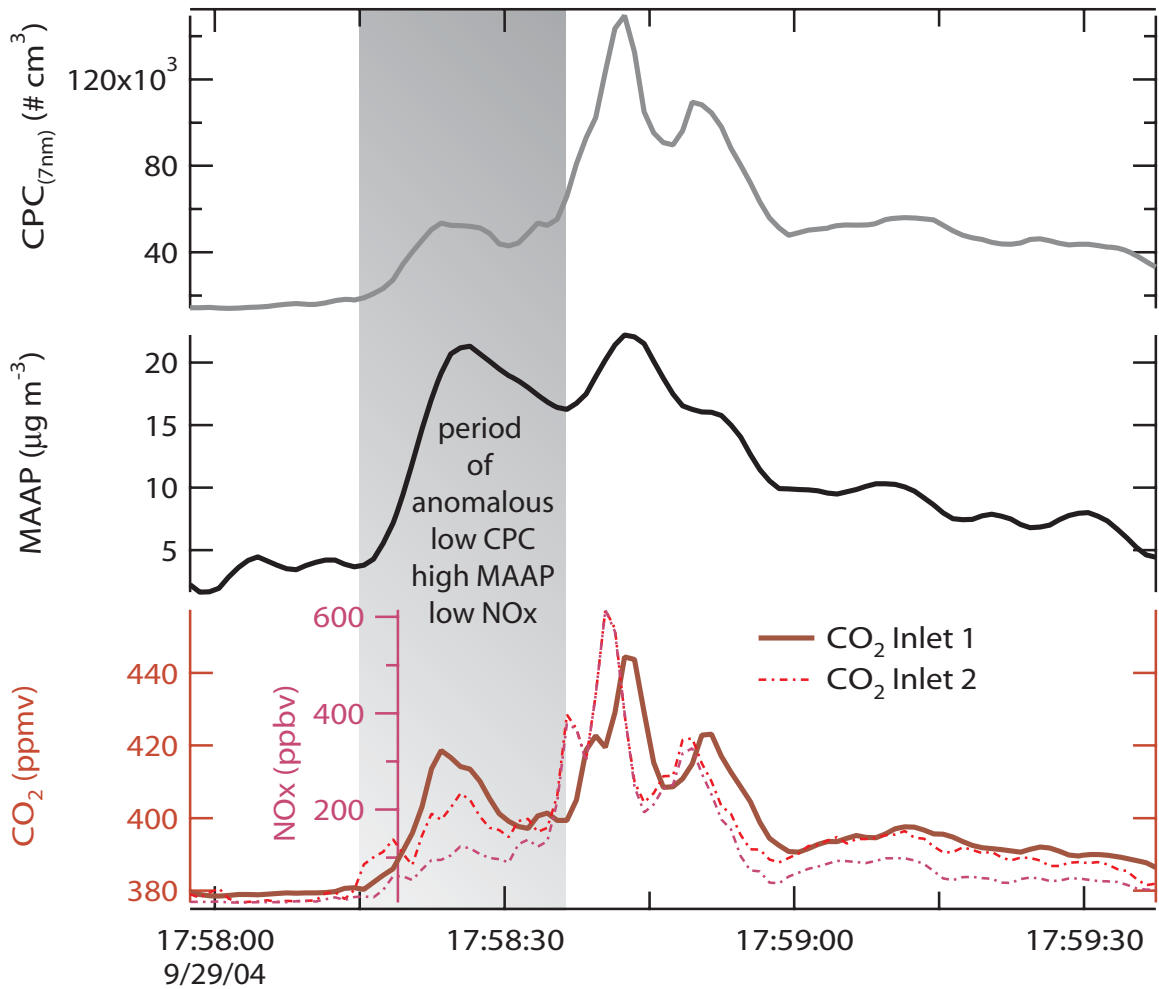
Figure 39: Time series of the Particulate data

The figure shows the time series of the condensation particle counter (CPC), the multi-angle absorption photometer (MAAP) and CO_2 measurements on Inlet #1. Repeated data from a previous figure is shown from the gas-phase NOx and CO_2 measurements. Note that the two CO_2 measurements are lagged by ~3 seconds but they show very good agreement during the entire plume event. The shaded region labeled 'period of anomalous...' is described in the text.
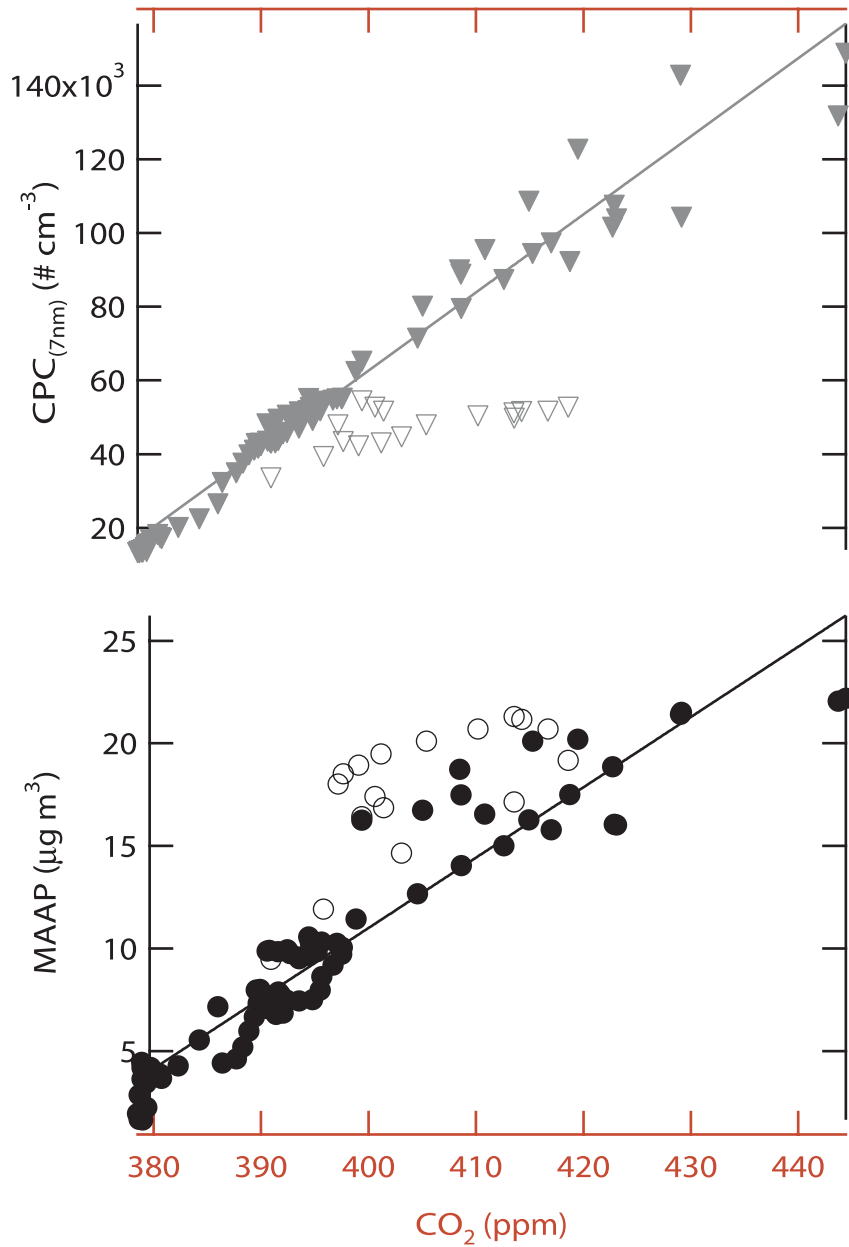
Figure 40: Correlation Figure of Particulate Measurements with CO_2

This figure shows the 1s CPC (grey, top panel) and the 1s MAAP (black, bottom panel) data plotted vs CO_2. The open symbols have been excluded from the fit and are indicated by the shaded region of a previous time series figure. See text for quantification of the EI_n and EI determined from this plot.

Table 8: Selected Events Analysis Results

Engine Model	NOx (g kg^{-1})	Thrust[1]	CO (g kg^{-1})	ICAO CO[2] (g kg^{-1})	HCHO (mg kg^{-1})	CPC EI$_n$ (# kg^{-1})	BC[3] EI (g kg^{-1})
A1	27.4±1.6	89%	1.0±0.1	1.07	65±7	3.7×10^{15}	0.59±0.06[29]
A2	20±0.9	83%	0.2±0.07	0.5	0 ± 6	9.0×10^{15}	0.12±0.02[29]
A1	19.4±0.7	61%			31±4	5.0×10^{15}	0.48±0.08[27]
A3	1.7±0.3	<7%	59±2		506±35	4.3×10^{15}	0.03±0.03
A3	15.6±0.7	68%	0.9±0.4		20±12	2.7×10^{15}	0.24±0.03
A3	2.8±0.7	6%	31±7		243±8	6.0×10^{15}	0.02±0.04
B1	7.2±0.9	<30%	3.1±0.2		84±24	6.8×10^{15}	0.27±0.04
B2	12±1	~45%	1.4±0.3		164±20	2.4×10^{15}	0.26±0.11
B3	27±1.6	83%	1.2±0.2		6±7	1.1×10^{16}	0.52±0.6
B3	2.7±0.5	<7%	40±8		452±86	7.5×10^{15}	0.06±0.1
C1	30.4±1	98%	0.2±0.07	0.4	25±9	2.5×10^{15}	0.52±0.02
D1	5.5±0.6	<30%	1.2±0.2		16±13	3.0×10^{15}	0.45±0.10
E1	16.2±0.7	79%	1.1±0.4		5±24	8.5×10^{15}	0.61±0.11
F1	13.8±0.6	85%	0.8±0.1		0±40	1.9×10^{15}	2.1±0.2
F1	14.5±0.7	87%	1.6±0.2		98±24	2.2×10^{15}	1.4±0.1
F2	9.0±1.0	~45%	2.5±0.4		53±10	4.0×10^{15}	1.7±0.1
F2	2.6±0.3	8%	11±0.6		222±30	5.0×10^{15}	0.35±0.05

[1]ICAO Thrust is computed from the measured NOx EI, assuming a linear relationship between the defined 100% and 85% ICAO data points for the listed engine.

[2]ICAO CO is computed (for take-off) by matching the ICAO Thrust (in this table) to an exponential fit of the 30%, 85% and 100% ICAO data.

[3]These BC number have not been quality assured. The raw data needs to be re-run in the latest MAAP/Petzold formulation as well as flow rates verified. They have all been computed from fixed parameters, though and can reveal useful trends within the category.
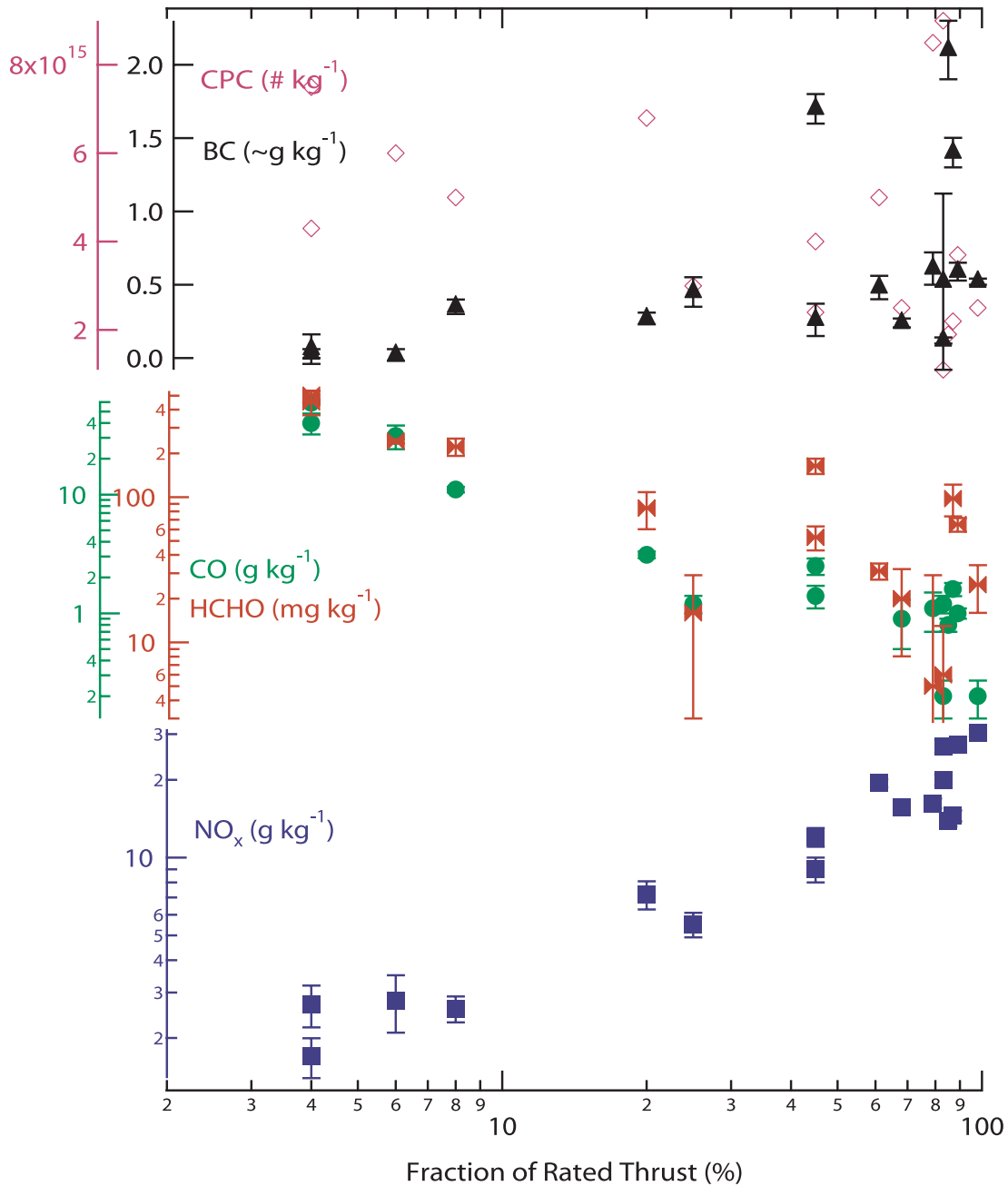
Figure 41: Summary of Emission Indices

This figure shows the emission index for various species, NOx, CO and HCHO, CPC and BC vs. the fraction of rated thrust. Starting from the bottom, NOx is shown in blue. CO and HCHO are depicted in the middle panel in green and red respectively. On the top panel, the CPC and ~BC emission indices are shown in magenta and black respectively. See text for a more complete discussion of this figure.

79
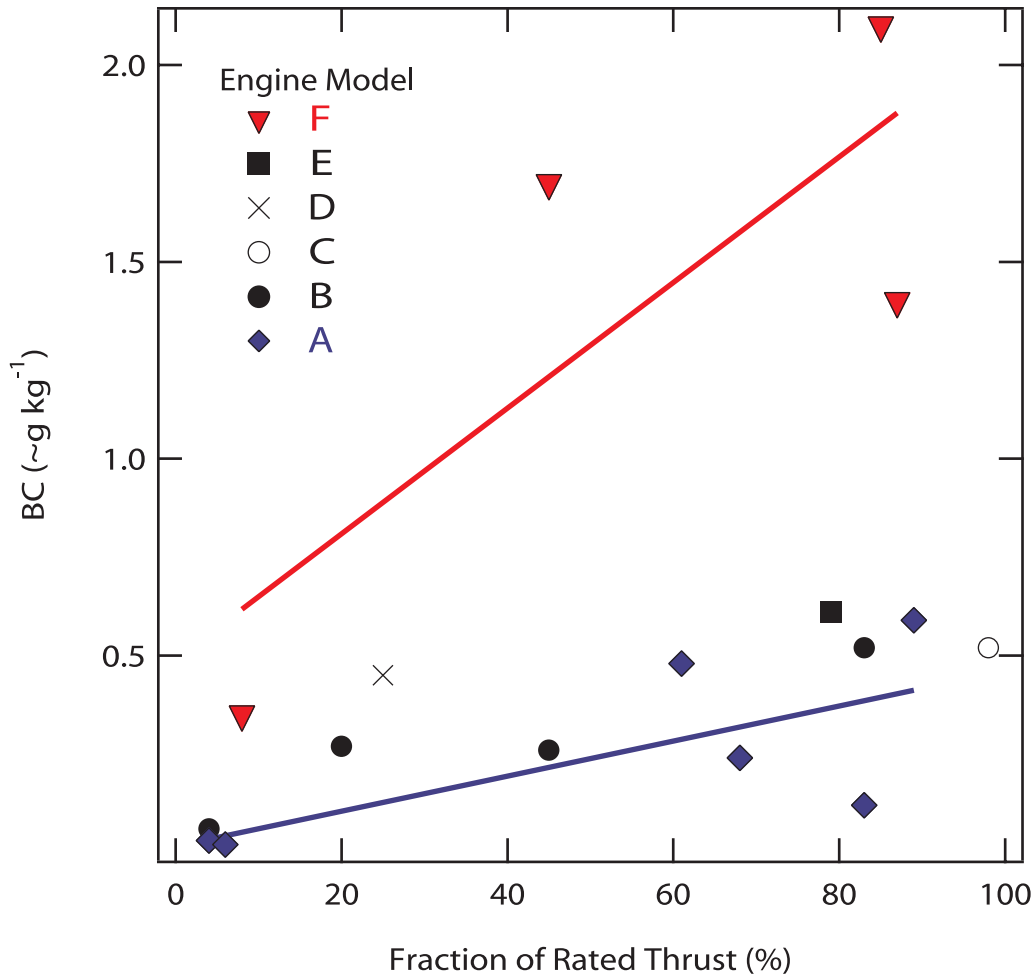
Figure 42: MAAP Black Carbon Emission Index

The MAAP black carbon emission index is result is plotted vs. fraction of rated thrust for various types of engines. The red triangle data and red trend line depict the four results for the engines of type "F". The blue diamonds and blue trend line show the six results for the engines of type "A". The figure shows that black carbon emissions may be a strong function of engine model.
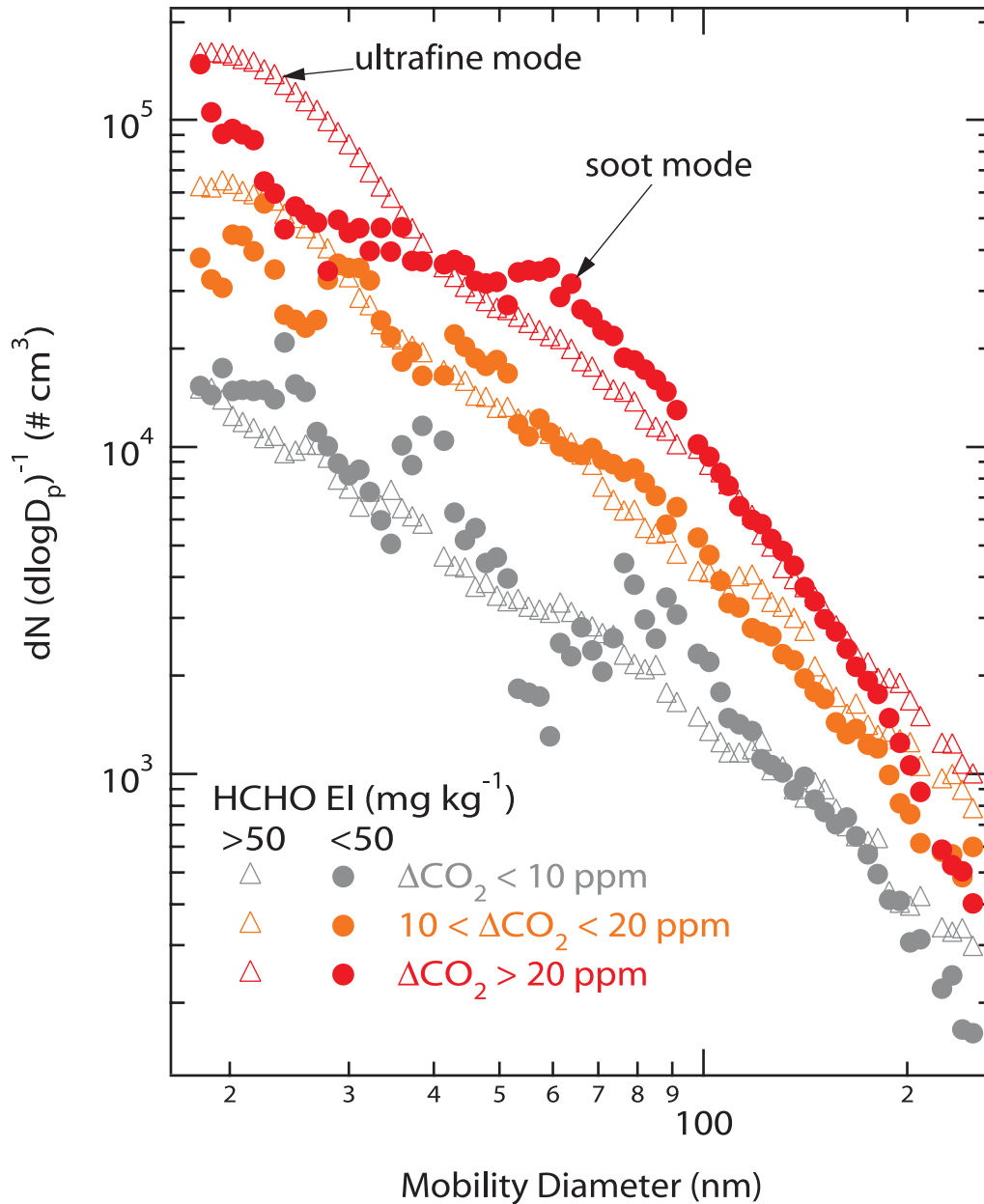
Figure 43: Average Size Distributions based on CO_2 and HCHO Emission Index

This figure shows some average size distributions derived from the scanning mobility particle sizer (SMPS) data. The algorithm used to sort the 'slow' SMPS data (1 sweep every minute) using the 1s measurements of HCHO and CO_2 is described in the text. When the HCHO emission index is greater than 50 mg kg^{-1}, it is presumably due to an engine operating at low thrust. This figure shows an 'ultra fine' mode (<25 nm) indicative of low thrust and a 'soot' mode emerging at ~65 nm which is presumably due to higher thrust settings.

3.2.3.2 PM Physical Characterization Results

The "show-case" events are categorized by engine type so that they might be compared and trends for each engine type can possibly be identified. Table 9 summarizes pertinent information that can be gleaned from the UMR analysis of events.

Table 9: Summary of the Important Characteristics and Identifiers for Each of the Sample Events

Date	Time	Airframe	Engine	ARI Engine Designation	Peak Number Concentration	Peak Volume Concentration	Peak CO2 Concentration Delta	Primary Number Mode Peak Size	Small Particle Volume Mode Peak Size	Large Particle Volume Mode Peak Size
					(Mparticles/cc)	(μm^3/cc)	(ppm)	(nm)	(nm)	(nm)
9/27/2004	12:40:00	747	CF6-80C2B1F	A3	12.8	14.5	176	7.5	12	130
9/27/2004	15:58:21	767-300	CF6-80A2	A1	11.4	19.9	188	7.5	11	75
9/29/2004	16:19:49	767-400ER	CF6-80C2B8F	A2	15.7	10.6	--	7.5	10	55
9/27/2004	12:52:47	737	CFM56-7B20	B2	11.0	7.0	104	7.5	14	85
9/29/2004	16:16:34	737-800	CFM56-7	B1	6.9	12.9	114	8.5	11	55
9/29/2004	16:17:31	A340-400	CFM56-5C4	B3	13.9	15.5	145	7.5	14	55
9/27/2004	15:14:47	MD-88	JT8D-217C	F2	14.1	36.1	197	7.5	10	90
9/29/2004	15:07:57	MD-88	JT8D-219	F1	178.0	131.0	594	6.5	10	130
9/29/2004	16:40:41	MD-88	JT8D-219	F1	3.5	42.4	207	5.6	20	75
9/27/2004	12:32:26	757-200	PW 2037	C1	8.9	10.6	138	7.5	10	75
9/29/2004	16:22:45	717	BR715A1-30	E1	11.8	14.8	83	7.5	10	55
9/29/2004	17:13:28	CRJ	CF34-3B1	D1	3.6	8.0	48	5.6	5.6	55

There are three plots associated with each event identified in the table above. The first of these plots shows the total number concentration in millions of particles per cubic centimeter of air, the total volume concentration in cubic microns of particles per cubic centimeter of air, and the carbon dioxide concentration in parts per million versus time in seconds after midnight local time of the given day. This plot also indicates the time period during which the event is received by bold lines and a double arrow. The second is a plot of differential number concentration of particles versus time, while the last is a plot of the differential volume concentration of particles versus time. Each set of plots for each event includes a bulleted list of important features.

Sample Event 1

Boeing 747 Airframe with CF6-80C2B1F Engines
9/27/2004   12:40:00
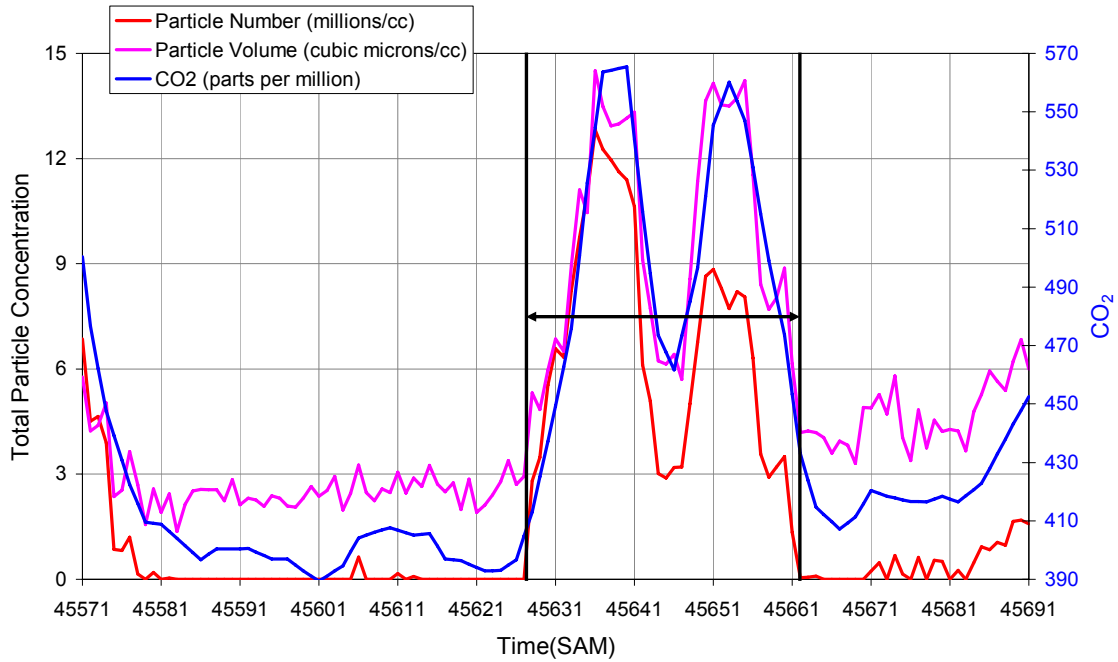
Figure 44a: Sample Event 1 - Total Particle Concentration (Number and Volume) and CO₂ Concentration as a Function of Time

- This take-off event spans times from 45627 to 45662 SAM and has two peaks possibly because this is a four engine aircraft.
- The second peak is weaker in number concentration because it has had about 15 seconds longer to disperse with the ambient air and/or the small particles have agglomerated into larger ones.
- The second peak has a larger average size for the small particle volume mode because the longer travel time has allowed more agglomeration to occur.

Figure 44b: Sample Event 1 - Particle Number Concentration Size Distribution as a Function of Time

Figure 44c: Sample Event 1 - Particle Volume Concentration Size Distribution as a Function of Time

Sample Event 2

Boeing 767-300 Airframe with GE CF6-80A2 Engines
9/27/2004   15:58:21

Figure 45a: Sample Event 2 - Total Particle Concentration (Number and Volume) and CO_2 Concentration as a Function of Time

- This take-off event spans times from 57517 to 57545 SAM and is a "spool" event (as identified from compositional measurements made by ARI) in which the engine proceeds from low power to high power.
- The "spooling" is evident from the lack of the normally sharp leading edge at event arrival and by the two larger particle volume modes the smaller of which corresponds to lower power and the larger to high power.
- There is a clear and distinct shift in particle size once a certain engine power is reached at about 57528 SAM.

Figure 45b: Sample Event 2 – Particle Number Concentration Size Distribution as a Function of Time

Figure 45c: Sample Event 2 - Particle Volume Concentration Size Distribution as a Function of Time

86

Sample Event 3

Boeing 767-400ER Airframe with CF6-80C2B8F Engines
9/29/2004   16:19:49

(NOTE: CO_2 data absent from 58781 to 58838 because of instrument calibration)

Figure 46a: Sample Event 3 - Total Particle Concentration (Number and Volume) and CO₂ Concentration as a Function of Time

- This take-off event spans 58817 to 58849 and does not have complete carbon dioxide information because of instrument auto-calibration.
- This event exhibits typical behavior in its sharp leading edge at arrival and slower declination thereafter.
- This event's volume concentration is dominated by the small particle mode which is somewhat atypical.
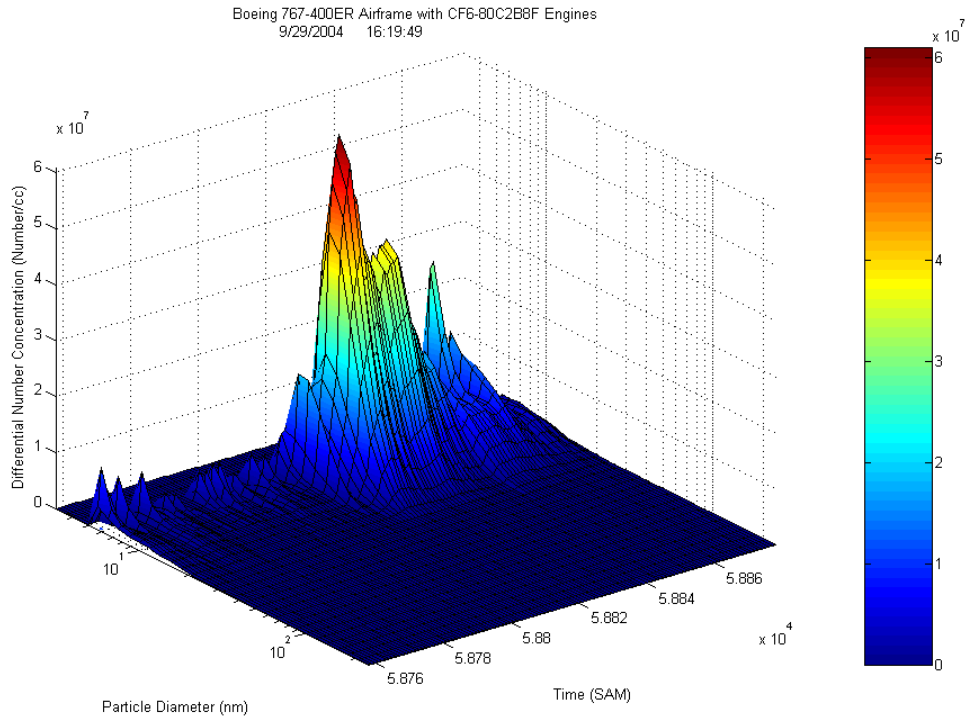
Figure 46b: Sample Event 3 – Particle Number Concentration Size Distribution as a Function of Time

Figure 46c: Sample Event 3 - Particle Volume Concentration Size Distribution as a Function of Time
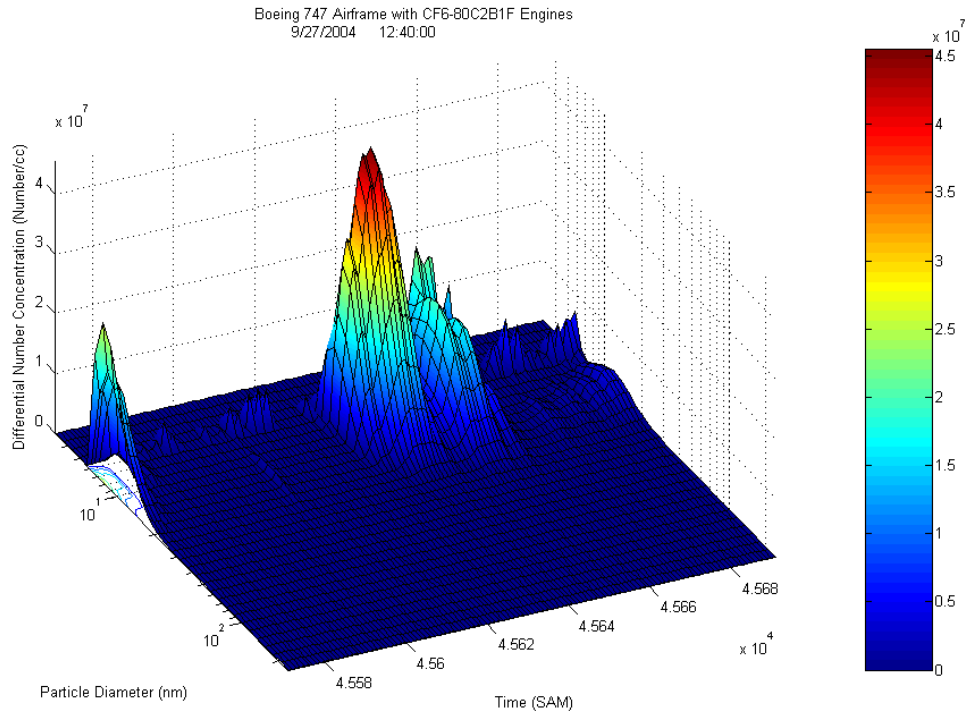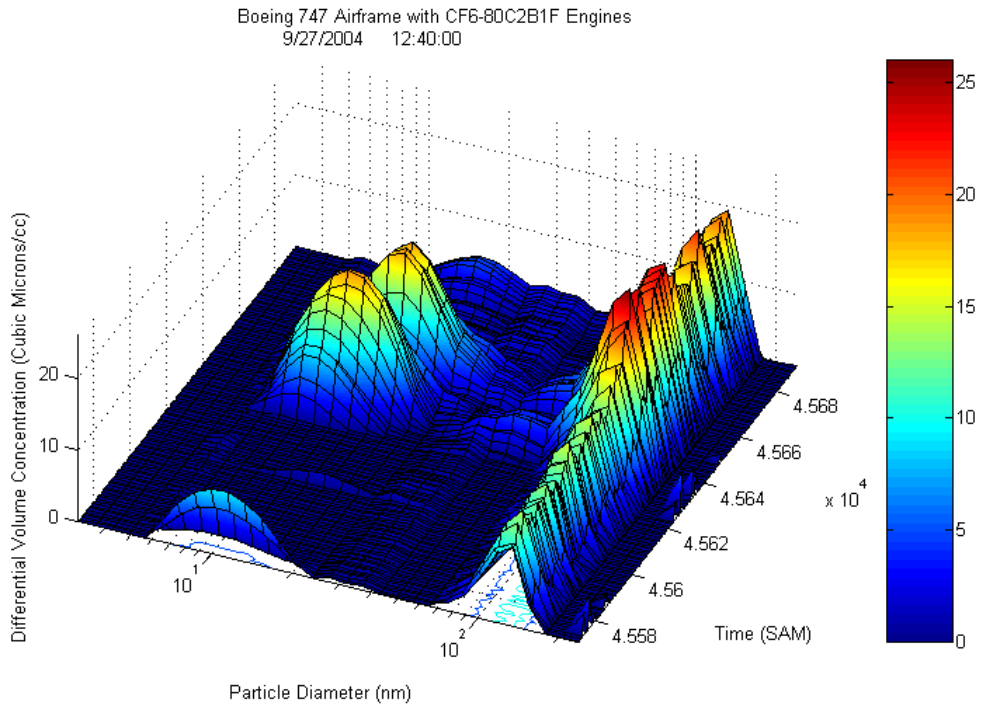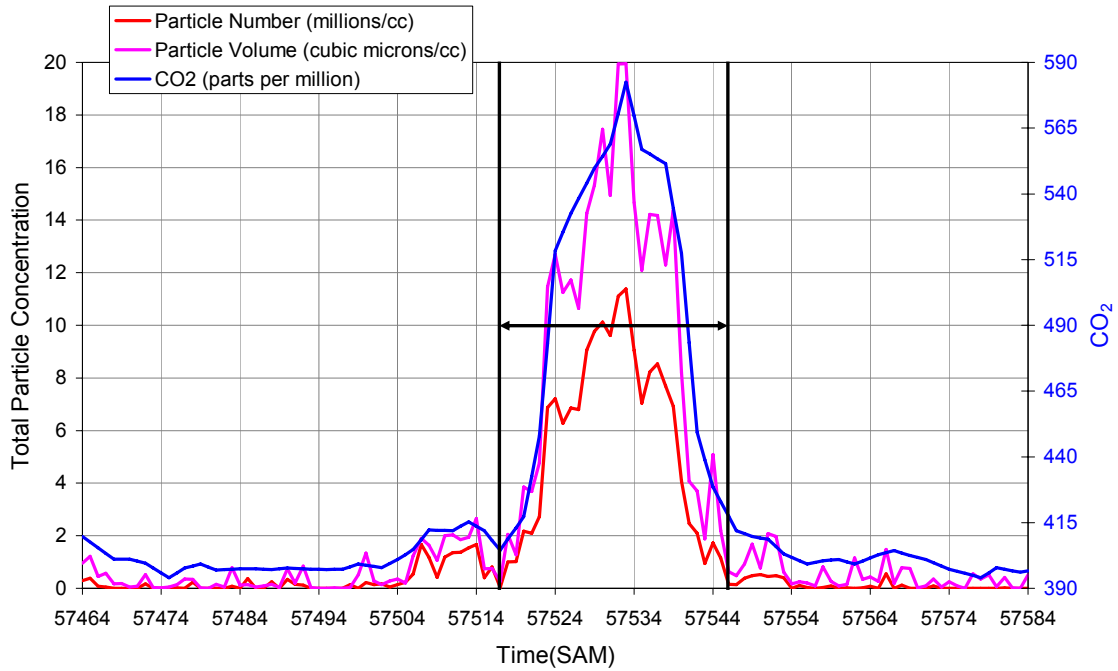
Sample Event 4

Boeing 737 Airframe with CFM56-7B20 Engines
9/27/2004   12:52:47
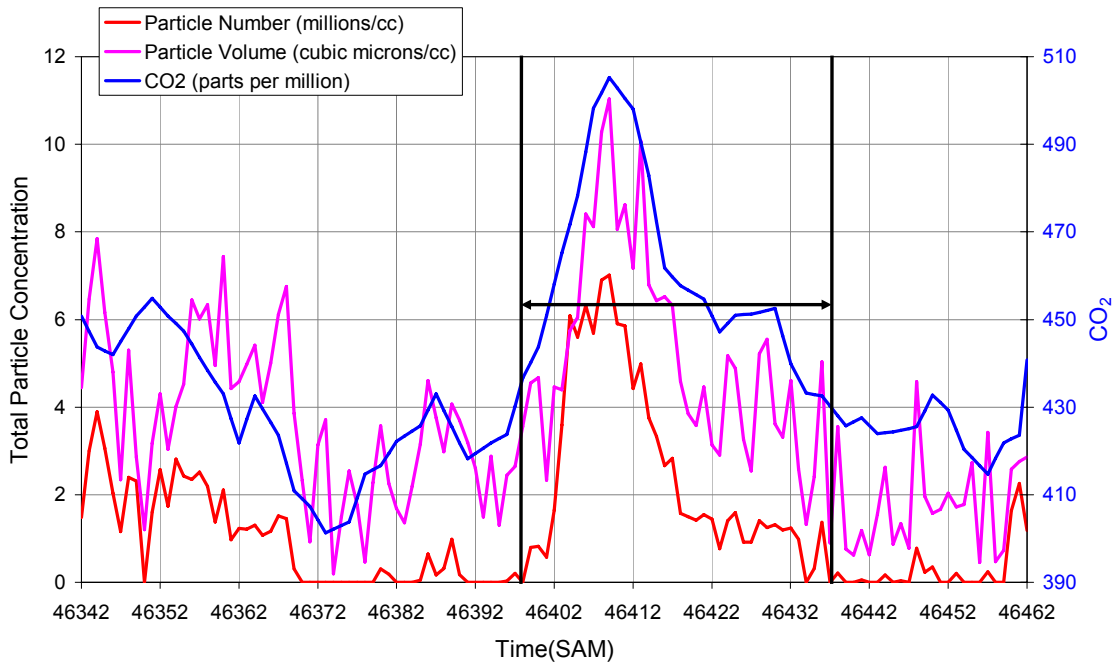
Figure 47a: Sample Event 4 - Total Particle Concentration (Number and Volume) and CO_2 Concentration as a Function of Time

- The takeoff event spans 46398 to 46437 and is a typical take-off plume.
- This take-off event shares large and small particle volume modes of like magnitude.
- This take-off event occurred during a high take-off frequency period which accounts for the great fluctuations both preceding and following it; these fluctuations are due to mixing of multiple aircraft emissions, which is unavoidable during high departure frequency.
- This take-off plume is 39 seconds long while event activity during this time corresponds to one event approximately every 50 seconds.

Figure 47b: Sample Event 4 – Particle Number Concentration Size Distribution as a Function of Time

Figure 47c: Sample Event 4 - Particle Volume Concentration Size Distribution as a Function of Time
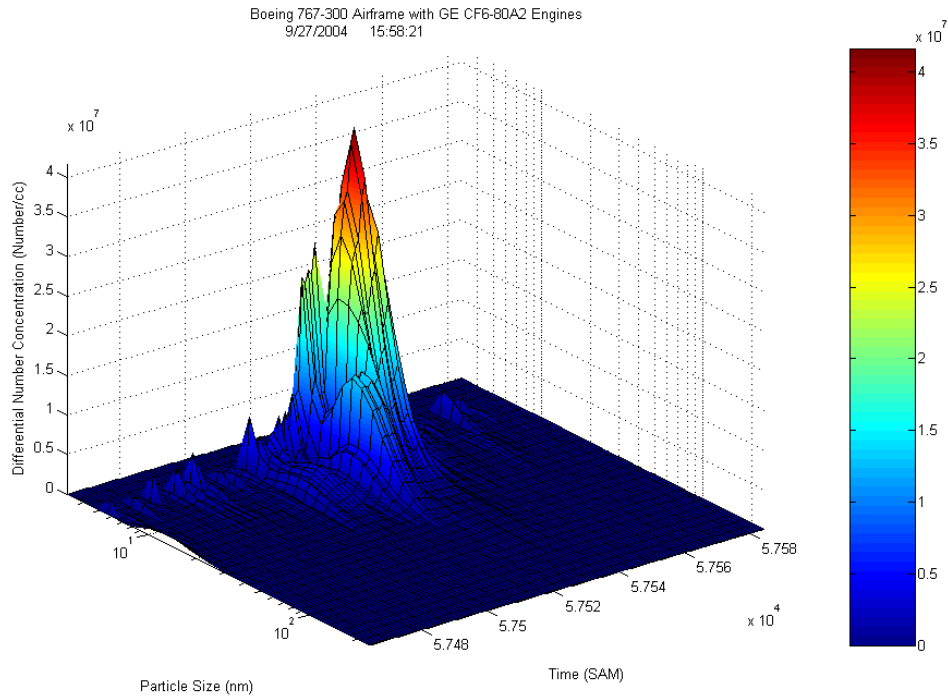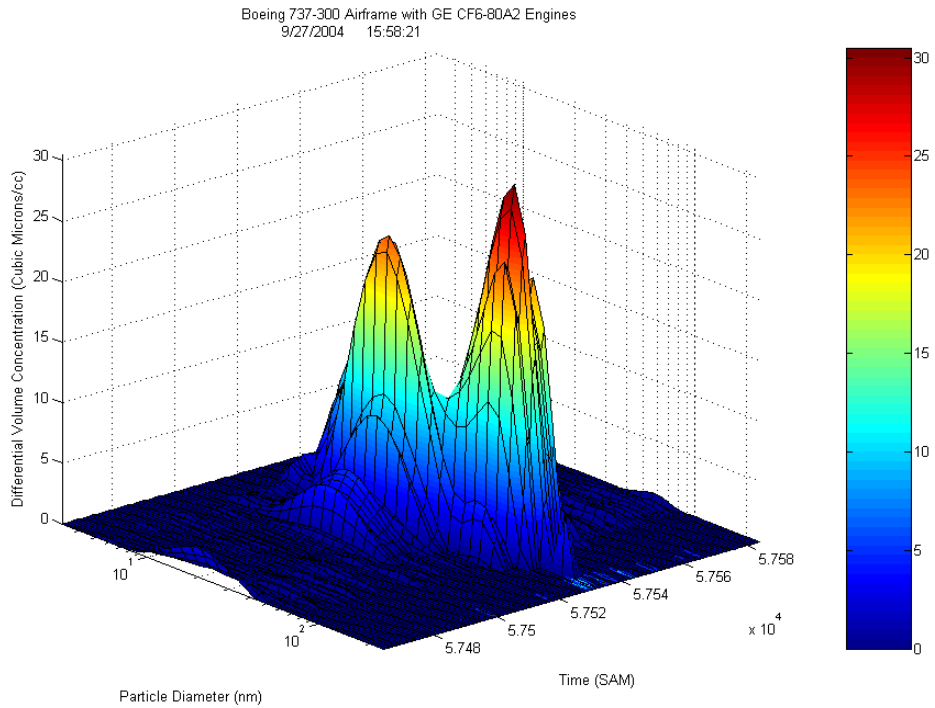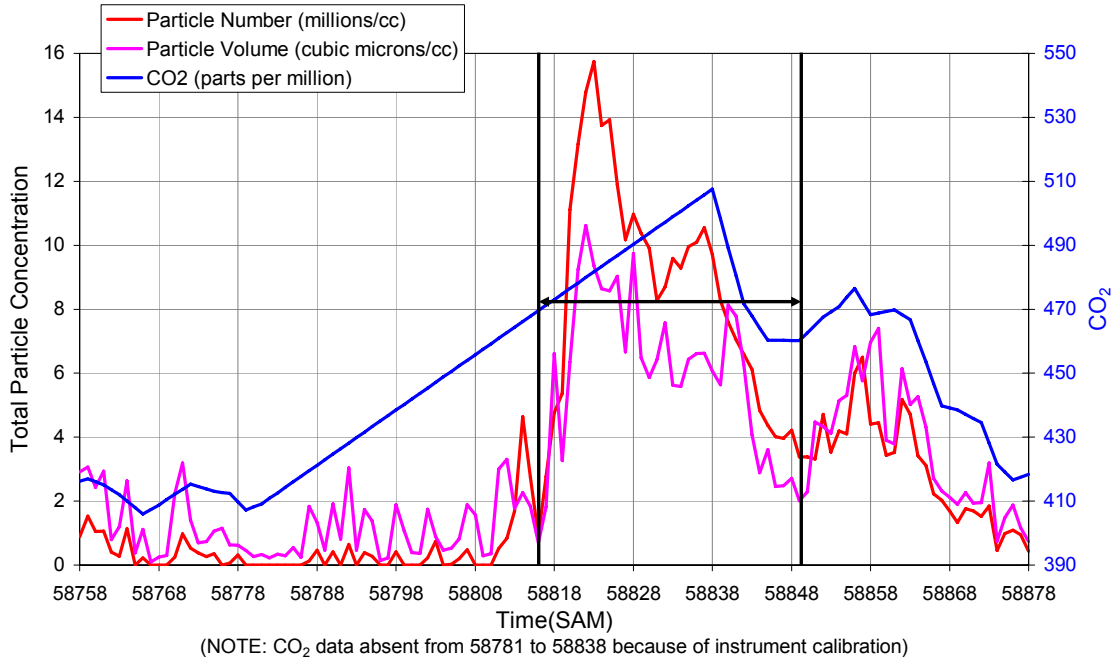
Sample Event 5

Boeing 737-800 Airframe with CFM56-7 Engines
9/29/2004   16:16:34

Figure 48a: Sample Event 5 - Total Particle Concentration (Number and Volume) and CO₂ Concentration as a Function of Time

- This take-off event spans 58624 to 58653 and is both preceded and followed by other take-off events.
- The preceding event from 58566 to 58577 is the take-plume of a regional jet.
- The following event is the A340-400 take-off featured next in the sample events.
- Immediately before this take-off there is an unassigned idle signature from 58595 to 58623 possibly from a taxiing aircraft in line for take-off.
- This take-off event is dominated by the small particle volume mode.

Boeing 737-800 Airframe with CFM56-7 Engines
9/29/2004   16:16:34

Figure 48b: Sample Event 5 – Particle Number Concentration Size Distribution as a Function of Time

Boeing 737-800 Airframe with CFM56-7 Engines
9/29/2004   16:16:34

Figure 48c: Sample Event 5 - Particle Volume Concentration Size Distribution as a Function of Time

Sample Event 6

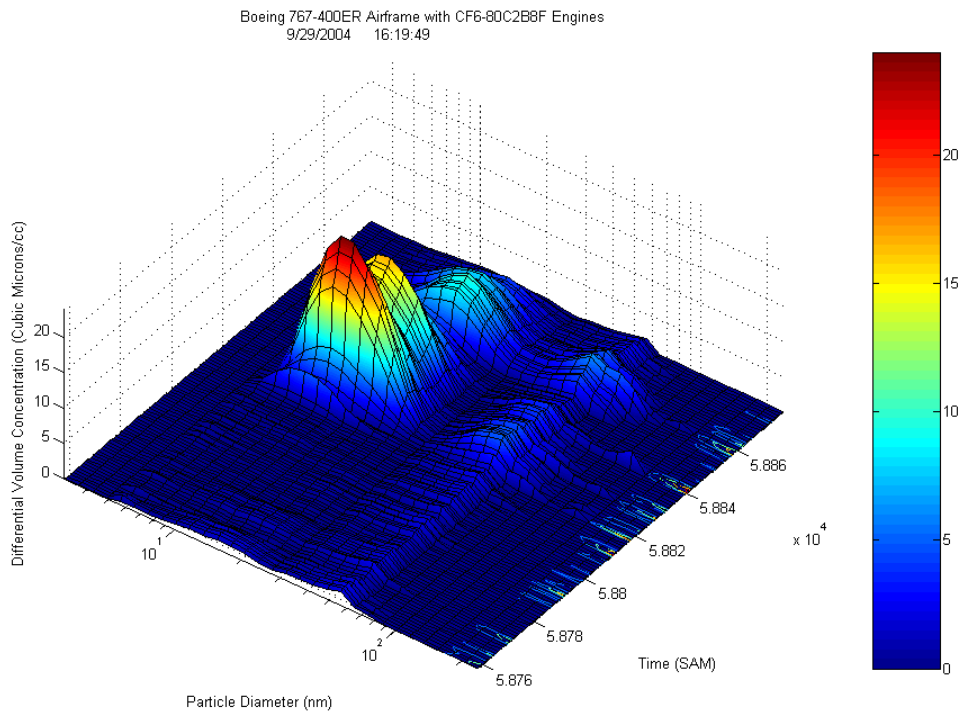A340-400 Airframe with CFM56-5C4 Engines
9/29/2004   16:17:31
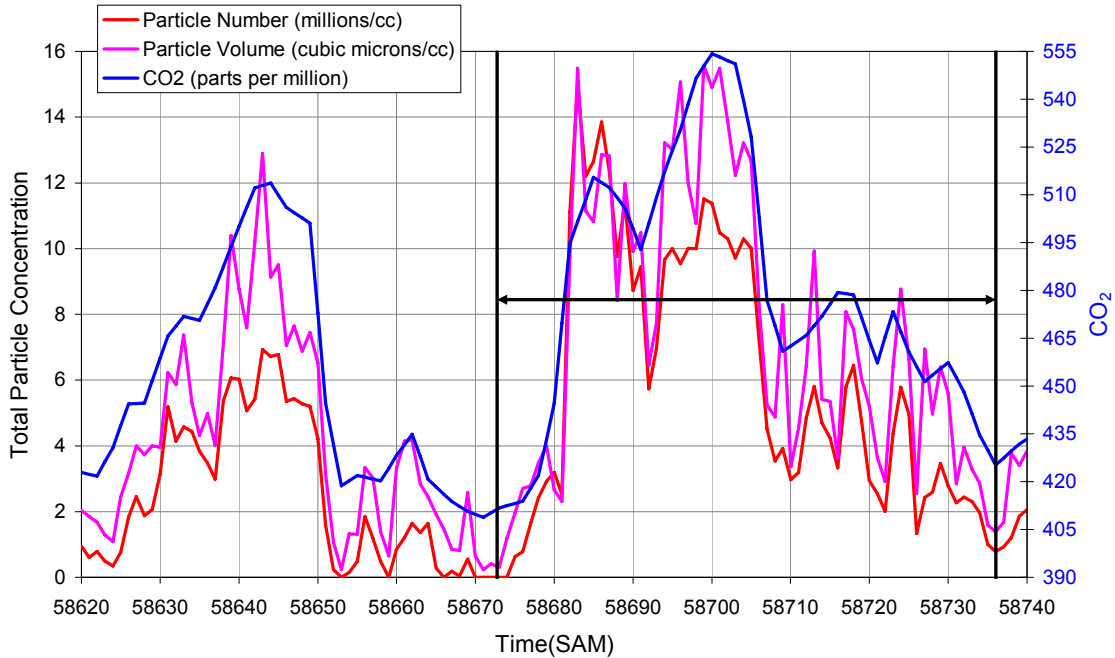
Figure 49a: Sample Event 6 - Total Particle Concentration (Number and Volume) and CO₂ Concentration as a Function of Time

- This take-off event spans 58673 to 58736 and has two peaks possibly because this is a four engine aircraft.
- The preceding event is the 737-800 which is the immediately previous event featured.
- The second peak is weaker in number concentration because it has had about 15 seconds longer to disperse with the ambient air and/or the small particles have agglomerated into larger ones.
- The second peak has a larger average size for the small particle volume mode because the longer travel time has allowed more agglomeration to occur, similarly to the 747 discussed above.

Figure 49b: Sample Event 6 – Particle Number Concentration Size Distribution as a Function of Time

Figure 49c: Sample Event 6 - Particle Volume Concentration Size Distribution as a Function of Time
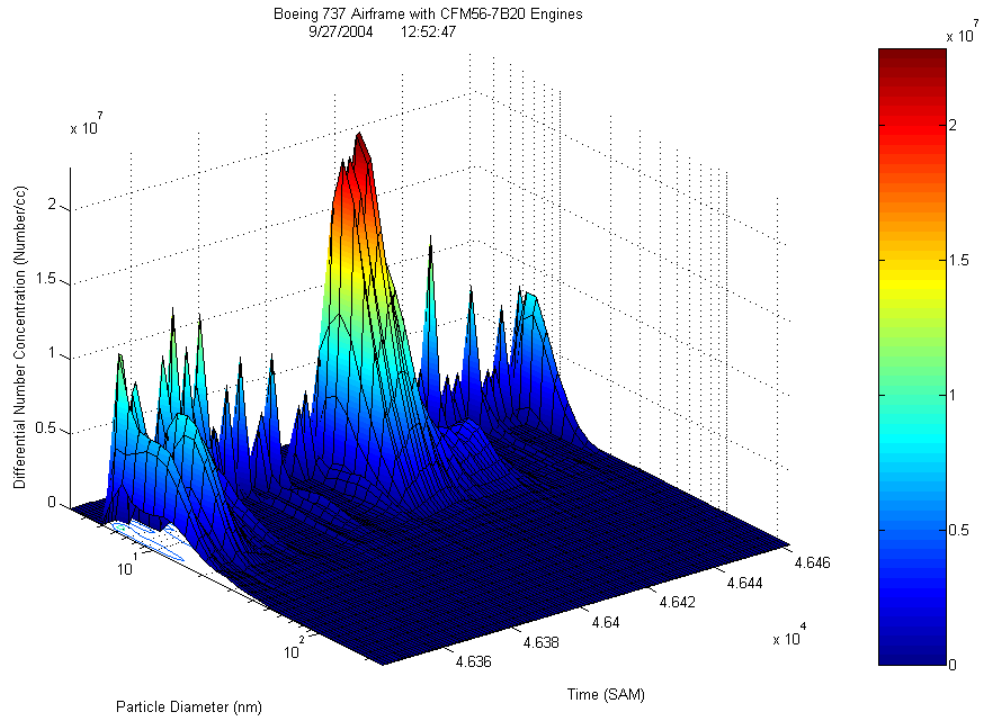
Sample Event 7

MD-88 Airframe with JT8D-217C Engines
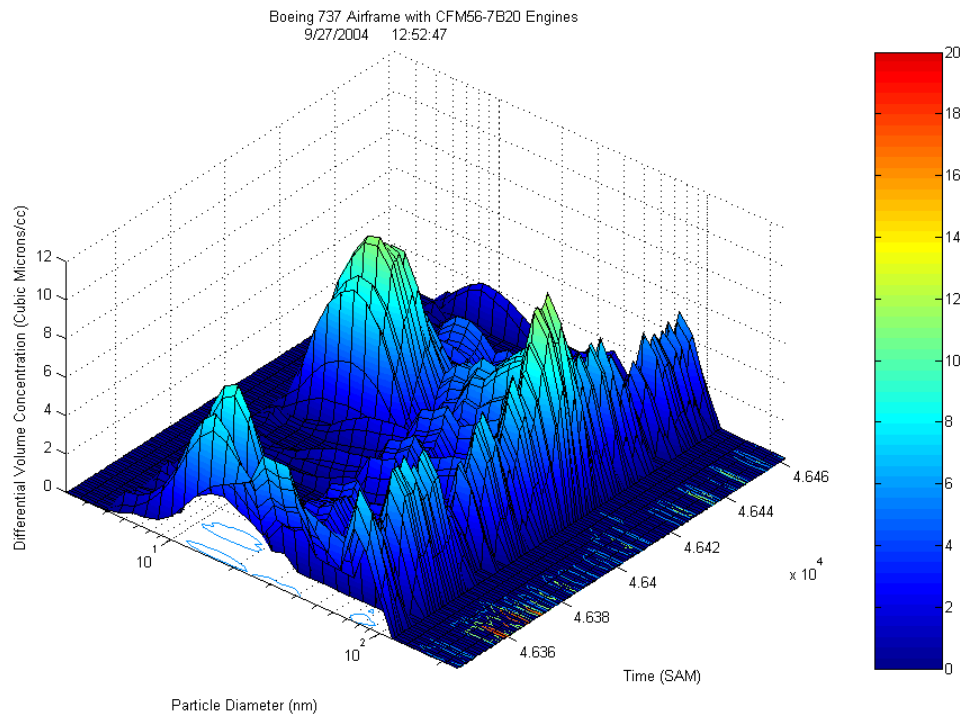### 9/27/2004   15:14:47
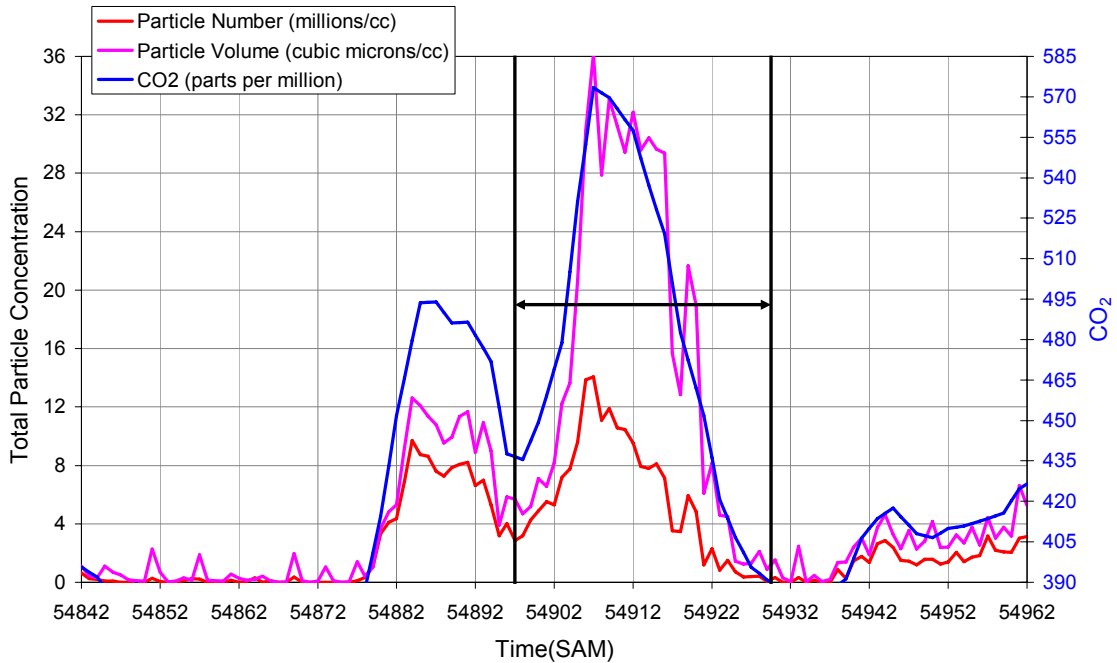
Figure 50a: Sample Event 7 - Total Particle Concentration (Number and Volume) and CO₂ Concentration as a Function of Time

- This take-off event spans 54897 to 54929 and is immediately preceded by the idle signature of the same aircraft from 54878 to 54896.
- While the take-off and idle have about the same particle number concentration, the take-off has a much higher volume concentration.
- The above trend is possibly because of the increase in the magnitude of the large particle volume mode at the higher power of take-off versus the relatively lower power idle.
- The peak size of the large particle volume mode does not increase from low power to higher power which is distinctly different than the "spooling" event (CF6-80A2 engines) analyzed earlier perhaps because of the differing engine type.
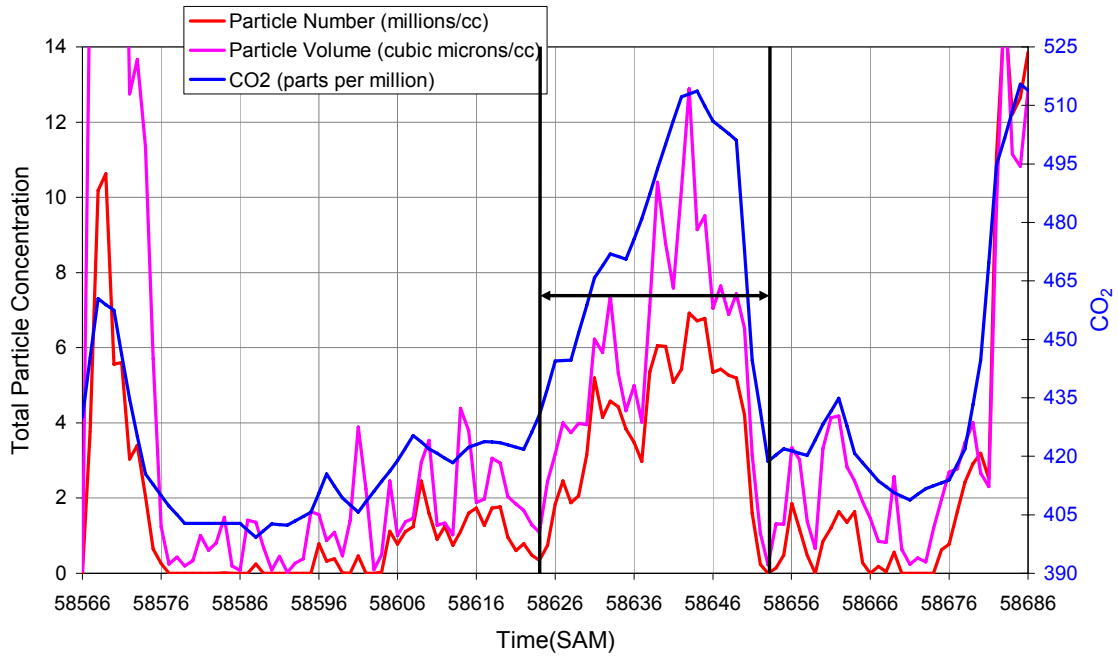
Figure 50b: Sample Event 7 – Particle Number Concentration Size Distribution as a Function of Time

Figure 50c: Sample Event 7 - Particle Volume Concentration Size Distribution as a Function of Time
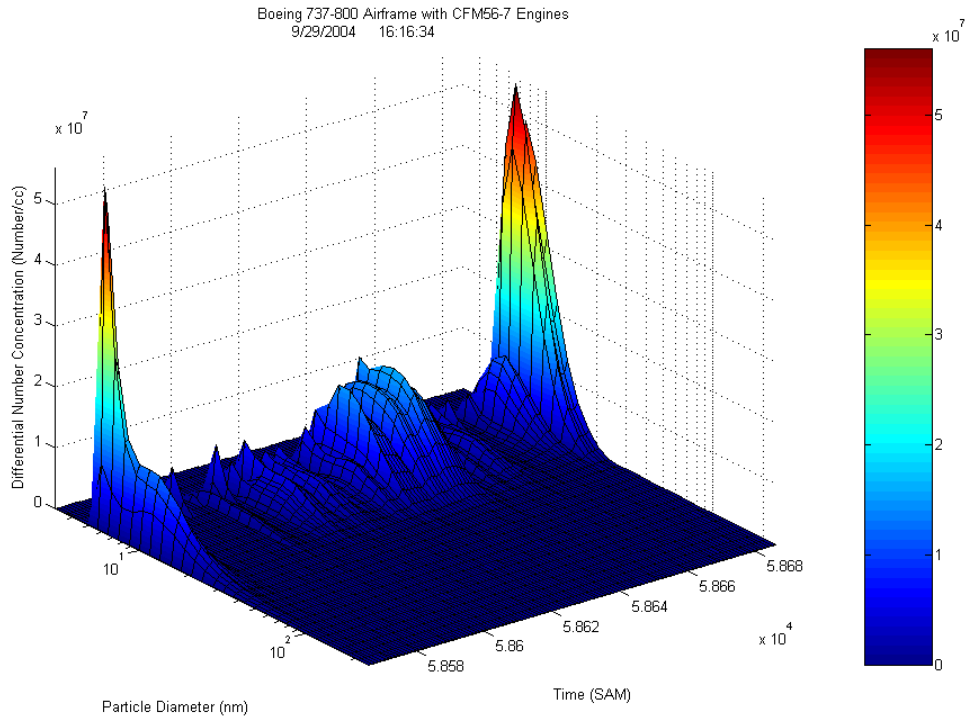
Sample Event 8

MD-88 Airframe with JT8D-219 Engines
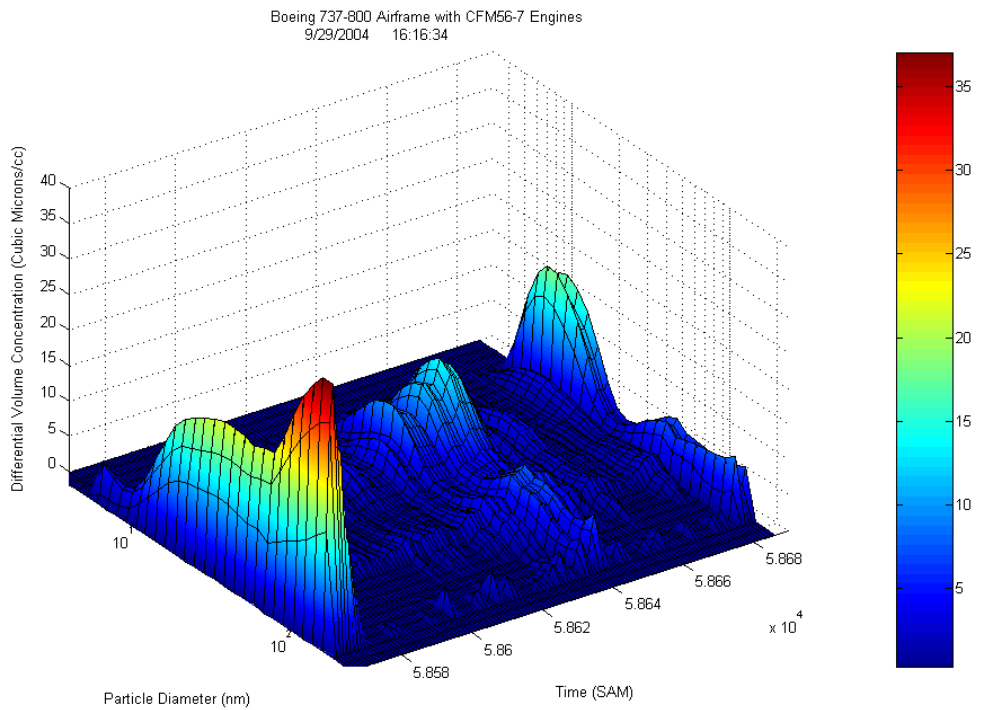9/29/2004   15:07:57
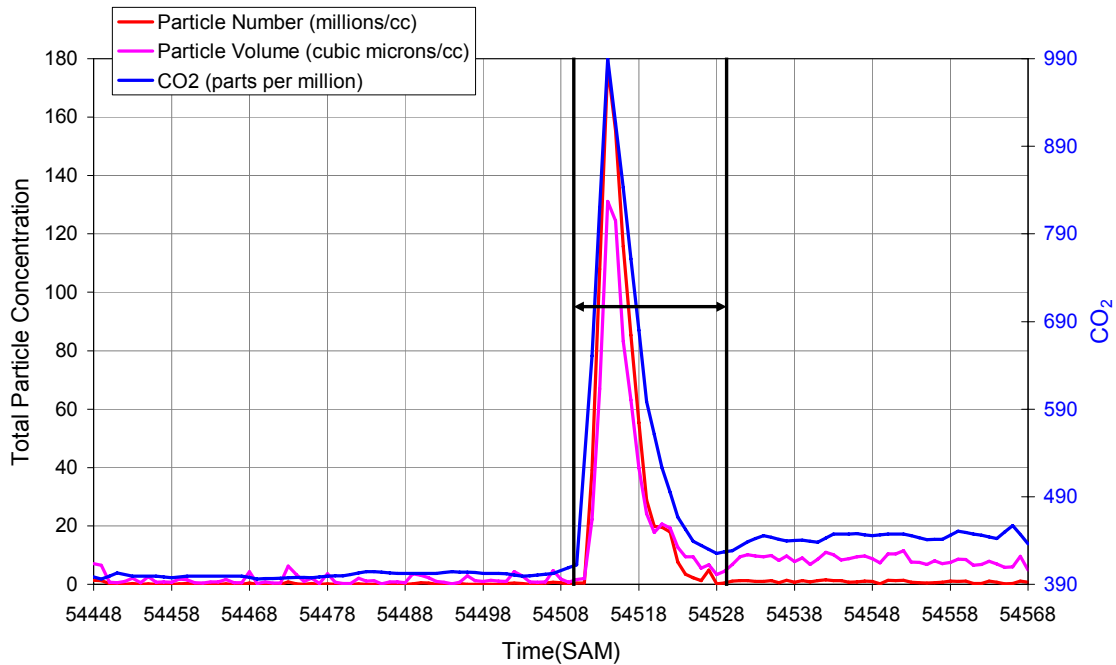
Figure 51a: Sample Event 8 - Total Particle Concentration (Number and Volume) and CO_2 Concentration as a Function of Time

- This take-off event spans 54510 to 54528 and is extremely atypical because of its extremely high particle and carbon dioxide concentrations.
- The order of magnitude increase in concentrations for this event is as yet unexplained, but clearly is indicative of a higher fuel consumption rate.
- The concentration of carbon dioxide produced is well below what can be produced by the stoichiometric reaction of commercial jet fuel with air, meaning this high concentration is not chemically impossible.
- The volume size distribution is sharply bimodal with each mode having about the same peak differential concentration of about 140 cubic microns of particle per cubic centimeter of air.

Figure 51b: Sample Event 8 – Particle Number Concentration Size Distribution as a Function of Time

Figure 51c: Sample Event 8 - Particle Volume Concentration Size Distribution as a Function of Time
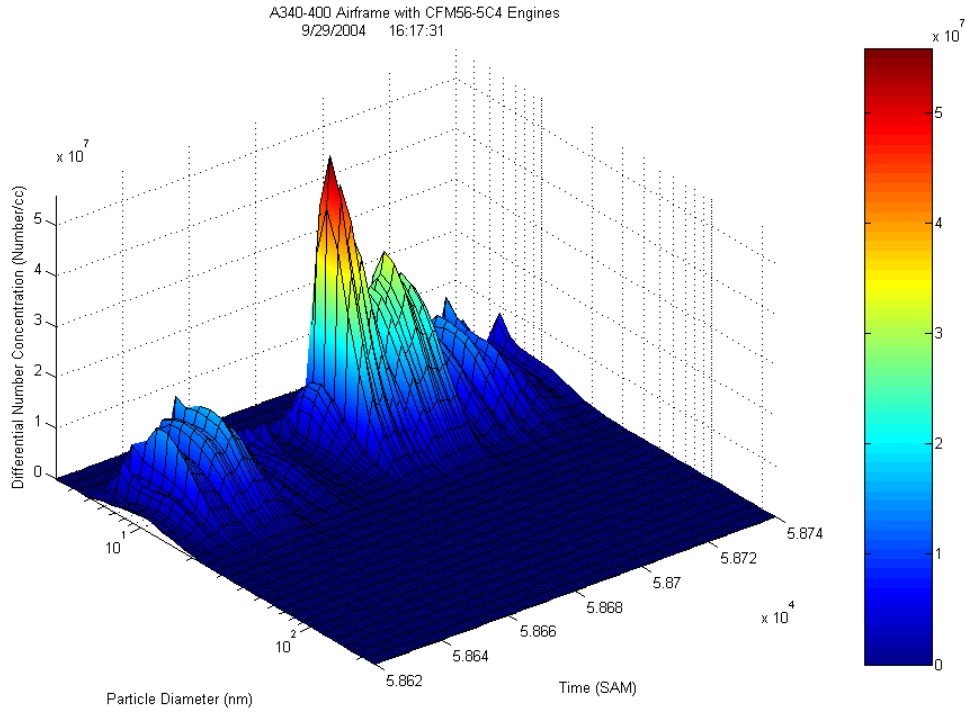
Sample Event 9

MD-88 Airframe with JT8D-219 Engines
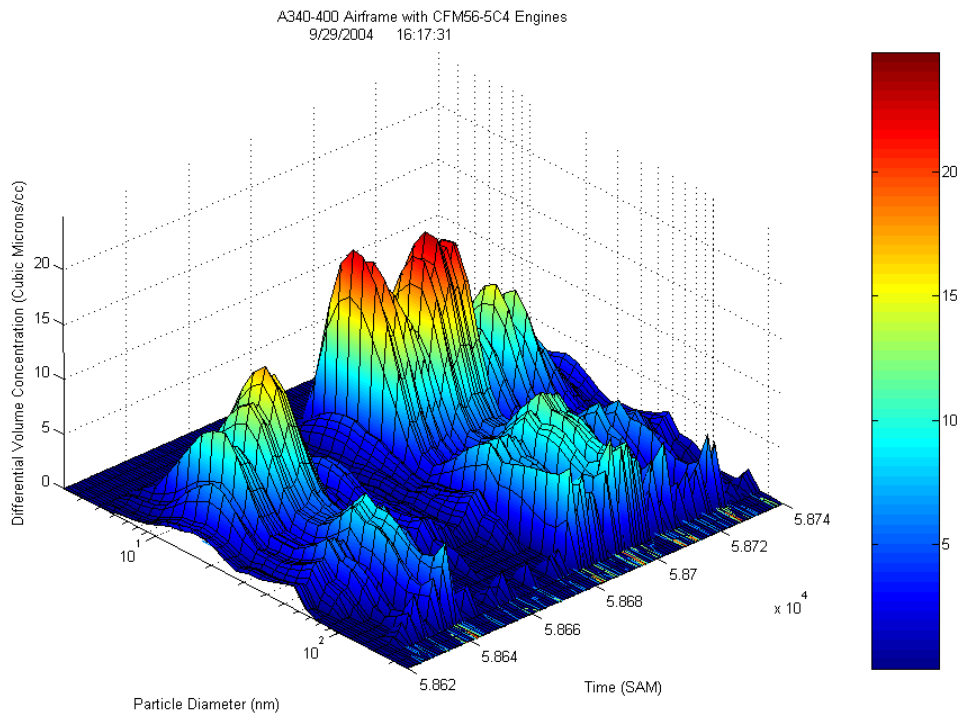9/29/2004   16:40:41
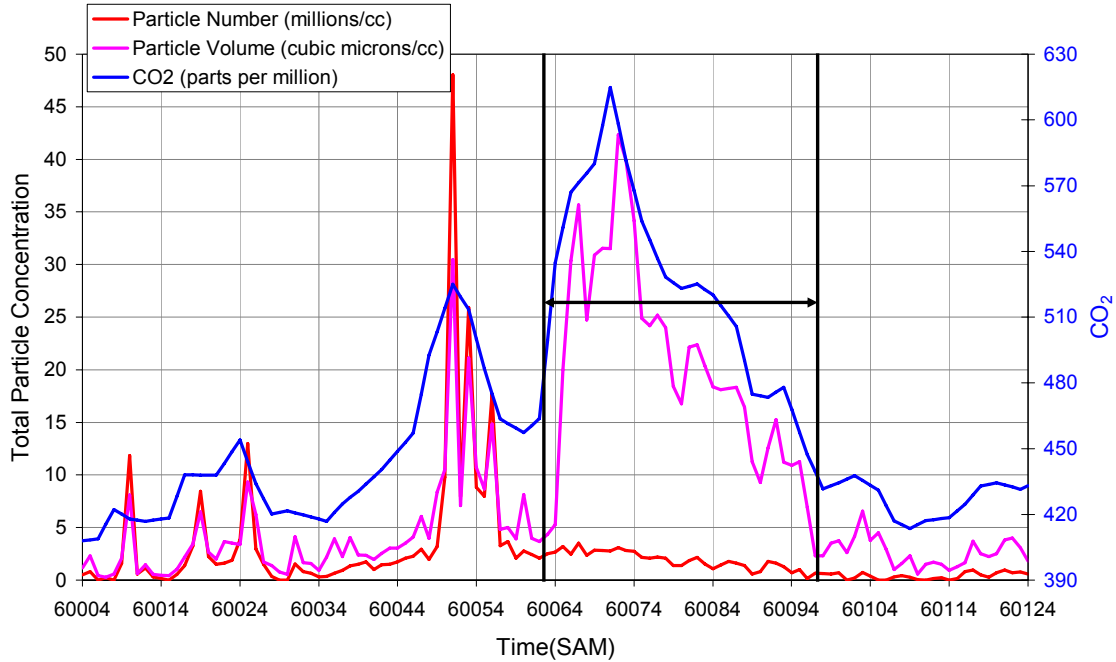
Figure 52a: Sample Event 9 - Total Particle Concentration (Number and Volume) and CO_2 Concentration as a Function of Time

- This take-off event spans 60063 to 60097 and is immediately preceded by an unassigned idle signature from 60044 to 60060.
- This take-off event is not identifiable by number concentration alone as it exhibits almost no increase in the number of particles; this phenomenon appears typical of most JT8D take-off plumes.
- This take-off event is clearly identifiable by volume concentration as the volume of large particles produced increases greatly from background conditions.
- This take-off event contains practically no small particle volume mode.
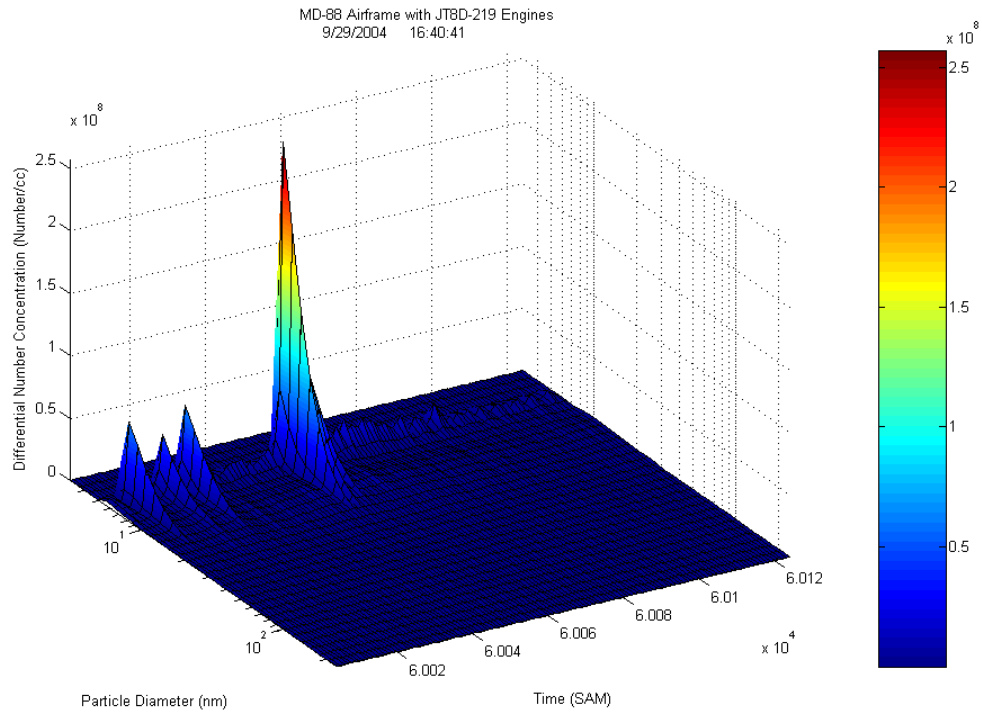
Figure 52b: Sample Event 9 – Particle Number Concentration Size Distribution as a Function of Time
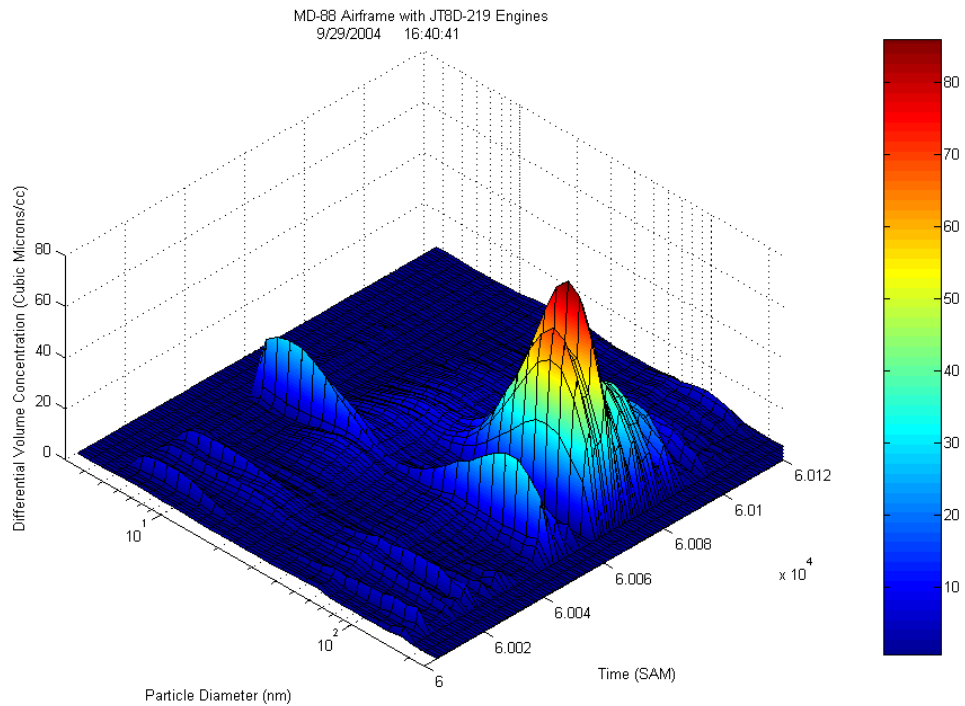
Figure 52c: Sample Event 9 - Particle Volume Concentration Size Distribution as a Function of Time

Sample Event 10

Boeing 757-200 Airframe with PW 2037 Engines
9/27/2004   12:32:26
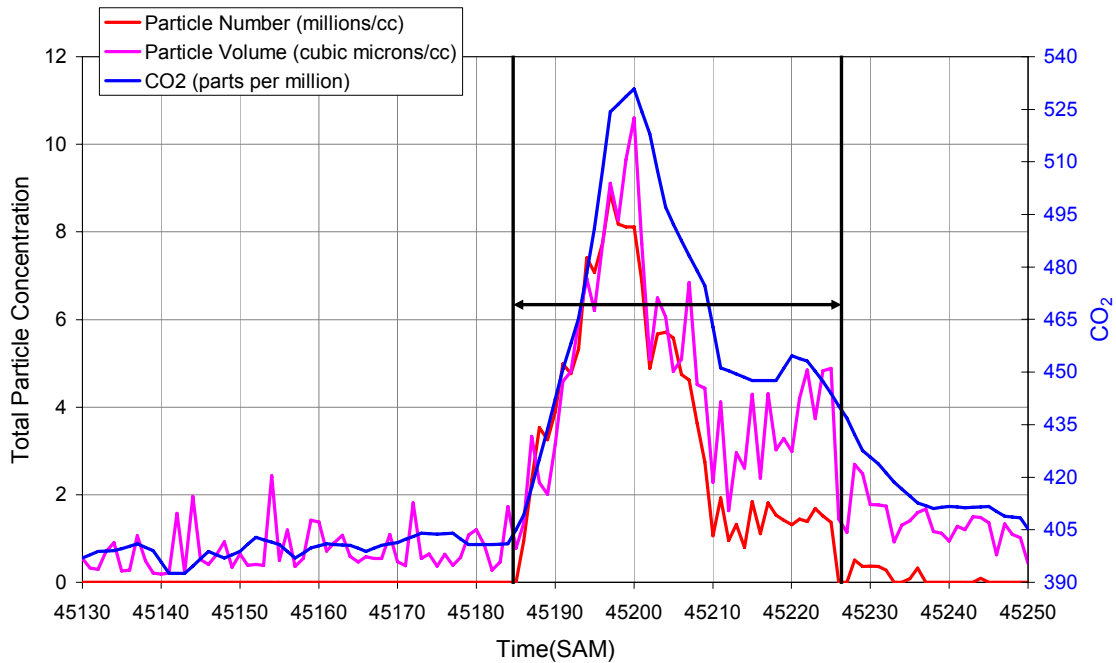
Figure 53a: Sample Event 10 - Total Particle Concentration (Number and Volume) and CO₂ Concentration as a Function of Time

- This take-off event spans 45785 to 45226 and is fairly typical in structure.
- This take-off event is bimodal in volume concentrations with a small particle mode that peaks at 10 nm, and a large particle mode that peaks at 75 nm.
- The peak values of the small and large particle volume modes are approximately the same.

101
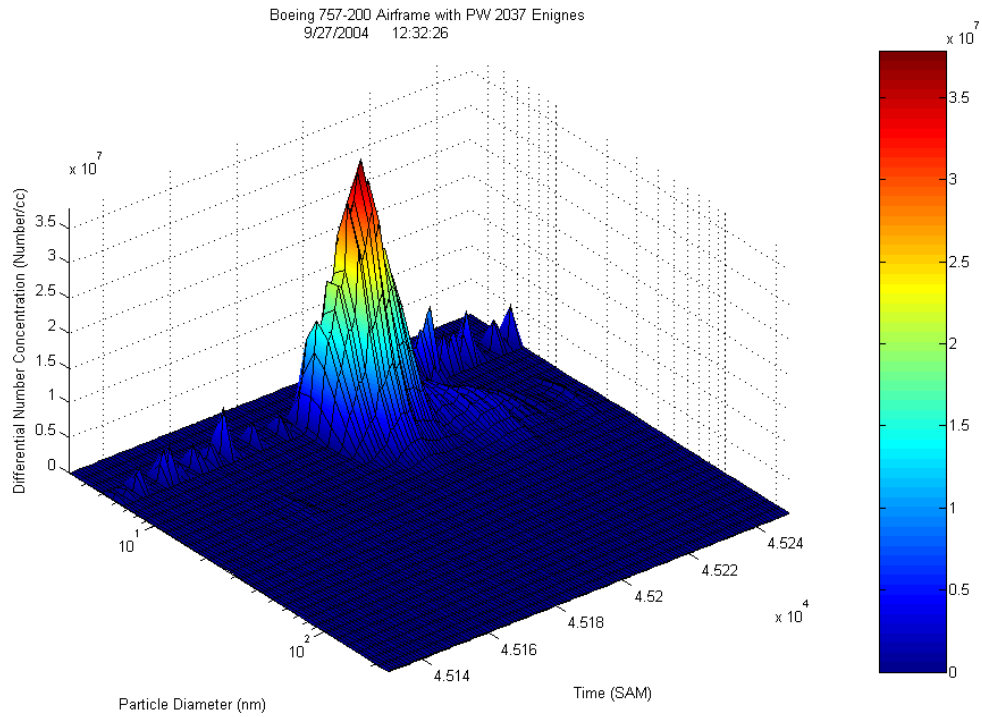
Figure 53b: Sample Event 10 – Particle Number Concentration Size Distribution as a Function of Time
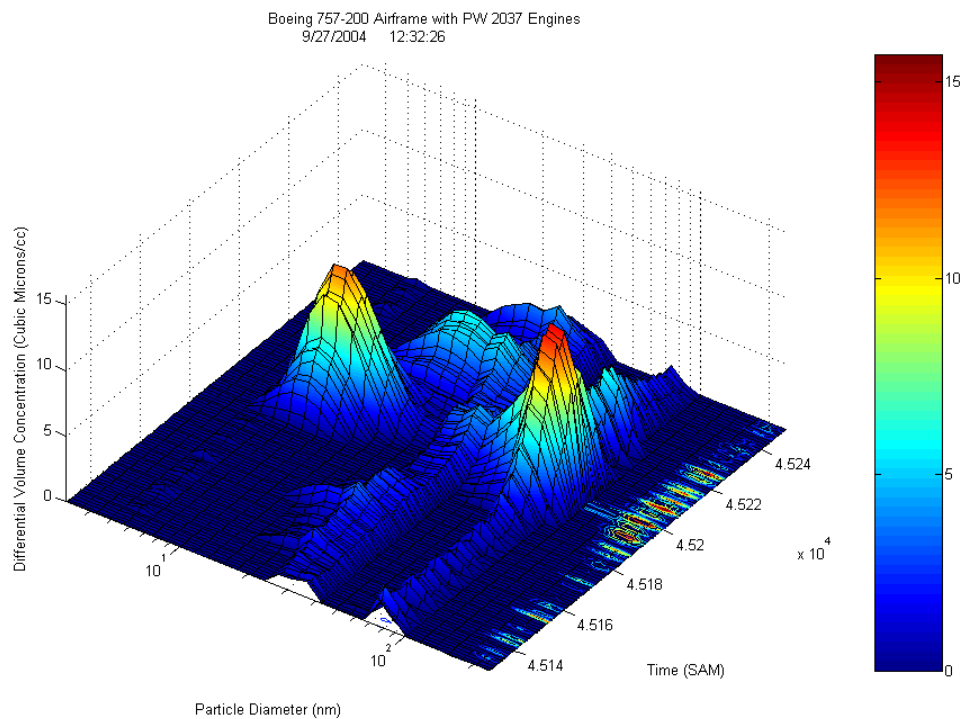
Figure 53c: Sample Event 10 - Particle Volume Concentration Size Distribution as a Function of Time
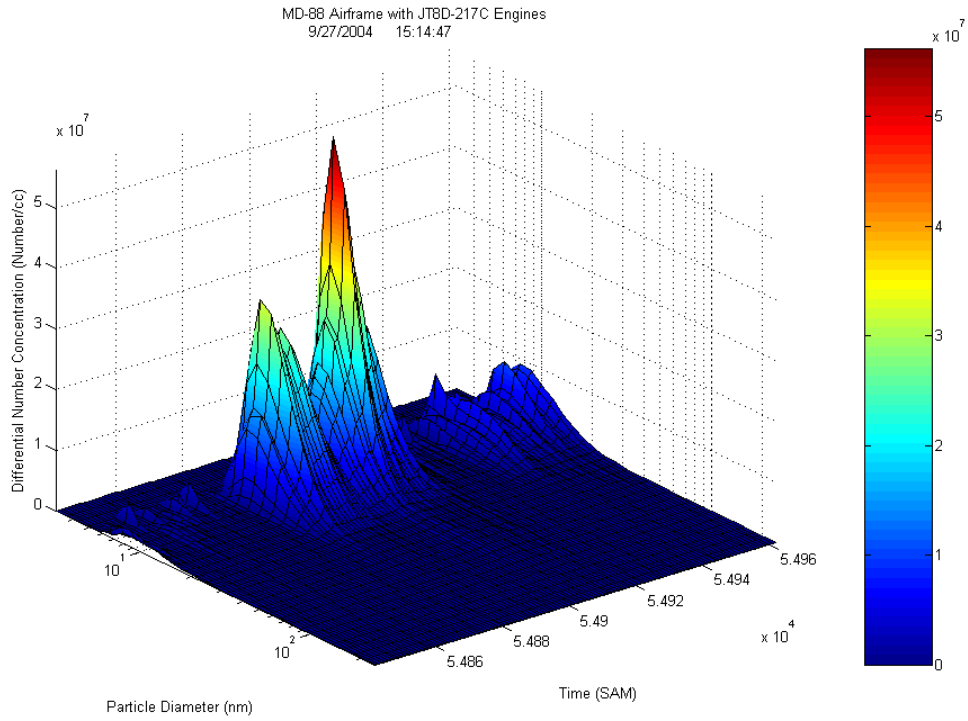
Sample Even 11

Boeing 717 Airframe with BR715A1-30 Engines
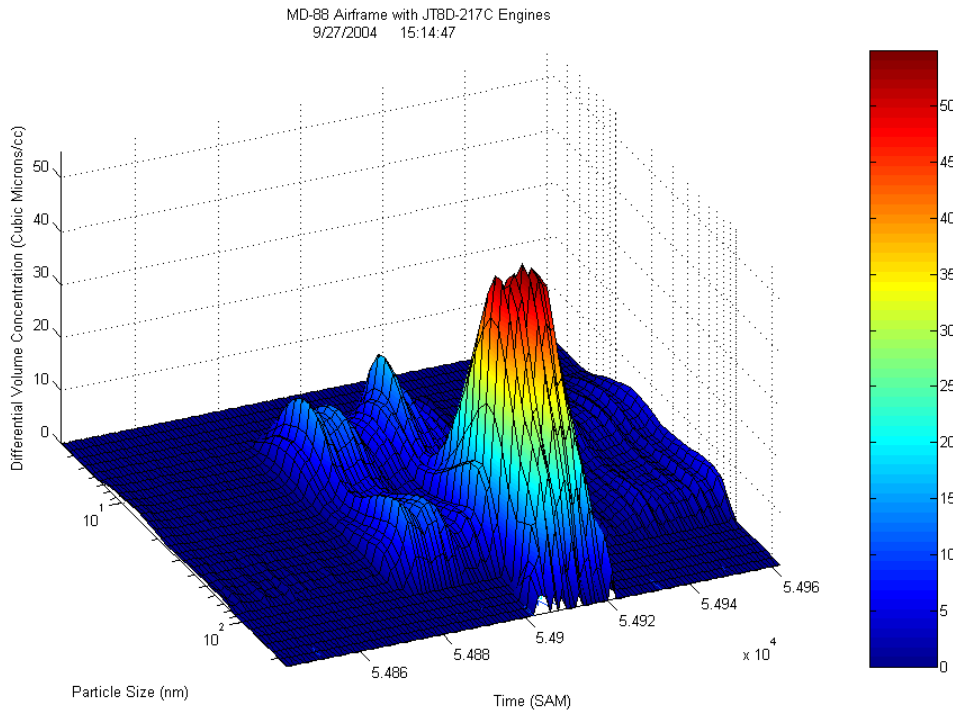### 9/29/2004   16:22:45
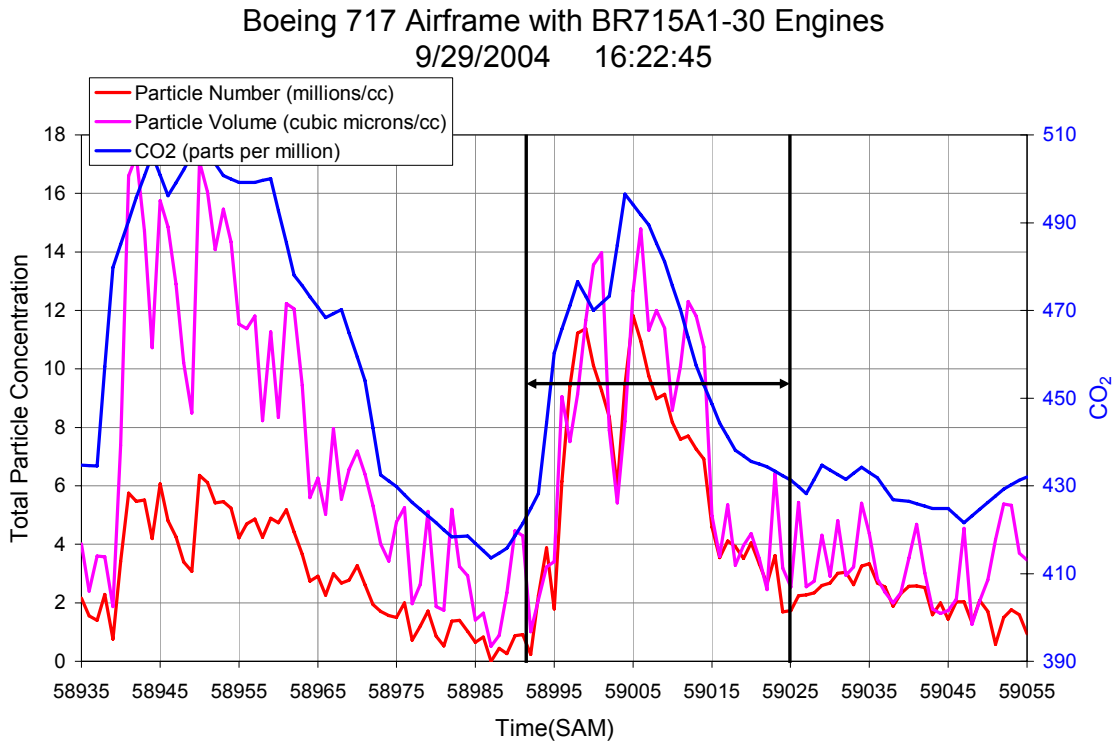
Figure 54a: Sample Event 11 - Total Particle Concentration (Number and Volume) and CO_2 Concentration as a Function of Time

- This take-off event spans 58991 to 59025 and is preceded by another take off event that corresponds to a 737 with JT8D-15A engines from 58937 to 58990.
- This take-off event is dominated by its small particle volume mode, whereas the 737 preceding it on this plot is dominated by the large particle mode consistent with JT8D engines.
- The number concentration of particles produced by this 717 is larger than that for the 737 preceding it, although the 737 produces a larger particulate volume concentration.
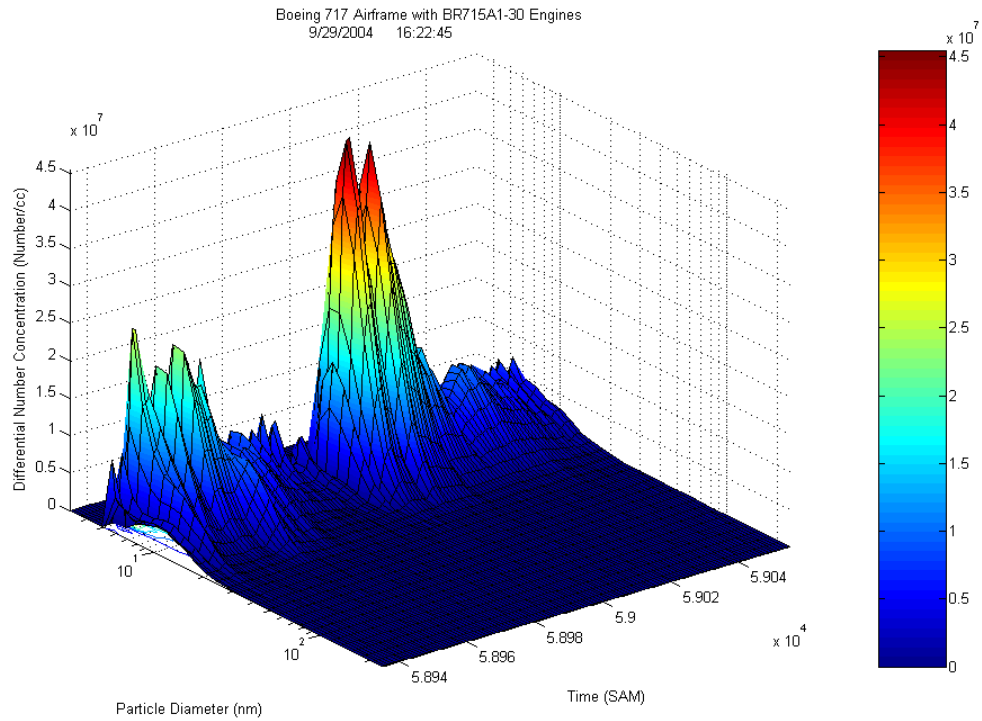
Figure 54b: Sample Event 11 – Particle Number Concentration Size Distribution as a Function of Time
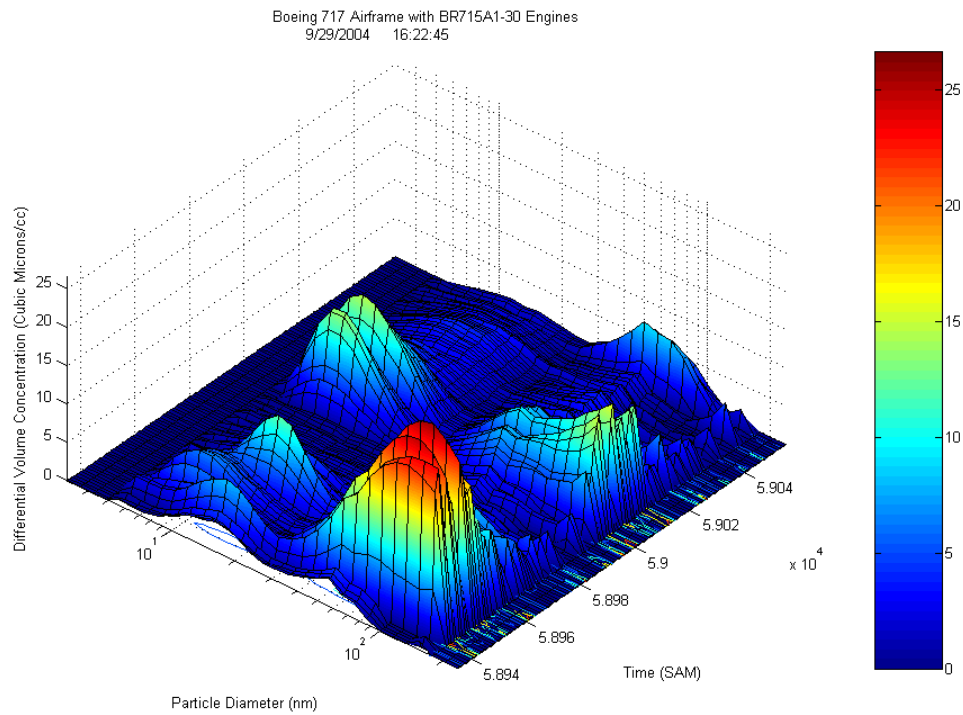
Figure 54c: Sample Event 11 - Particle Volume Concentration Size Distribution as a Function of Time

Sample Event 12

CRJ Airframe with CF34-3B1 Engines
9/29/2004   17:13:28
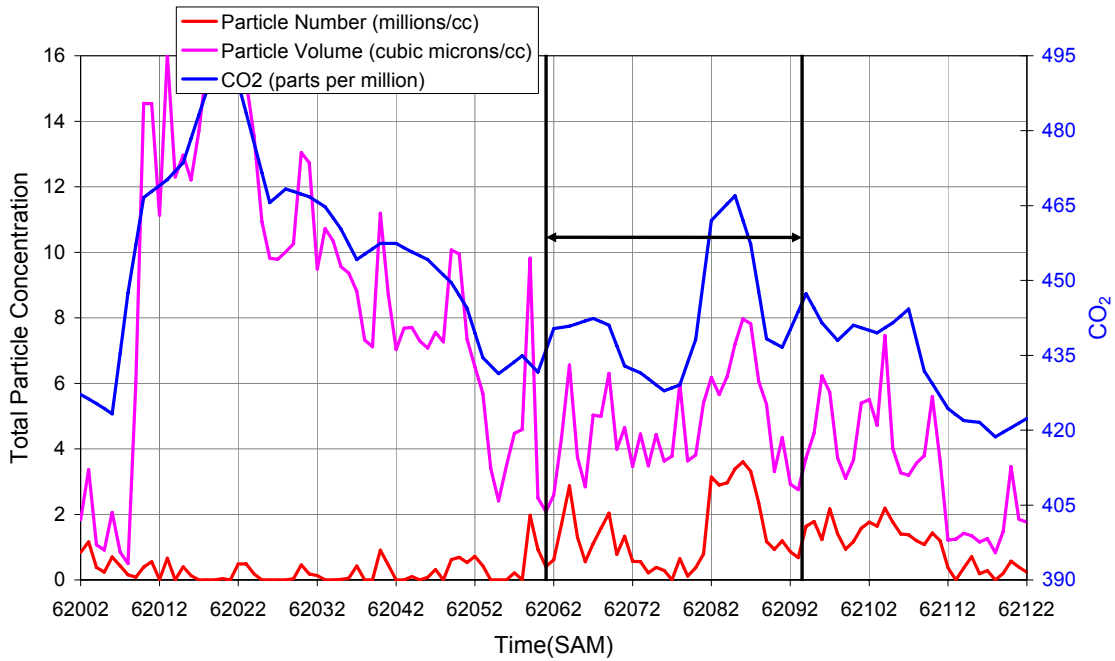
Figure 55a: Sample Event 12 - Total Particle Concentration (Number and Volume) and CO_2 Concentration as a Function of Time

- This take-off event spans 62061 to 62093 and is practically dwarfed by surrounding aircraft activity.
- This take-off event is preceded by the take off of an MD-88 with JT8D-219 engines.
- This take-off event would be unidentifiable by volume concentration alone.
- This take-off event is dominated by a large particle volume mode, while the small particle volume mode is practically non-existent.
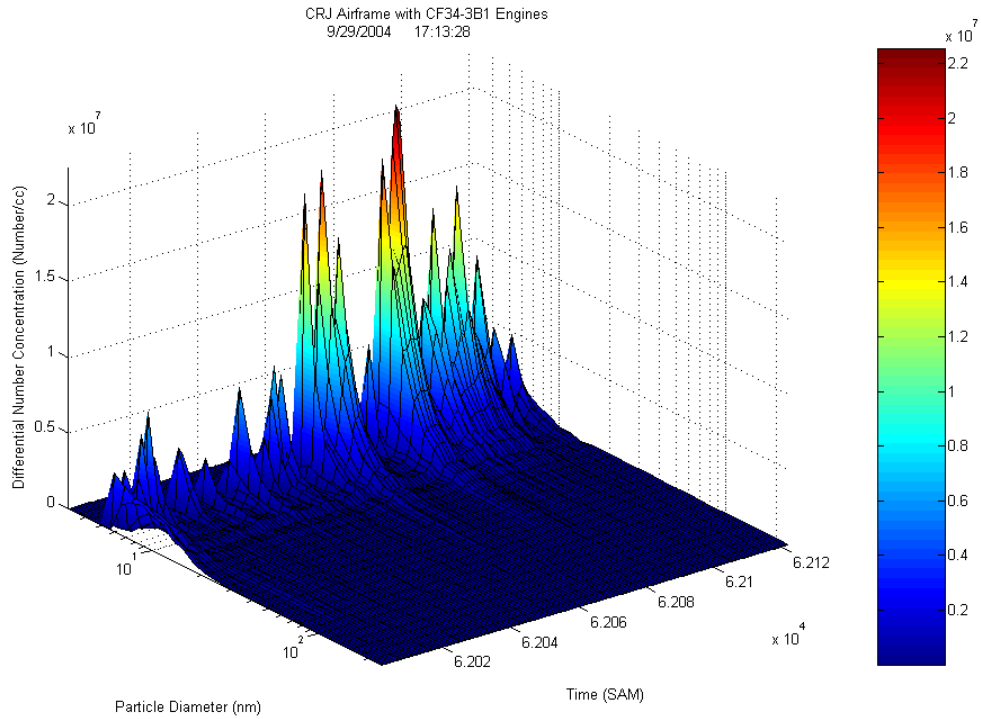
Figure 55b: Sample Event 12 – Particle Number Concentration Size Distribution as a Function of Time
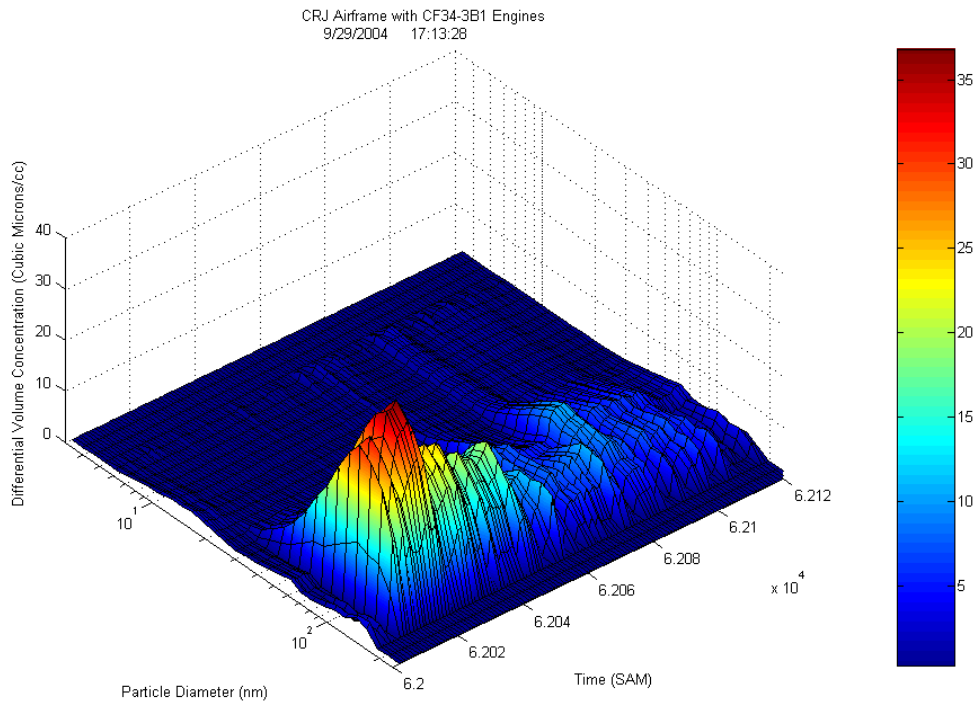
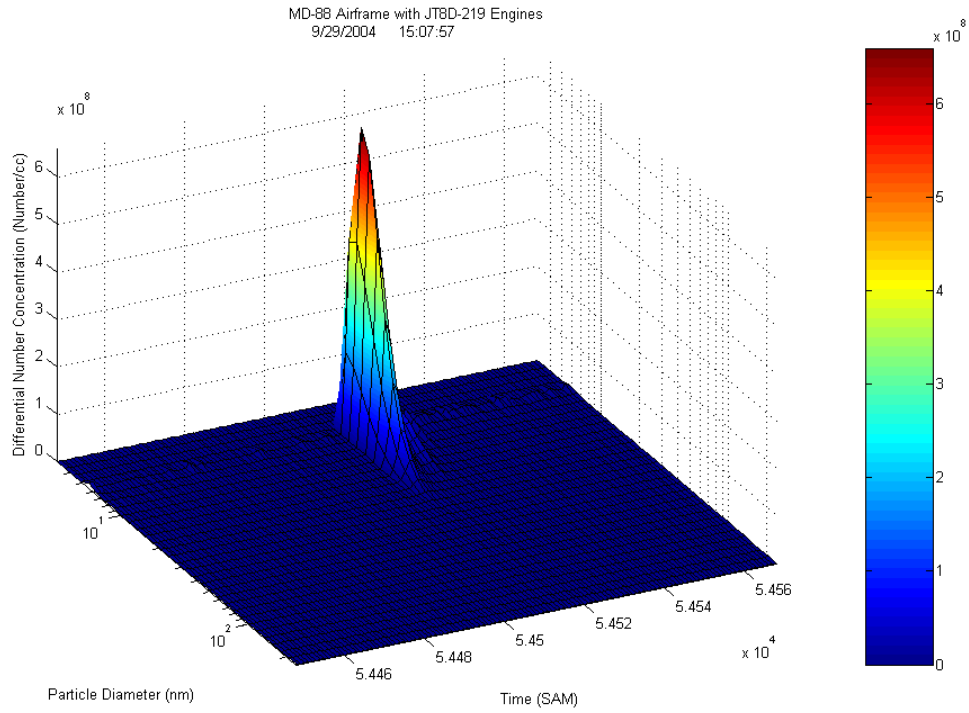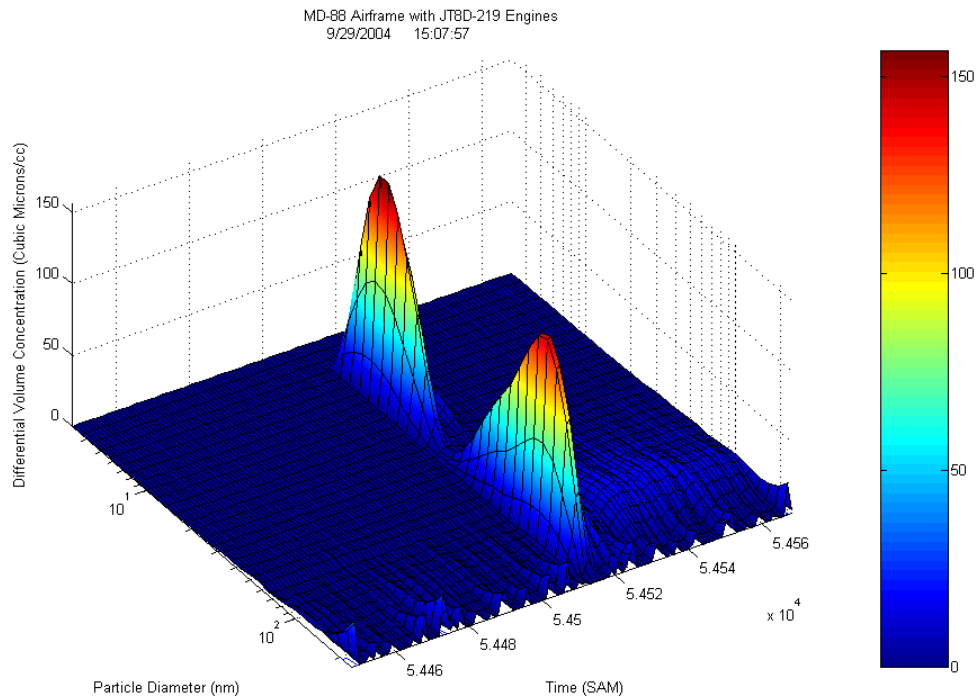**Figure 55c: Sample Event 12 - Particle Volume Concentration Size Distribution as a Function of Time**

106

3.2.3.3 Engine-specific Emission Index Averages from Advected Plume Measurements

This study yielded 500 unique aircraft related events, of which 289 were clearly identified as takeoff plumes, from the six most common engine types, then operating at Atlanta Hartsfield. It is informative to examine averages of PM number- and mass-based emission indices for selected engine types and for each of the three sampling days to capture impacts due to changes in ambient conditions and background PM.

Fig. 56 represents the overall daily averages of number-based emission indices for the six engine types – BR715, CF34, CF6-80, CFM56, JT8D, and PW2037. These are weighted averages based on the uncertainties associated with each plume event. The error bar on each vertical bar represents the statistical uncertainty in the average due to the individual plume uncertainties, discussed in section 3.2.2. The number on each vertical bar gives the number of takeoff events for a given engine on a given day. A composite for all three days is also included in the figure. Its error bar represents the standard deviation (1σ) in the three day average.
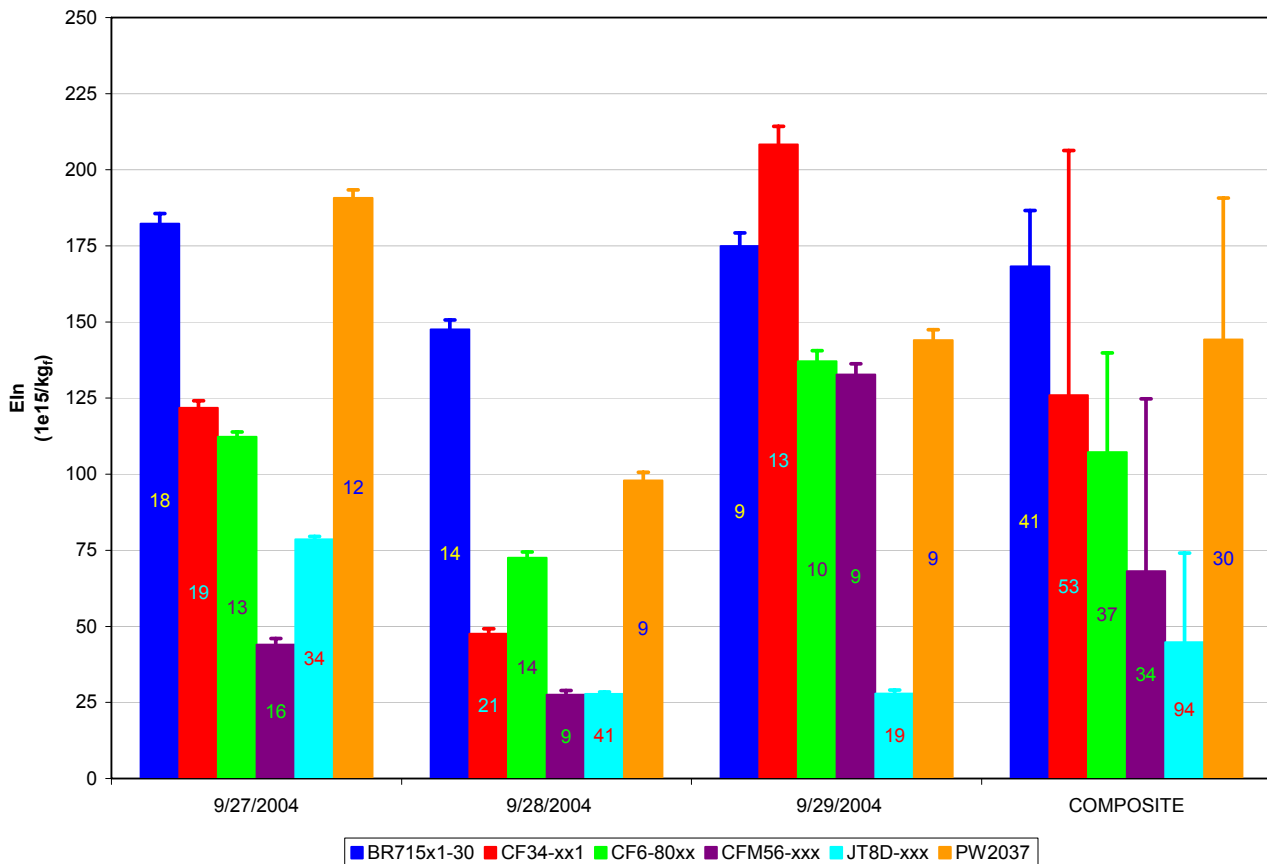
Figure 56: Overall Average EIn for Six Aircraft Engine Families

There is a significant day-to-day variation in number-based emission index. The day-to-day change is bigger than the uncertainty in the average for a given day. The behaviors of engines of a given class are remarkably similar on a given day. It should be noted that the error bars on the composite are significantly larger than on the daily averages. This variation can be attributed to changes in ambient conditions.

The sign of the EIn change from day-to-day (with changing ambient conditions) was the same for all engines. The emissions from the engines either collectively, all increased or all decreased together with changes in ambient conditions. The ambient conditions which caused the emission changes have not been identified, but temperature, relative humidity, and pressure significantly changed from one day to the next. Further research is warranted for correlating changing atmospheric conditions to changes observed in the emissions.

The emissions from the JT8D engines, oldest technology engine in this comparison group, stands out from the other engines. While on average, the JT8D engines have a relatively lower number-based emission index, the average mass-based emission index is the highest, when compared to the other engines (see Fig. 57).
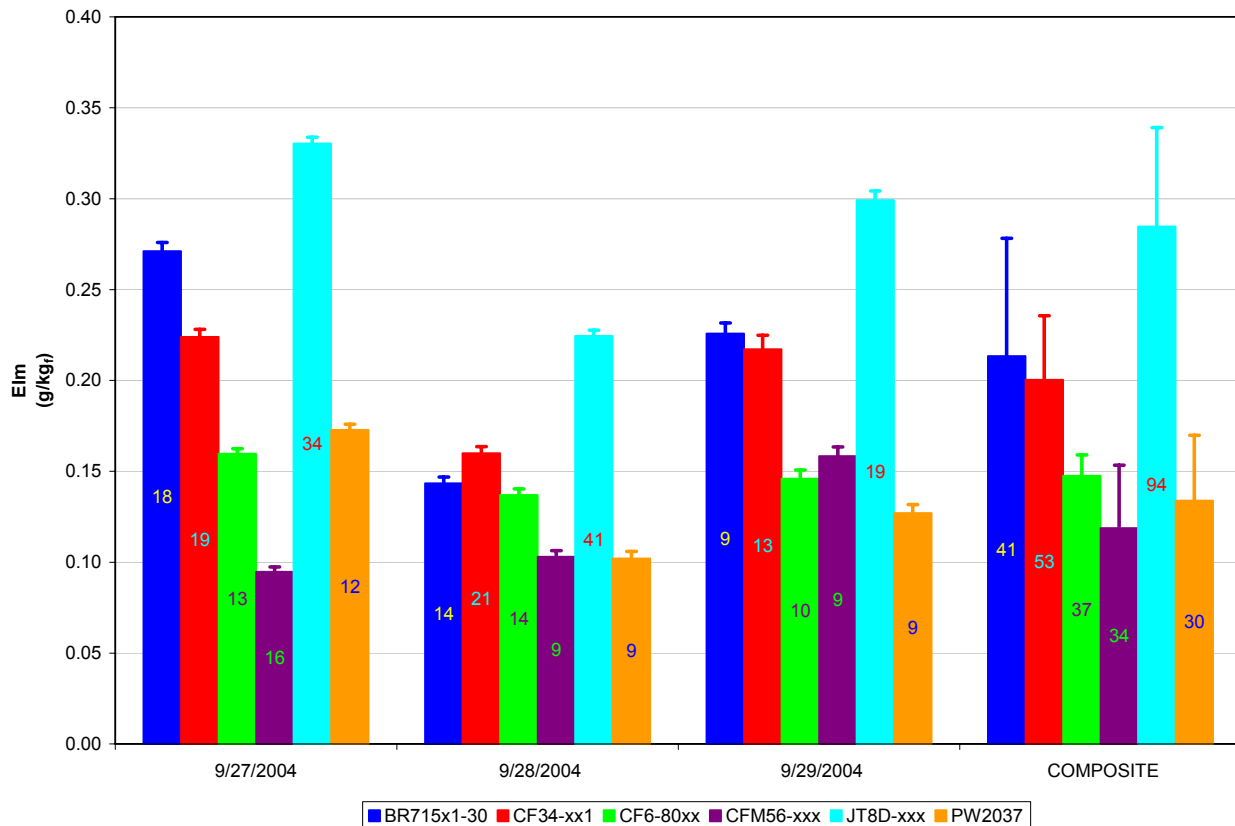
Figure 57: Overall Average EIm for Six Aircraft Engine Families

3.2.4 LIDAR Results

Airfield testing was accomplished using LIDAR, in the same manner for the UNA-UNA study as at LAX (Wayson et al., 2004). Except for a few engineering improvements, the same system (OPAL) was used (see Fig. 2). Shown mounted on top of the trailer, the ultraviolet beam is emitted and the backscatter is measured through precise mirror alignment. The precision in elevation pointing was improved for UNA-UNA, allowing measurements closer to the ground.

LIDAR system operates at an ultraviolet wavelength of 0.355 μm and measures the backscatter from the aerosols emitted by the aircraft engines. It should be noted that these aerosol components are very small, typically less than 100 nanometers with reported average diameter of about 30 nanometers.

The LIDAR System had to be placed so that the plume cross sectional results could provide meaningful information. Fig. 58 shows an idealized view of how the system was located, and it lists key measurement parameters for the LIDAR system.
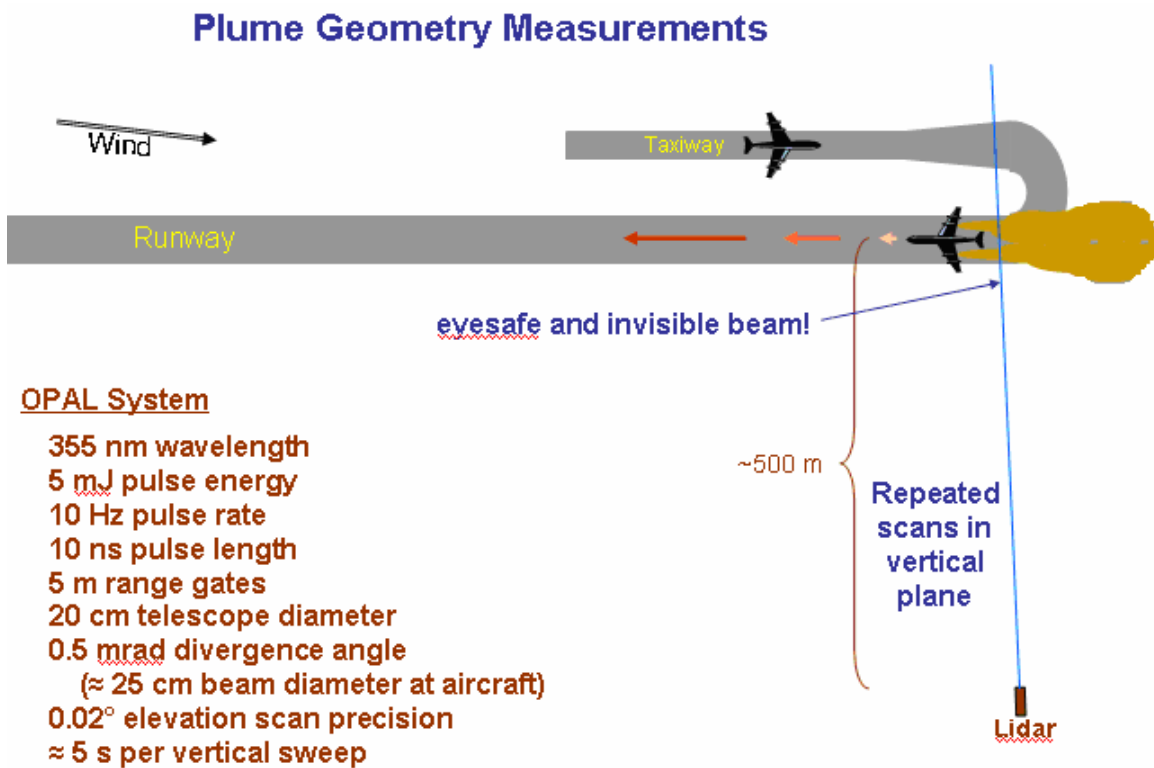
Figure 58: Idealized View of LIDAR during Airfield Sampling and Key LIDAR Parameters

The aircraft plumes were measured during initial take-off roll, as at LAX. Testing was done on multiple days and at two different airport positions on various days. The position of the LIDAR system was dependent upon the wind direction during measurements. Testing occurred on two different runways (two LIDAR positions) due to a change in wind direction during the test days.

Measurements on 26 September 2004 were made at one runway (Fig. 59). The LIDAR was approximately 570 m from the center of the runway. The angle between the perpendicular to the centerline and the LIDAR beam was 27°. The beam crossed the center of the runway ≈ 30 m from the end. The beam was typically just in front of the tail of the aircraft when they completed the turn onto the runway. Most of the time the LIDAR scan plane was fairly close to the hindmost part of the tail when the aircraft commenced takeoff acceleration.

The active runway was then changed because of a shift in winds, so the LIDAR was moved before continuing measurements at a different runway on 29-30 September. The LIDAR was approximately 670 m away, the angle was 23°, and the beam crossed the center of the runway ≈ 80 m from the end. The beam was in front of the aircraft after they completed the turn onto the runway. For this setup, the aircraft had almost always commenced takeoff acceleration by the time the tail passed the LIDAR 's scan plane.
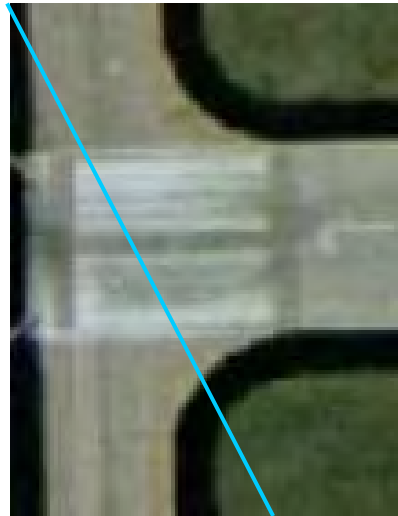
Figure 59: Beam geometry for measurements on 26 September 2004. The blue line shows the approximate position in plan view of the LIDAR's beam. Takeoffs were toward the right. Runway width is 46 m (150 ft).

The LIDAR measured exhaust plumes behind 458 aircraft. A number of these events were eliminated during processing and quality assurance because of signal too weak to detect a plume, merging of one plume with that from the previous aircraft, and other reasons. A total of 342 aircraft takeoff events remained in the final data set. The total number of sweeps in the final data set was 1794.

3.2.4.1 Data reduction

The data collection resulted in raw data sweeps that required extensive quality control by NOAA prior to final formatting and analysis. Fig. 60 shows a typical sweep containing raw data. Further processing by NOAA was required to allow the information to be viewed in a more meaningful fashion. This included redefining the graphical views and further tabulation of the data. Fig. 61 shows a typical sweep after this additional processing.
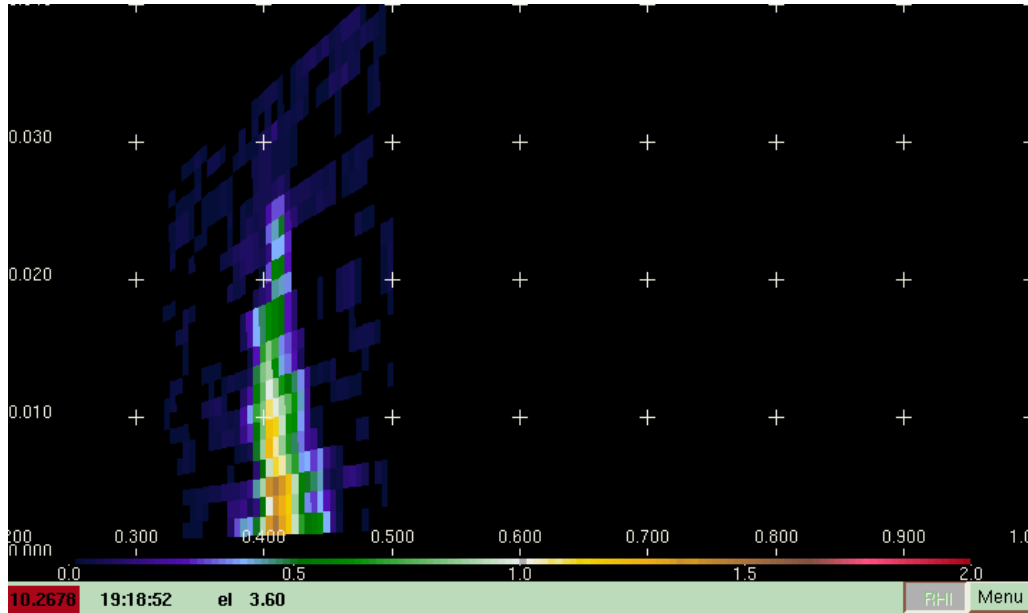
Figure 60: Example Output from the OPAL System

Only after the quality control process was complete could computer graphics be generated to characterize the plume. It was possible to locate the plume center (Z_{center}), the plume width and the plume height. By following the plume center from multiple sweeps for an aircraft takeoff, plume rise could also be determined. The time between each sweep was approximately 5 seconds. The manual analysis was based on pattern recognition of the plume from the key parameters shown in Fig. 61. The manual processing was conducted on one day's worth of Delta-Atlanta Hartsfield data using the manual human pattern recognition process detailed in the LAX report (Wayson et al., 2004).
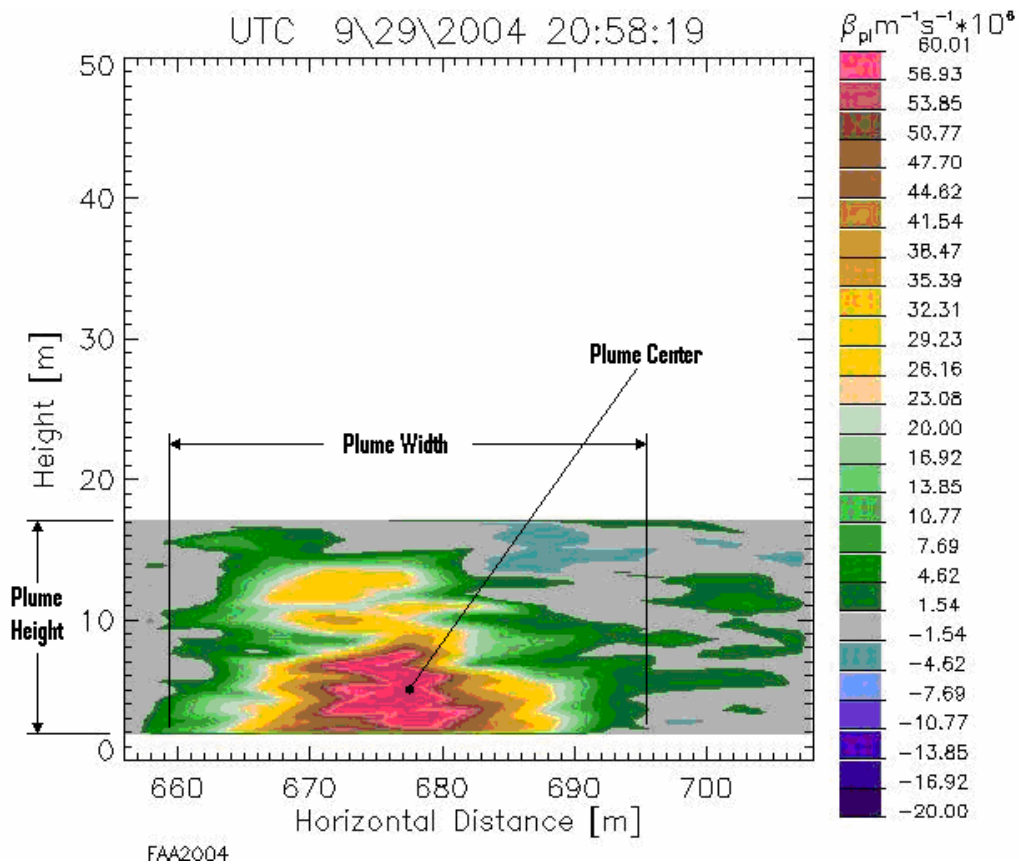
Figure 61: Typical Sweep after Processing

It was thought desirable to automate the data processing so that future sampling could be accomplished much more rapidly, and data review could occur in the field. This would allow reporting time to be greatly reduced for future measurement campaigns. As such, NOAA processed the data in multiple ways to determine key variables that could be used in lieu of the manual pattern recognition method. The variables that were evaluated are listed in Appendix C. It can be seen that many parameters had to be calculated, multiple approaches applied, and results checked.

3.2.4.2 Data analysis

For each aircraft event, the sweep that represented the second highest value for the center of the plume was selected and the value was taken to represent the plume rise in a conservative fashion. This also resulted in a conservative approach used to determine the standard deviation of the plume in the horizontal (σ_y) and in the vertical (σ_z) since the same sweep selected for the plume rise was used. This is the location that is assumed to start dispersing downwind and the key input needed using the Gaussian dispersion modeling approach. Again, this mirrors the methodology used at LAX.

Fig. 61 represents a well-defined plume. The outer dimensions of the plume were derived, as in the LAX study, using the concentration gradient displayed in each scan. The scale on the side of Fig. 61 should be noted. To make sure that the plume was represented in an accurate fashion, and not other concentrations or interferences, the plume was only measured to well-defined boundaries. In Fig. 61, this was to the grey area as shown.

Unfortunately, it was not easy to determine the center and fringes of the plume for all sweeps. This problem was exacerbated when using the automatic processing software, because plume break-up, multiple centers, high plume rise, and irregular shapes led to fragments of the plume being included in many of the derived parameters, resulting in greater widths and heights than actually occurred. To overcome this problem, the data from September 29th was manually analyzed and all parameters compared to this manual pattern recognition analysis. It was found that for the standard deviation in the horizontal the derived parameter dhor (signal-weighted absolute deviation in the horizontal about xmedian) and for the standard deviation in the vertical dver (signal-weighted absolute deviation in the vertical about zmedian) provided the best results. These parameters were then used for further analysis.

3.2.4.3 Plume characterization results

The data analysis procedure defined in previous section yielded the in-situ analysis results shown in Table 10.

Table 10: Final Plume Characterization Derived Parameters

Date	Total # of Aircraft Scanned	Total # of Aircraft Types Scanned	Total # of Scans	Derived Parameters (meters)					
				Full Data Set			2nd Highest Plume Center Data Set		
				σ_y	σ_z	Plume Rise	σ_y	σ_z	Plume Rise
26-Sep	73	21	503	12.0	4.3	8.5	13.8	5.1	10.1
29-Sep	140	22	619	10.8	3.8	7.2	11.2	3.6	7.0
30-Sep	129	21	672	11.0	4.5	8.3	11.2	4.7	8.9
Averages of All Three Days				11.2	4.2	8.0	11.2	4.3	8.4

If the overall averages of the three days are compared to the overall derived parameters from the LAX measurements campaign (σ_y = 10.5 meters, σ_z = 4.1 meters, Plume Rise = 12 meters), it can be seen that the standard deviations of the plume width and height are very similar. Plume rise was less at UNA-UNA than at LAX by approximately 3.6

meters, but it was still relatively close, and therefore tends to validate the previous results.

Statistical testing of the data was also used to determine if variance in the weather or the type of aircraft resulted in correlated changes with the determined plume parameters. This testing was done by first combining key measured data with reported meteorological data taken at the airport by NOAA.

3.2.4.4 Statistical Testing of Airfield Data for Changes Due to Weather and/or Aircraft Types

Data were analyzed to see if trends existed either for aircraft types or key weather parameters (temperature, wind speed, and wind direction). This section presents these results.

3.2.4.4.1 Aircraft Type Trends

Results from LAX seem to indicate a difference based on the aircraft, especially the location of the engine mounting. Aircraft measurements were divided into the same three groupings as at LAX: wing mounted engines, fuselage mounted engines, and commuter aircraft. Table 11 shows the results for the three plume parameters for this analysis.

Table 11: Aircraft Type Analysis Results for Airfield Sampling

	Wing Mounted			Fuselage Mounted			Commuter		
Date	Plume Rise (m)	hor std dev (m)	vert std dev (m)	Plume Rise (m)	hor std dev (m)	vert std dev (m)	Plume Rise (m)	hor std dev (m)	vert std dev (m)
Sept. 26	8.9	13.6	4.7	12.6	16.5	6.2	7.1	8.7	3.6
Sept. 29	6.4	13.1	3.3	9.7	11.7	5.0	4.6	7.6	2.3
Sept. 30	9.1	13.3	4.4	12.3	12.0	6.6	5.4	8.2	3.0
Average	7.9	13.3	4.0	11.4	13.2	5.9	5.3	8.1	2.8

The aircraft type results in Table 10 were compared to the LAX results in Table 12:

Table 12: Aircraft Type Analysis for the LAX campaign

Wing Mounted			Fuselage Mounted			Commuter		
Plume Rise (m)	hor std dev (m)	vert std dev (m)	Plume Rise (m)	hor std dev (m)	vert std dev (m)	Plume Rise (m)	hor std dev (m)	vert std dev (m)
11.1	11.0	3.8	14.6	10.0	4.8	12.1	10.3	4.1

114

Comparison of the Delta-Atlanta Hartsfield and LAX results above reveals that plume rise is similar at both venues for wing and fuselage mounted aircraft, and plume rise is lower at LAX for commuter aircraft. Horizontal and vertical standard deviations were substantially lower for wing mounted and fuselage aircraft at Delta-Atlanta Hartsfield than at LAX, and somewhat lower for commuter aircraft.

3.2.4.4.2 Meteorological Analysis

Plume rise and plume spread can be influenced by local meteorological variables such as temperature, wind speed, wind direction, and turbulence. The temperature difference between the ambient air and the jet exhaust provide thermal buoyancy that leads to both plume rise and vertical dispersion. The wind speed acts against this vertical motion and may cause the plume rise and vertical plume spread to be reduced. The wind direction could have an effect on the initial parameters if it is blowing across the runway as compared to along the runway. As such, each of these parameters was analyzed by comparing the NOAA reported meteorological parameters with the initial plume parameters. Turbulence could also have an effect on these initial parameters but insufficient information existed to evaluate turbulence. Each of the three evaluated meteorological variables is discussed below.

Temperature Effects
In general, plume rise occurs due to the plume's initial thermal buoyancy and its vertical momentum, as was discussed in the LAX report. Plume rise has been studied intensely for stationary sources such as stacks and semi-empirical equations have been developed and successfully applied in predicting plume rise. The important variables used in these approaches often include the wind speed, downwind distance, and heat emission rate (Stern, 1976). This allows many of the derived models to take the form:

$$\Delta h(x) = \text{constant } (Q_h)^a (x)^b (u)^c \qquad\qquad \text{(Eq. 39)}$$

where:

$\Delta h(x)$ = plume rise as a function downwind
Q_h = heat emission rate
x = distance downwind
u = wind speed at source height
a,b,c = constants

As at LAX, the derived stationary approach cannot be used in this case because most of the equations include the vertical velocity of the release, common for stationary sources. Also, due to the horizontal release of the aircraft engine, vertical momentum/vertical kinetic energy is small when compared to thermal buoyancy. If the jet exhaust is considered to have the properties of air, the thermal buoyancy is a function of the difference in the absolute temperature of the jet exhaust and the ambient air.

The internal temperature of the primary combustion zone of a modern jet/turbine engine can reach 2000K. However, the temperatures at the turbine are closer to about 1300 K and as such, the exhaust stream from the core engine will be in the range of 1000 K or greater. This temperature is reduced considerably by mixing with the ambient air and the bypass air of modern turbofan engines. Regardless, the exhaust temperature of the engine is still far above the ambient temperature. This leads to a large heat emission rate and as such, a large amount of thermal buoyancy.

Fig. 62 shows an analysis of the plume rise vs. ambient temperature. As at LAX, no correlation was shown, with the best fit being an exponential equation with an R^2 of only 0.014. This would seem to indicate, just as at LAX, that the high exhaust temperature are more important than a few degrees change in ambient temperature. At Delta – Atlanta Hartsfield there was only about an 8 Degrees K change in ambient temperature over the course of the measurement period. Additionally, the weather data, which was only reported once per hour, most likely was a reason for the low correlation. More refined data on shorter time increments may improve these correlations.

As at LAX, this would seem to indicate that Equation 39 could be reduced to only a function of the heat emission rate or thermal flux as shown in Equation 40:

$$\Delta h(x) = \text{constant } (Q_h)^a \qquad\qquad (\text{Eq. 40})$$

As at LAX, this implies that high temperature of the jet turbine exhaust is the overriding variable for the plume rise.

For completeness, the plume horizontal and vertical standard deviations were compared to ambient temperature. Figs. 63 and 64 show that no significant correlation was shown (just as at LAX).
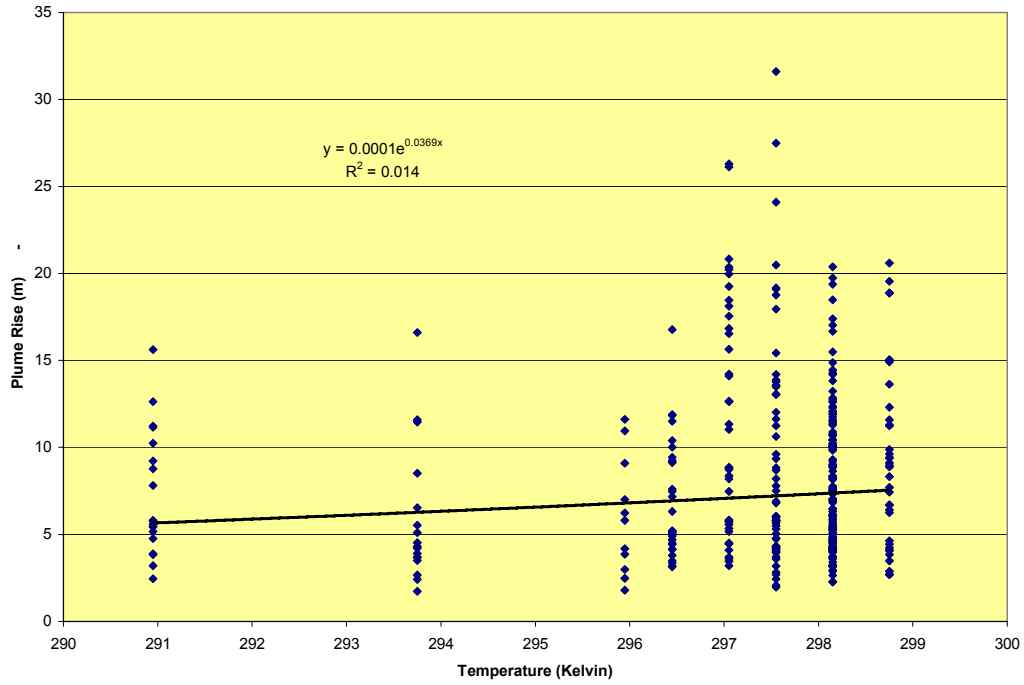
Figure 62: Plume Rise vs. Ambient Temperature
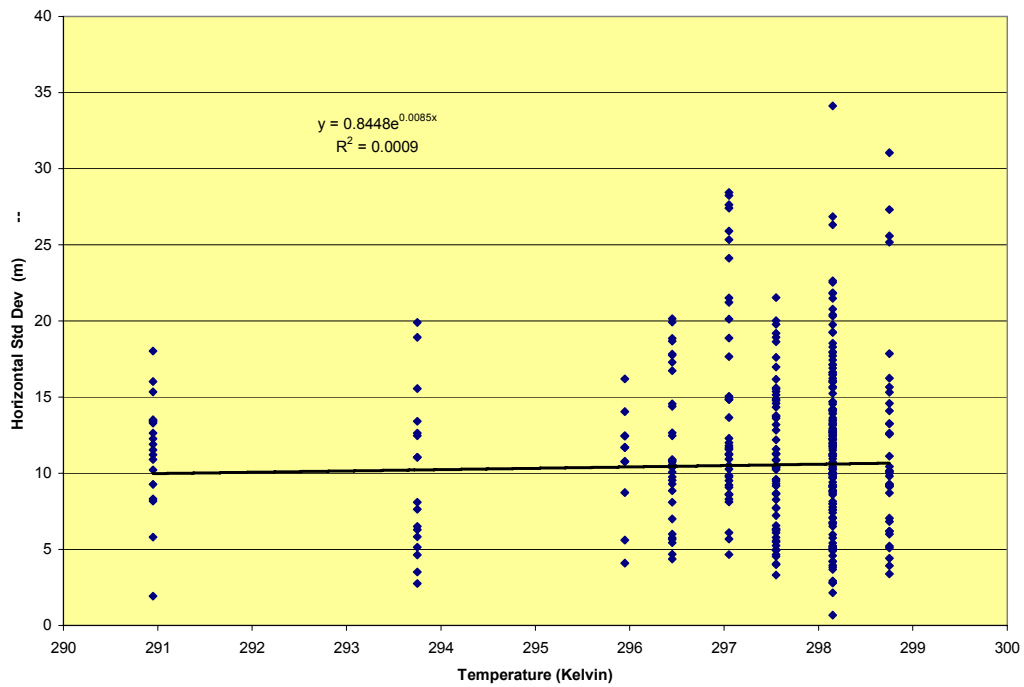
Figure 63: Horizontal Standard Deviation vs. Ambient Temperature

117
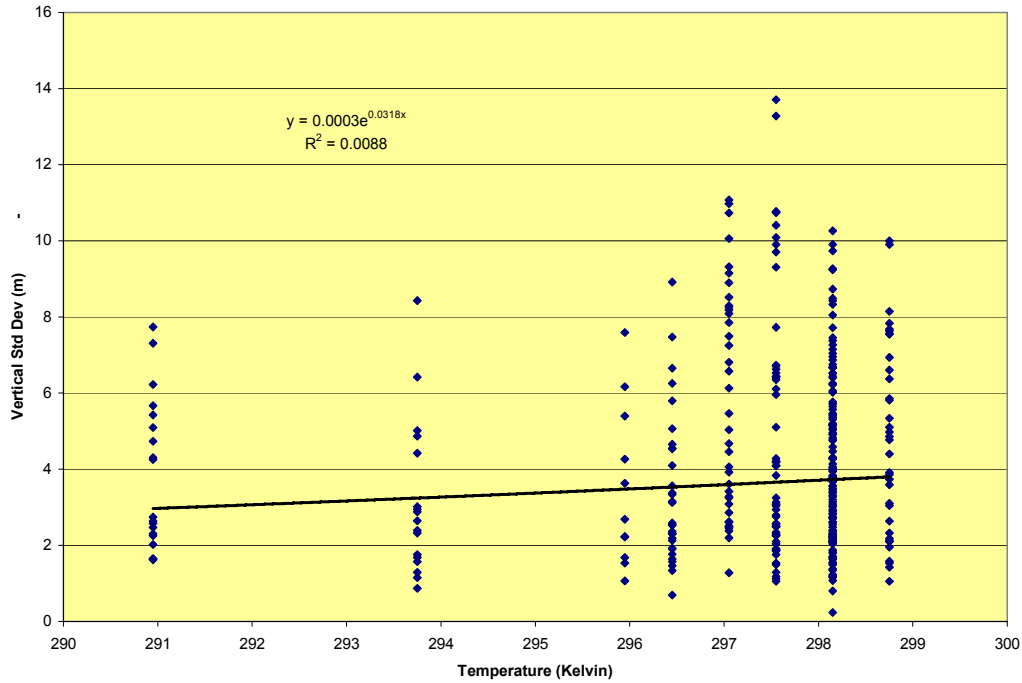
Figure 64: Vertical Standard Deviation vs. Ambient Temperature

Wind Speed Effects

Wind speed effects, including the direction, add a vector consideration to the wind. Plume rise and the derived plume standard deviations were evaluated to see if there was a correlation. Wind speed vs. the three parameters is shown in Figs. 65, 66 and 67. As with LAX, no correlation was shown.

Wind Direction Effects

Again, for completeness, wind direction was also tested with the three plume parameters, as shown in figures 68, 69 and 70. As with LAX, no correlation was shown. Again, it should be noted that hourly averages of the weather parameters from the NOAA database were used, which may affect these correlations.
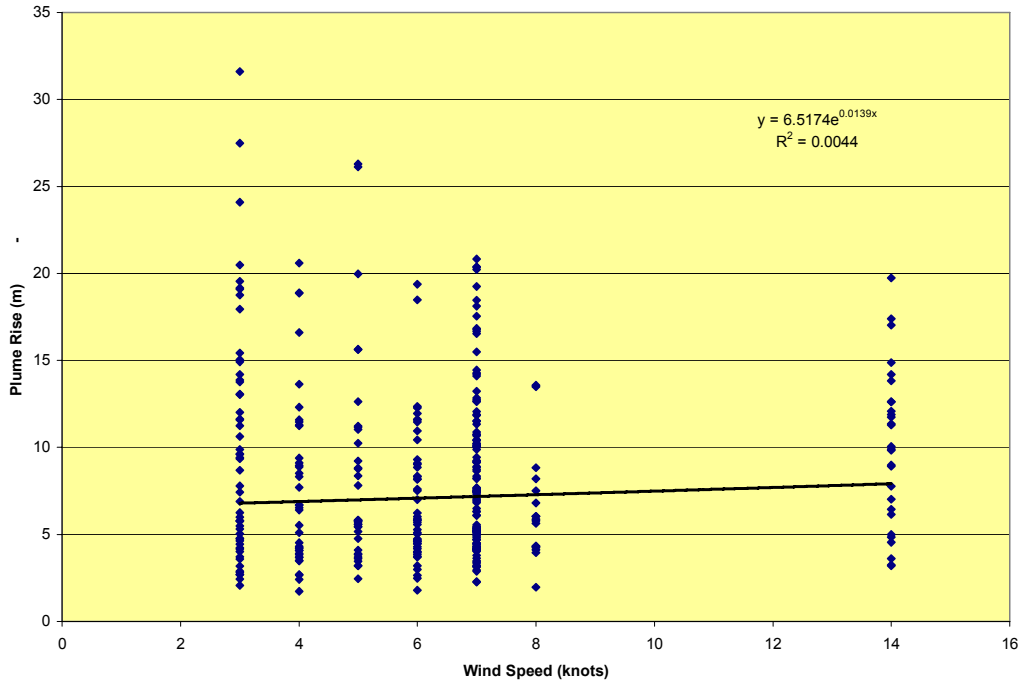
Figure 65: Wind Speed vs. Plume Rise
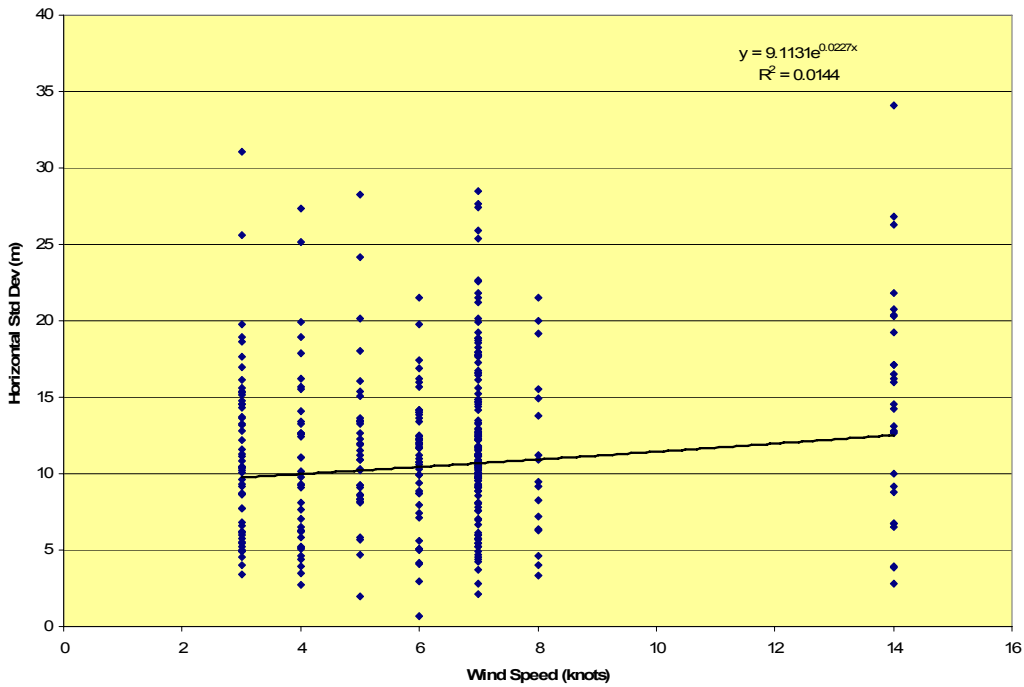
Figure 66: Wind Speed vs. Horizontal Standard Deviation
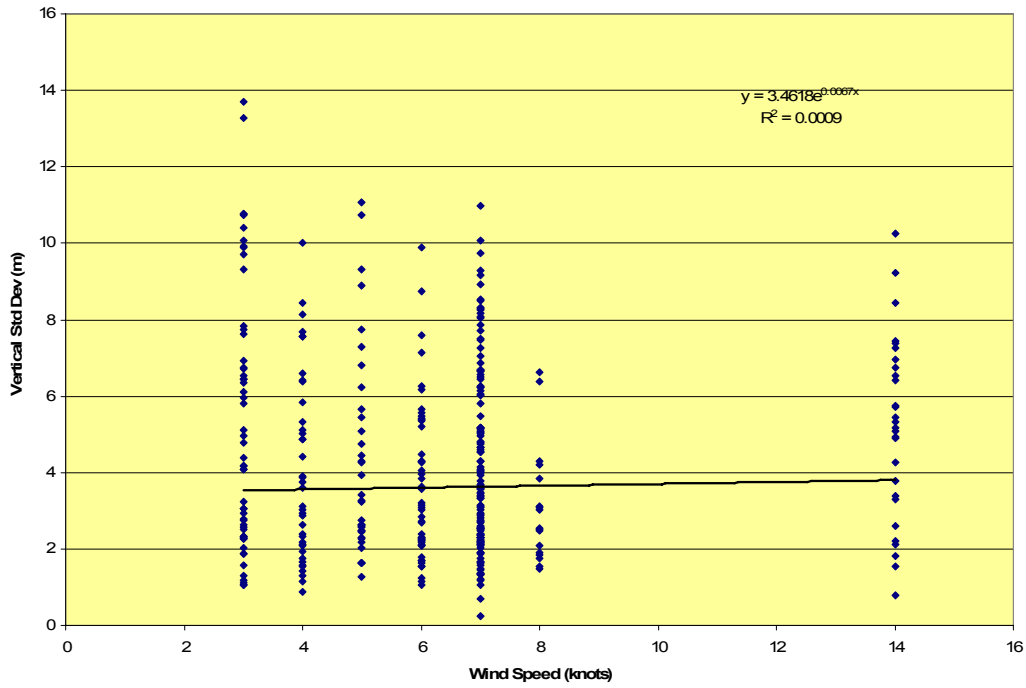
Figure 67: Wind Speed vs. Vertical Standard Deviation
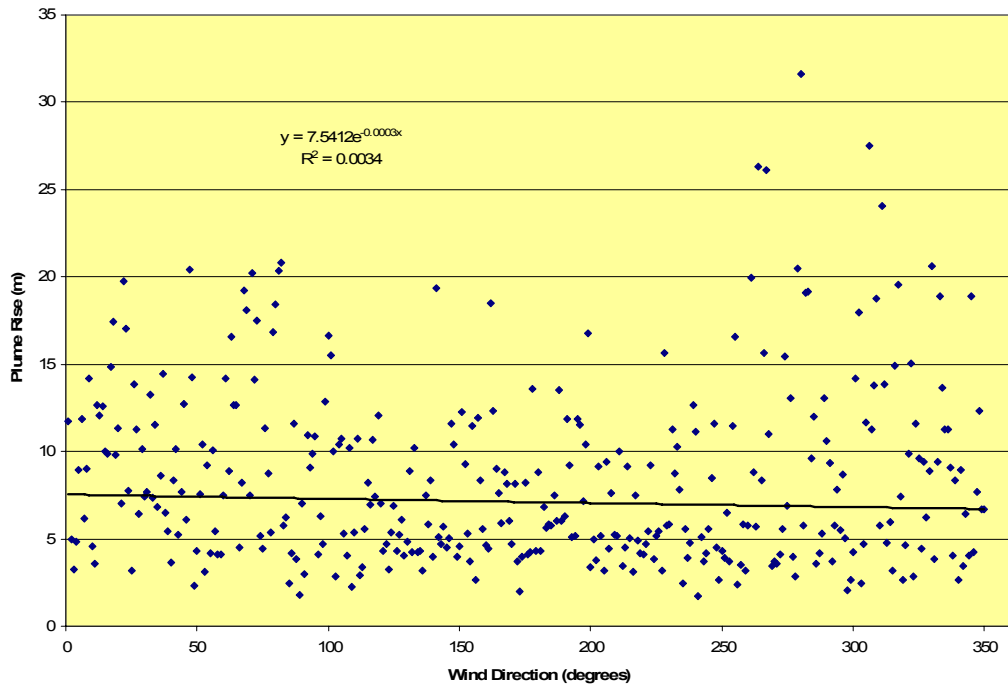
Figure 68: Wind Direction vs. Plume Rise
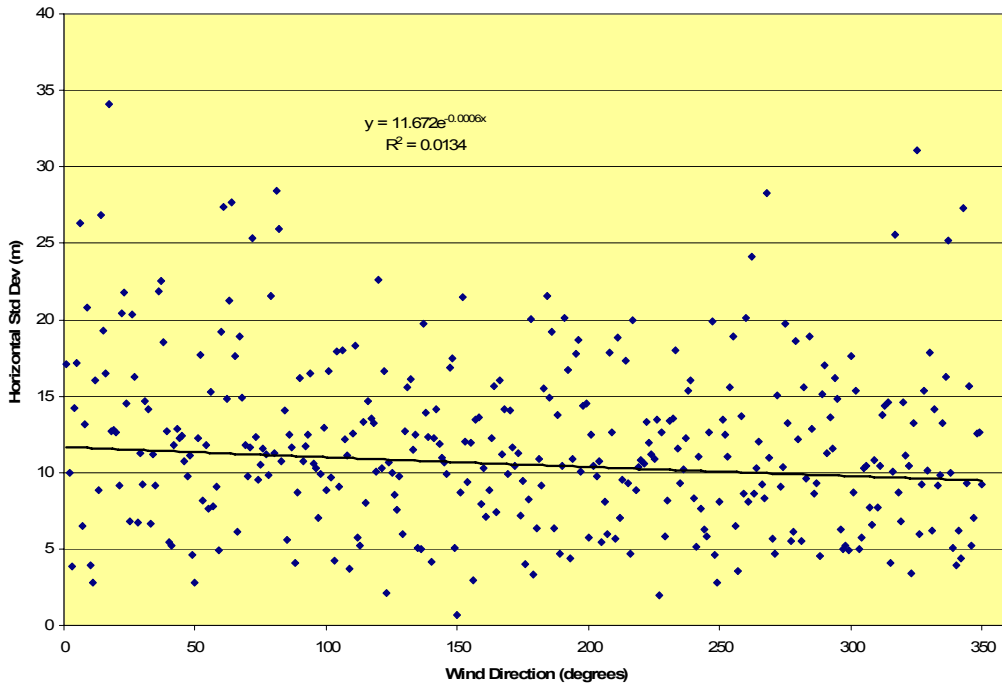
Figure 69: Wind Direction vs. Horizontal Standard Deviation
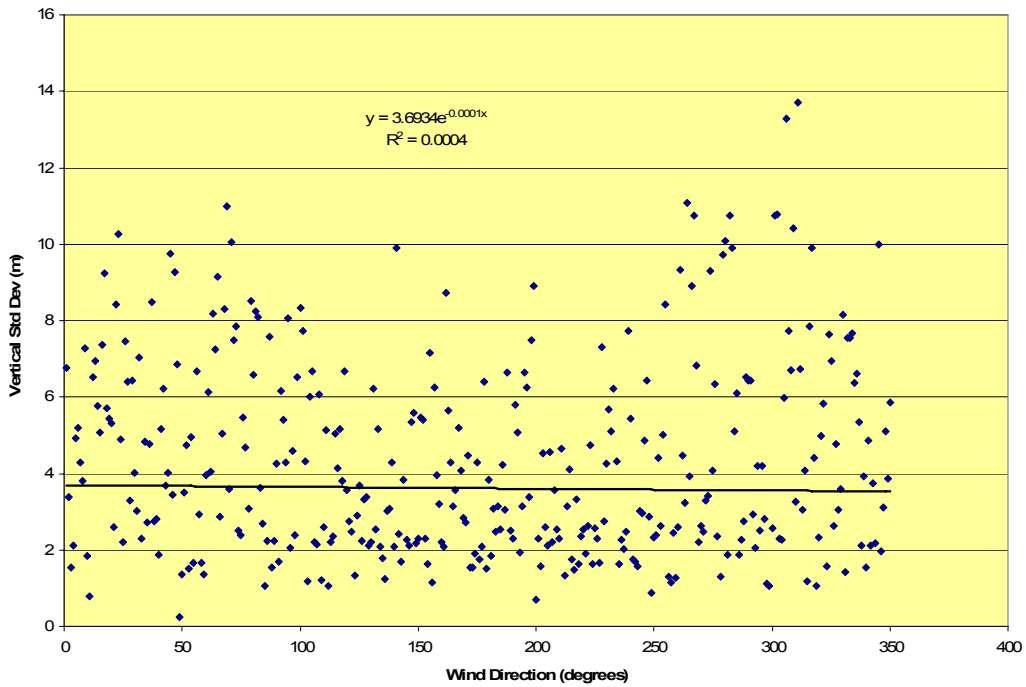
Figure 70: Wind Direction vs. Vertical Standard Deviation

3.2.4.5 Differences between the LAX and UNA-UNA studies

Since it can be assumed that the aircraft are similar, then a local condition must be causing these differences. A review of weather conditions for both tests show the temperatures to be similar. However, although the range of wind speeds was approximately the same, the wind speeds were generally lower at Delta-Atlanta Hartsfield. This could explain the plume not spreading as far for the commuter aircraft. It does not however explain the plume rise being less at Delta-Atlanta Hartsfield. Additional efforts are needed to further understand the effects of stability on the plume rise.

Two other differences in sampling at Delta-Atlanta Hartsfield may have also contributed to the lesser plume rise than obtained at LAX. First, the LIDAR's better elevation angle precision allowed measurements closer to the ground and a more accurate and slightly lower plume center than in the LAX mode. The sweep time at Delta-Atlanta Hartsfield was twice as long as at LAX, resulting in ~ ½ as many sweeps for each aircraft. The second highest sweep at Delta-Atlanta Hartsfield tended to be a little closer to the aircraft and hence not quite as high.

3.3 Deliquescence Experiments Results

Fig. 71 shows the comparison of tests while sampling at the engine exit plane (1 m probe) and tests done alongside the runway or taxiway (approximately 100 m away). There is a large increase in the SMF for the runway study as compared to the tests done at the engine exit plane. Also, there is no substantial variation in SMF from one engine to another.
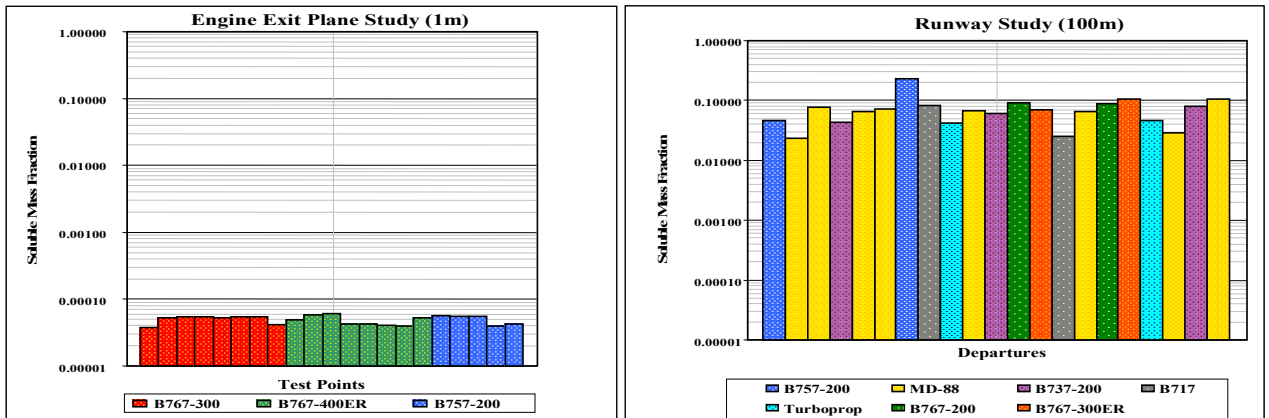
Figure 71: Comparison of SMF values obtained at the engine exit plane and alongside an active runway/taxiway using the UMR Deliquescence apparatus.

4.0 Summary and Conclusions

The following can be summarized from the analysis of the data from the dedicated engine tests:

For the JT8Ds, Dgeom increases with engine power setting from minima ~20nm to maxima ~ 40nm. Sigma increases slightly with power from ~1.7 at low power to ~1.8 at high power. DgeomM exhibits a minimum ~30% power with relatively high values at low and high power. EIn is higher at the low power conditions, exhibits a minimum at 30% power and then increases with power. EIm is similar to EIn, higher at the low power conditions, exhibits a minimum at 30% power and then rapidly increases with power. These trends are consistent with behavior of the CFM56-2C1 engine studied in the APEX campaign.

The two JT8D engines in this study have the greatest black carbon emission indices. This is due to a prevalent soot mode at 40-80 nm (particle mobility diameter). The CF6 and PW2037 engines emit soot in a smaller size mode, < 50nm with overall less total black carbon mass. These engines, however, have a greater particle number emission index than the JT8D. Anecdotally, the JT8D emits fewer but larger particles while engines designed to reduce smoke number certification measurements emit more numerous quantities of smaller particles.

Studies for CF6-80s were confined to low and mid power conditions due to probe rake limitations. In contrast to the JT8Ds, no statistically meaningful power dependence was observed. The range of low and mid power PM parameters for the CF6-80s were comparable to those for the JT8Ds.

Data for the PW2037 again suggests a trend of increasing emissions with power, but high power points were not sampled due to probe rake limitations. It should be noted that in other engines studied (JT8D, CFM56) it was the high power points that made the power dependency most evident. The range of low and mid power PM parameters for the PW2037s were also comparable to those for the JT8Ds.

From least EIn to greatest, the trend is CF6-80C2B8F, PW2037, JT8D-219 and CF6-80A2. The AMS Organic particulate loading qualitatively correlates with the ICAO UHC with a couple of outliers in the JT8D-219. This is reasonable since the mechanism leading to incomplete combustion and unburned hydrocarbons is also likely to produce partially combusted low volatility species which can either participate in nucleation or condense to available soot surface area. In the case of the JT8D-219 engine, the latter is quite likely due to the presence of a relatively greater black carbon emission index.

From the LIDAR analysis, similar trends for the MD88s, CF6-80s and PW2037s are observed. The MD88's (JT8D engines) exhibited strong emissions at high power settings, substantial emissions at idle (4%) and taxi (7%) power settings, and low emissions at other power settings. The B767's (CF6-80 engines) had low emissions, even negative values. (It is of course impossible to have negative soot emissions, but the noise in the

data, nonuniform ambient, and imperfections in the theory could all contribute to negative values of *EI*. These negative *EI* values help indicate the limits of accuracy in the current LIDAR method). The B757's (PW2037 engines) had emission index values that overall were between those of the MD88's and the B767's. Differences between the two aircraft of one type were smaller than differences between types of aircraft.

The characteristic of advected plumes - plume rise and plume spread (horizontal and vertical) were measured using the LIDAR technique. These measured parameters are key variables in dispersion modeling and are being used to help in model development.

The following can be summarized from the analysis of the data from the airport study:

Due to the vast nature of this dataset, analysis is still ongoing for many of the plumes observed. In order to demonstrate the potential of this dataset, two specific subset analyses were presented. The first encompassed 12 aircraft plume events that were selected for detailed analysis. These events were chosen to cover a variety of engine technologies and conditions. The following general conclusions from these selected analyses can be drawn.

- The combination of the PM and gas analysis of the advected plume provides unique identification of the engine operating condition generating the plume, i.e. idle, spool-up, maximum thrust, etc.
- When compared to engine exit plane measurements, it is clear that extensive secondary volatile aerosol formation is occurring during plume advection.
- The black carbon component of the PM emissions detected in the advected plume appears to be a strong function of engine model.

The second subset encompassed 289 takeoff plumes, sampled over the three day campaign. These plumes were selected because they were generated by six of the most common engine types, then operating at Atlanta Hartsfield. Daily engine by engine averages of PM number- and mass-based emission indices have been calculated. It should be noted that the emission indices were based on DMS500 measurements and were corrected for size dependent line loss. Since most of the particles have diameters <20nm, these line losses significantly impact the number-based emission index calculations. For all engines, for all days, the following range of values was observed:

EIn: $3*10^{16} – 2*10^{17}$ particles/kg fuel
EIm: 0.1 – 0.35 g/kg fuel

These averages, based on measurements of PM emissions from in-service aircraft under normal operating conditions, give credence to the rough averages reported by Penner et al., 1999 in the IPCC report – *Aviation and the Global Atmosphere*.

References

Alofs, D.J. (1978). "Performance of a dual-range cloud nucleus counter", *J. Appl. Meteor.*, 17:1286-1297.

Alofs, D.J. and Trueblood, M.B., (1981)."UMR dual mode CCN counter (Modes: CFD plus Haze)", *J. Rech. Atmos.*, 15:219-223.

Anderson, B. E.; Cofer, W. R.; Bagwell, D. R.; Barrick, J. D.; Hudgins, C. H.; Brunke, K. E., (1998). "Airborne observations of aircraft aerosol emissions I: Total nonvolatile particle emission indices", Geophys Res. Lett., 25, 1689-1692.

Anderson, B. E., Branham, H.-S., Hudgins, C. H., Plant, J. V., Ballenthin, J. O., Miller, T. M., Viggiano, A. A., Blake, D. R., Boudries, H., Canagaratna, M., Maike-Lye, R. C., Onasch, T., Wormhoudt, J., Worsnop, D., Brunke, K. E., Culler, S., Penko, P., Sanders, T., Han, H.-S., Lee, P., Pui, D. Y. H., Thornhill, K. L., and Winstead, E. L., "Experiment to Characterize Aircraft Volatile Aerosol and Trace-Species Emissions (EXCAVATE)". NASA/TM-2005-213783, Hampton, VA, August 2005.

Bond, T. C., and R. W. Bergstrom (2006). Light absorption by carbonaceous particles: An investigative review. *Aerosol Sci. Technol.* 40, 27-67.

Biskos, G., Reavell, K., and Collings, N., (2005). "Description and Theoretical Analysis of a Differential Mobility Spectrometer", *Aerosol Sci. Technol.,* 39, 527-541.

Dutton, J. A. (chair), "Committee on Aeronautics Research and Technology for Environmental Compatibility Report: For Greener Skies – Reducing Environmental Impacts of Aviation", National Research Council, Washington D.C., 2002, ISBN: 0-309-08337-0.

Eberhard, W.L., W.A. Brewer, and R.L. Wayson (2005). Lidar observation of jet engine exhaust for air quality. *Second Symp. on Lidar Appl., Combined Preprints CD-ROM, 85th AMS Ann. Mtg,* San Diego, (Amer. Meteorol. Soc.), #3.4

Fahey, D. W., E.R. Keim, K.A. Boering, C.A. Brock, J.C. Wilson, H.H. Jonsson, S. Anthony, T.F. Hanisco, P.O. Wennberg, R.C. Miake-Lye, R.J. Salawitch, N. Louisnard, E.L. Woodbridge, R.S. Gao, S.G. Donnelly, R.C. Wamsley, L.A. Del Negro, S. Solomon, B.C. Daube, S.C. Wofsy, C.R. Webster, R.D. May, K.K. Kelly, M. Loewenstein, J.R. Podolske, K.R. Chan (1995). "Emission measurements of the Concorde Supersonic aircraft in the lower stratosphere", Science, 270, 70-74.

Hagen, D.E., Trueblood, M.B., Whitefield, P.D. (1992). "A Field Sampling of Jet Exhaust Aerosols", *Particle Sci. Technol.*, 10, 53-63

Hagen, D., Whitefield, P., Paladino, J., Trueblood, M., and Lilenfeld, H. (1998). "Particulate Sizing and Emission Indices for a Jet Engine Exhaust Sampled at Cruise," *Geophys. Res. Lett.*, 25, 1681–1684.

Hall, C. T., Thrasher, T. G., Draper, J. A., Holsclaw, C. A., Wayson, R. L., Kim, B. Y., and Fleming, G. G. (2003). FAA EDMS airport air quality model development. *Proc. 96th Ann. Mtg. AWMA*, San Diego, (Air and Waste Management Assoc.), #69574.

Herndon, S. C.; Shorter, J. H.; Zahniser, M. S.; Nelson, D. D. J.; Jayne, J. T.; Brown, R. C.; Miake-Lye, R. C.; Waitz, I. A.; Silva, P.; Lanni, T.; Demerjian, K. L.; Kolb, C. E., (2004). "NO and NO2 Emissions Ratios Measured from in use Commercial Aircraft during Taxi and Take-Off", Environ. Sci. Technol., 38, 6078-6084.

Herndon, S. C.; Onasch, T., B.; Frank, B. P.; Marr, L. C.; Jayne, J. T.; Canagaratna, M. R.; Grygas, J.; Lanni, T.; Anderson, B. E.; Worsnop, D. R.; Miake-Lye, R. C. (2005). "Particulate emissions from in-use Commercial aircraft", Aerosol Sci. Technol., 39, 799-809.

Herndon, S. C.; Yongquan, L.; Nelson, D. D.; Zahniser, M. S. (2005). "Determination of line strengths for selected transitions in the nu2 band relative to the nu1 and nu5 bands of H2CO", JQSRT, 90, 207-216.

Herndon, S. C.; Rogers, T.; Dunlea, E. J.; Jayne, J. T.; Miake-Lye, R. C., and Knighton, B. (2006). "Hydrocarbon emissions from In-use Commercial Aircraft during Airport Operations", Environ. Sci. Technol., 40, 4406-4413.

Horii, C. V.; Zahniser, M. S.; Nelson, D. D. J.; McManus, J. B.; Wofsy, S. C. (1999). "Nitric Acid and Nitrogen Dioxide Flux Measurements: a New Application of Tunable Diode Laser Absorption Spectroscopy", Proceedings of the SPIE Conference on Atmospheric Sensing.

Horvath, H. (1993) Atmospheric light absorption – a review. *Atmos. Env.*, 27A, 293-317.

ICAO, International Civil Aviation Organization *Aircraft Engine Emissions DataBank.* (2006)

Jimenez, R.; Herndon, S. C.; Shorter, J. H.; Nelson Jr., D. D.; McManus, J. B.; Zahniser, M., "Atmospheric trace gas measurements using a dual quantum-cascade laser mid-infrared absorption spectrometer", SPIE Proceedings 2005, 5738, 318.

Kolb, C. E.; Herndon, S. C.; McManus, J. B.; Shorter, J. H.; Zahniser, M. S.; Nelson, D. D.; Jayne, J. T.; Canagaratna, M. R.; Worsnop, D. R. (2004). "Mobile Laboratory with Rapid Response Instruments for Real-time Measurements of Urban and Regional Trace Gas and Particulate Distributions and Emission Source Characteristics", Environ. Sci. Technol., 38, 5694-5703.

Li, W., Montassier, N. and Hopke, P. (1992). "A System to Measure the Hygroscopicity of Aerosol Particles", *Aerosol Sci. Technol.,* 17:25-35.

Li, Y.; Schwab, J.; Roychowdhury, U.; Ren, X.; Brune, W.; Karcher, R.; Zahniser, M. S.; Nelson, D. D. J.; Herndon, S. C.; Demerjian, K. L., "Intercomparison of formaldehyde, sulfur dioxide and nitrogen dioxide measurement techniques during the PMTACS-NY Summer 2002 Campaign at Whiteface Mountain", 2003.

Lobo, P., Hagen, D.E., Whitefield, P.D., and Alofs, D.J. (2007). "Physical characterization of aerosol emissions from a Commercial Gas Turbine Engine", *Journal of Propulsion and Power*, 23, 919-929.

Mishchenko, M., J. W. Hovenier, and L.D. Travis (2000). *Light Scattering by Nonspherical Particles*. Academic Press.

Penner, J. E., Lister, D. H., Griggs, D. J., Dokken, D. J., and McFarland, M. (eds.), *Aviation and the Global Atmosphere*, IPCC Report, Cambridge University Press, Cambridge, UK, 1999, p. 373.

McManus, J. B.; Kebabian, P. L.; Zahniser, M. S., (1995)."Astigmatic mirror multipass absorption cells for long-path-length spectroscopy", Appl. Opt., 39, 6866 – 6872.

Samet, J. M., Dominici, F., Curriero, F. C., Coursac, I.,and Zeger, A. L. (2000), "Fine Particulate Air Pollution and Mortality in 20 U. S. Cities, 1987-1994", *N. Engl. J. Med.*, 343, 1742-1749.

Schäfer, K.; Jahn, C.; Sturm, P.; Lechner, B.; Bacher, M., (2003)."Aircraft emission measurements by remote sensing methodologies at airports", Atmos. Environ. 37, 5261-5271.

Schlichting, H., and K. Gersten (2000). *Boundary Layer Theory*. Springer-Verlag.

Schmid, O., Hagen, D.E., Whitefield, P.D., Trueblood, M.B., Rutter, A.P., Lilenfeld, H.V. (2004). "Methodology for Particle Characterization in the Exhaust Flows of Gas Turbine Engines", *Aerosol Sci. Technol., 38*, 1108-1122.

Smith, M. A. H.; Rinsland, C. P.; Fridovich, B.; Rao, K. N. In Molecular Spectroscopy: Modern Research; Academic Press, Inc., 1985; Vol. Chapter 3.

Sorenson, C. M. (2001). Light scattering by fractal aggregates: A review. *Aerosol Sci. Technol.* 35, 648-687.

Stern, A.C. (ed.), Air Pollution, 3rd Edition, Volume I, Academic Press, New York, 1976.

Volkamer, R., "Comparison of the absorption cross-section of HCHO in the UV and IR spectral ranges", Personal Communication 2005, 1-3.

Waitz, I. A., Townsend, J., Cutcher-Gershenfeld, J., Greitzer, E. M., and Kerrebrock, J. L. "Aviation and the Environment: A National Vision Statement, Framework for Goals and Recommended Actions," *Report to the United States Congress*, on behalf of the U.S. DOT, FAA and NASA, December 2004

Wayson, R.L., Fleming, G.G., Kim, B., Eberhard, W.L., Brewer, W. A., Final Report – "The Use of LIDAR to Characterize Aircraft Initial Plume Parameters", FAA-AEE-04-01, DTS-34-FA34T-LR3, Federal Aviation Administration, Office of Environment and Energy, Washington, D.C., February 2004.

Wayson, R. L., G.G. Fleming, B. Kim, W. L. Eberhard, W. A. Brewer, J. Draper, J. Pehrson and R. Johnson (2003). "The use of LIDAR to characterize aircraft exhaust plumes." *Proc. 96th Ann. Mtg. AWMA*, San Diego, CA, (Air and Waste Management Assoc.), #69965.

Wey, C.C., Anderson, B.E., Hudgins, C., Wey, C., Li-Jones, X., Winstead, E., Thornhill, L.K., Lobo, P., Hagen, D., Whitefield, P., Yelvington, P. E., Herndon, S.C., Onasch, T.B., Miake-Lye, R.C., Wormhoudt, J., Knighton, W.B., Howard, R., Bryant, D., Corporan, E., Moses, C., Holve, D., and Dodds, W. "Aircraft Particle Emissions eXperiment (APEX)" NASA/TM-2006-214382, ARL-TR-3903, Cleveland, OH, September 2006.

Wilson, C. W., Petzold, A., Nyeki, S., Schumann, U., and Zellner, R. (2004). "Measurement and Prediction of Emissions of Aerosols and Gaseous Precursors from Gas Turbine Engines (PartEmis): An Overview", *Aerospace Science and Technology*, 8, 131–143.

Whitefield, P.D. and Hagen, D.E. (1995). "Particulates and aerosol sampling from combustor rigs using the UMR mobile aerosol sampling system (MASS)", AIAA (Amer. Institute of Aeronautics and Astronautics) paper No. 95-0111.

Whitefield, P.D., Hagen, D.E., and Lilenfeld, H.V. (1997). "Ground based measurements of particulate emissions from supersonic transports - Concorde Olympus engine", Proc. of the Comite Avion Ozone International Colloquium I:119-124.

Whitefield, P., Hagen, D., Siple, G., and Pherson, J. (2001). "Estimation of particulate emission indices as a function of size for the LTO cycle for commercial jet engines", A&WMA Conf. Proc. #347.

Whitefield, P. "Testing of Particulate Matter Sampling Technology at a North American Airport", *PARTNER Newsletter* 2005, Vol.2 (1), 1-2.

Wormhoudt, J., Herndon, S. C., Yelvington, P. E., Miake-Lye, R. C., and Wey, C. (2007) "Nitrogen Oxide (NO/NO2/HONO) Emissions Measurements in Aircraft Exhausts", *Journal of Propulsion and Power*, 23, 906-911.

Yelvington, P. E., Herndon, S. C., Wormhoudt, J. C., Jayne, J. T., Miake-Lye, R. C., Knighton, W. B., and Wey, C. (2007). "Chemical Speciation of Hydrocarbon Emissions from a Commercial Aircraft Engine" *Journal of Propulsion and Power*, 23, 912-918.

Zahniser, M. S.; Nelson, D. D.; McManus, J. B.; Kebabian, P. L. (1995). "Measurement of trace gas fluxes using tunable diode laser spectroscopy", Phil. Trans. R. Soc. Lond. A, 351, 371-382.

APPENDIX A:
Hartsfield- Jackson Atlanta International Airport

130

APPENDIX B:
Line loss Calibration Results

Line loss function for sampling train associated with the dedicated engine tests

Penetration vs. Size
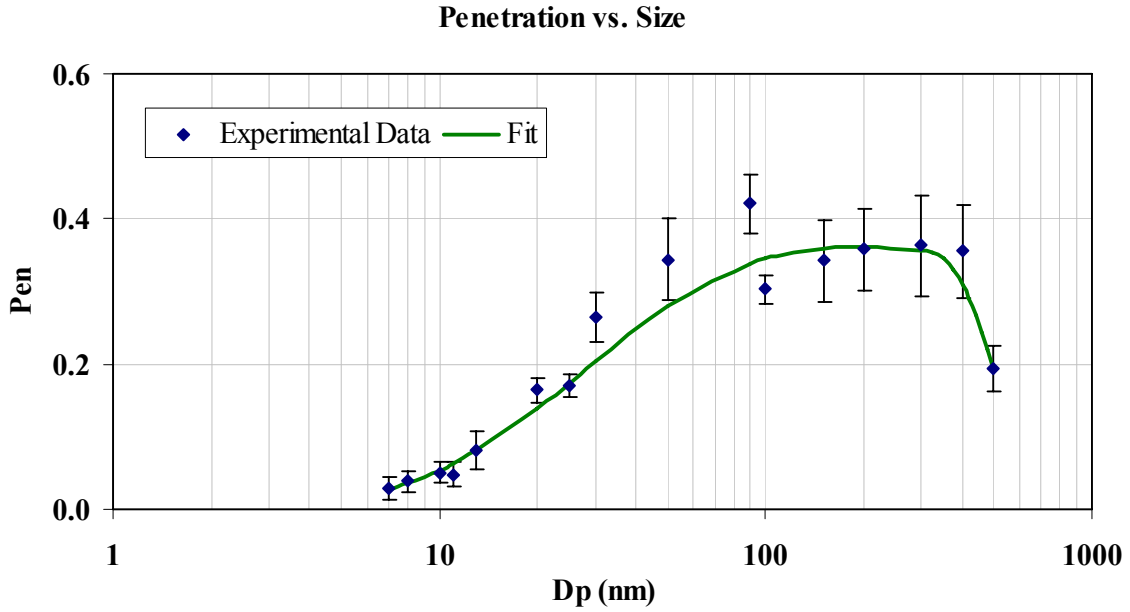
Line loss function for sampling train associated with the airport study

Penetration vs. Size
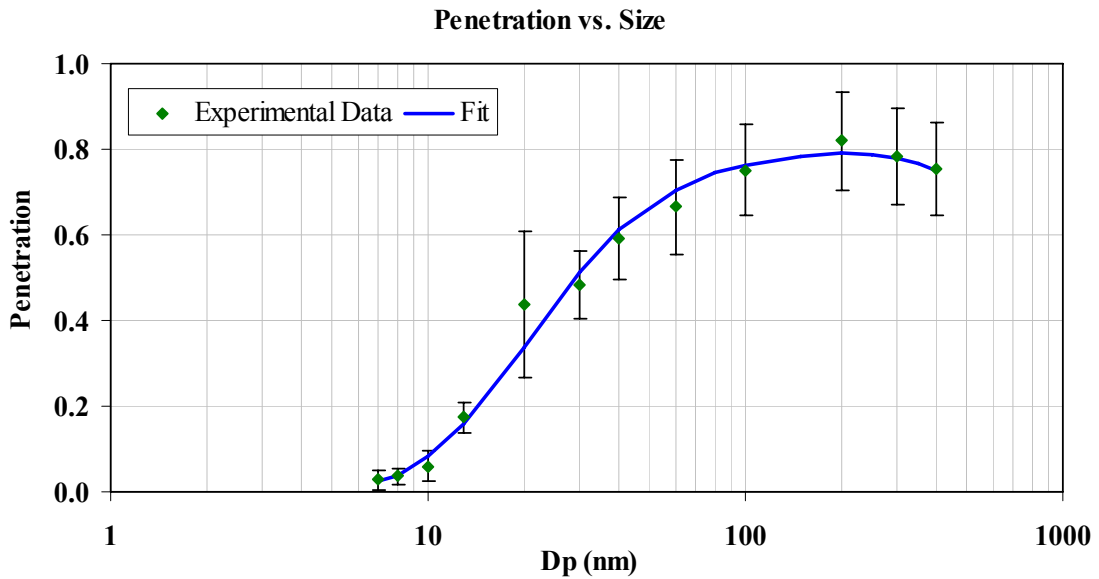
APPENDIX C:
Derived and Reported Data for LIDAR Airfield Testing

Column	Parameter	Units	Bad or missing flag	Description
A	day	(UTC)		Day of month scan started
B	month	(UTC)		
C	year	(UTC)		
D	start hour	(UTC)		Decimal time scan started: 21.5000 = 9:30 pm
E	end hour	(UTC)		Decimal time scan ended
F	tail number		XXXXXX	Aircraft tail number from spotter and/or departure log
G	A/C		XXXX	ICAO code for aircraft type
H	AL		XX	IATA code for airline
I	Sweep Dir			-1 = up, 1 = down
J	Nx			Number of horizontal elements in gridded data array
K	x0	m		Horizontal distance from lidar to nearest grid point in data array
L	Δx	m		Horizontal spacing of grid points in data array
M	Nz			Number of vertical elements in gridded data array
N	z0	m		Vertical distance from lidar to nearest grid point in data array
O	Δz	m		Vertical spacing of vertical grid points in data array
P	Engine Type			From Jane's or ICAO, retrieved by George Noel according to tail number
Q	Near pwr %		999	% power setting of engine closest to the lidar
R	Far pwr %		999	% power setting of engine farthest from the lidar
S	ST	m^2 / (Mm sr)	-999	Integrated (i.e., total) enhanced backscatter in the 2-D gridded data from the sweep
T	xmean	m	-999	Horizontal distance from the lidar of the spatial mean of the horizontal profile (signal-weighted mean location)
U	hor	m	-999	Square root of the signal-weighted spatial variance in the horizontal about xmean
V	ε1ssh		-999	Normalized absolute difference between horizontal profile data points and a Gaussian equation

				with parameters ST, xmean, and hor
W	ε2ssh		-999	Square root of normalized squared difference between horizontal profile data points and a Gaussian equation with parameters ST, xmean, and hor
X	γ1hor		-999	skewness of horizontal backscatter profile - the usefulness of these parameters has not yet been evaluated
Y	γ2hor		-999	kurtosis of the horizontal backscatter profile - the usefulness of these parameters has not yet been evaluated
Z	zmean	m	-999	Vertical distance above the runway of the spatial mean of the 2-D gridded data (signal-weighted mean location)
AA	ver	m	-999	Square root of the signal-weighted spatial variance in the vertical about the zmean
AB	ε1ssv		-999	Normalized absolute difference between vertical profile data points and a Gaussian fit using preceding three parameters
AC	ε2ssv		-999	Square root of normalized squared difference between vertical profile data points and a Gaussian fit using preceding three parameters
AD	γ1ver		-999	skewness of vertical backscatter profile - the usefulness of these parameters has not yet been evaluated
AE	γ2ver		-999	kurtosis of the vertical backscatter profile - the usefulness of these parameters has not yet been evaluated
AF	xmedian	m	-999	Horizontal distance from the lidar to the location of the signal-weighted median of the horizontal profile
AG	medh	m	-999	Horizontal standard deviation of distribution assuming a Gaussian shape possessing dhor
AH	ε1mdh		-999	Normalized absolute difference between horizontal profile data points and a Gaussian equation with parameters ST, xmed, and medh
AI	ε2mdh		-999	Square root of normalized squared difference between horizontal profile data points and a Gaussian equation with parameters ST, xmed, and medh
AJ	dhor	m	-999	Signal-weighted absolute deviation in the horizontal about xmedian
AK	zmedian	m	-999	Vertical height above the runway of the location of the signal-weighted median of the vertical profile
AL	medv	m	-999	Vertical standard deviation of distribution assuming a Gaussian shape possessing dver
AM	ε1mdv		-999	Normalized absolute difference between vertical profile data points and a Gaussian equation with parameters ST, zmed, and medv
AN	ε2mdv		-999	Square root of normalized squared difference between vertical profile data points and a Gaussian equation with parameters ST, zmed, and medv
AO	dver	m	-999	Signal-weighted absolute deviation in the vertical about zmedian
AP	68h	m	-999	Horizontal distance from xmed (averaged for the two directions) to which the integrated signal

				is 34.1% of ST, corresponding to the std dev of a Gaussian distribution
AQ	ε168h		-999	Normalized absolute difference between horizontal profile data points and a Gaussian equation with parameters ST, xmed, and h
AR	ε268h		-999	Square root of normalized squared difference between horizontal profile data points and a Gaussian equation with parameters ST, xmed, and 68h
AS	68v	m	-999	Vertical distance from zmed (averaged for the two directions) to which the integrated signal is 34.1% of ST, corresponding to the standard deviation of a Gaussian dist
AT	ε168v		-999	Normalized absolute difference between vertical profile data points and a Gaussian equation with parameters ST, vmed, and 68v
AU	ε268v		-999	Square root of normalized squared difference between vertical profile data points and a Gaussian equation with parameters ST, zmed, and 68v
AV	STpth	m^2 / (Mm sr)	-999	Total backscatter (area under the curve) of Gaussian equation with parameters Shmax, xpeak, and pth
AW	xpeak	m	-999	Horizontal distance from the lidar of STpth
AX	pth	m	-999	Std dev of dist assuming Gaussian shape and based on the distance from xpeak (averaged for the two directions) where the horizontal signal profile is < Shmax/10
AY	ε1pth		-999	Normalized absolute difference between horizontal profile data points and a Gaussian equation with parameters STpth, xpeak, and σpth
AZ	ε2pth		-999	Square root of normalized squared difference between horizontal profile data points and a Gaussian equation with parameters STph, xpeak, and pth
BA	Shmax	m / (Mm sr)	-999	Peak backscatter in the horizontal profile of enhanced backscatter
BB	STptv	m^2 / (Mm sr)	-999	Total backscatter (area under the curve) of Gaussian equation with parameters Svmax, zpeak, and ptv
BC	zpeak	m	-999	Height above the runway of STptv
BD	ptv	m	-999	Std dev of distribution assuming Gaussian shape, based on the distance from zpeak (averaged for the two directions) where the vertical signal profile is < Svmax/10
BE	ε1ptv		-999	Normalized absolute difference between vertical profile data points and a Gaussian equation with parameters STptv, zpeak, and σptv
BF	ε2ptv		-999	Square root of normalized squared difference between vertical profile data points and a Gaussian equation with parameters STpv, zpeak, and σptv
BG	Svmax	m / (Mm sr)	-999	Peak backscatter in the vertical profile of enhanced backscatter
BH	STGh(ext)	m^2 / (Mm sr)	-999	Total backscatter (area under the curve) of Gaussian equation least-squares fitted to the horizontal profile, extended with zero values on both ends
BI	xGh(ext)	m	-999	Distance from the lidar to the spatial mean location of the Gaussian equation least-squares

				fitted to the horizontal profile, extended with zero values on both ends
BJ	Gh(ext)	m	-999	Spatial standard deviation of the Gaussian equation least-squares fitted to the horizontal profile, extended with zero values on both ends
BK	ε1Gh(ext)		-999	Normalized absolute difference between horizontal profile data points and a Gaussian equation with parameters STGh, xGh, and Gh
BL	ε2Gh(ext)		-999	Square root of normalized squared difference between horizontal profile data points and a Gaussian equation with parameters STGh, xGh, and Gh
BM	STGv(ext)	m^2 / (Mm sr)	-999	Total backscatter (area under the curve) of Gaussian equation least-squares fitted to the vertical, extended with zero values on both ends
BN	zGv(ext)	m	-999	Distance above the runway of the spatial mean location of the Gaussian equation least-squares fitted to the vertical profile, extended with zero values on both ends
BO	Gv(ext)	m	-999	Spatial standard deviation of the Gaussian equation least-squares fitted to the vertical profile, extended with zero values on both ends
BP	ε1Gv(ext)		-999	Normalized absolute difference between vertical profile data points and a Gaussian equation with parameters STGv, xGv, and Gv
BQ	ε2Gv(ext)		-999	Square root of normalized squared difference between vertical profile data points and a Gaussian equation with parameters STGv, xGv, and Gv
BR	STDGh	m^2 / (Mm sr)	-999	Total backscatter (area under the curve) of double Gaussian eqn with equal amplitude each mode least-squares fitted to the hor.profile, extended with zero values at ends
BS	xDGh1	m	-999	Distance from the lidar to the center of the closer Gaussian in the double-Gaussian fit
BT	xDGh2	m	-999	Distance from the lidar to the center of the father Gaussian in the double-Gaussian fit
BU	DGh	m	-999	Standard deviation of both Gaussians in the double-Gaussian fit
BV	ε1DGh		-999	Normalized absolute difference between horizontal profile data points and the double Gaussian fit
BW	ε2DGh		-999	Square root of normalized squared difference between horizontal profile data points and the double Gaussian fit
BX	STGv	m^2 / (Mm sr)	-999	Same as for STGv(ext), but with the actual vertical profile (no extension)
BY	zGv	m	-999	Same as for zG(ext), but with the actual vertical profile (no extension)
BZ	Gv	m	-999	Same as for Gv(ext), but with the actual vertical profile (no extension)
CA	ε1Gv		-999	Same as for ε1Gv(ext), but with the actual vertical profile (no extension)
CB	ε2Gv		-999	Same as for ε2Gv(ext), but with the actual vertical profile (no extension)
CC	e	1/(mM)	-999	Ambient extinction coefficient used to process the lidar data
CD	<βh>	1/(mM sr)	-999	Haze (aerosol) backscatter coefficient in the foreplume region calculated from lidar signal, calibration, extinction correction, and subtracting m
CE	h	1/(mM)	-999	Ambient haze (aerosol) extinction coefficient = e - m

CF	βm	1/(mM sr)	-999	Molecular backscatter coefficient for air density calculated from surface temperature and pressure
CG	m	1/(mM)	-999	Molecular extinction coefficient for air density calculated from surface temperature and pressure
CH	Tp	m	-999	Vertical integral of plume optical depth assuming difference in ambient signal from post-plume and fore-plume regions is due only to plume attenuation
CI	Lp	Mm sr / m	-999	Plume's lidar extinction-to-backscatter ratio based on Tp and ST
CJ	Nabove		-999	Number of beams in the sweep above the plume as designated by the operator in sweep processing
CK	Δτabove		-999	Optical depth between foreplume and postplume regions for the Tp beams if their average difference in ambient signal were caused by extinction
CL	Δ h above	1/(mM)	-999	Average extinction coefficient corresponding to Δ above
CM	r1	m	-999	Distance between lidar and near boundary of foreplume region
CN	r2	m	-999	Distance between lidar and boundary dividing the foreplume and plume regions
CO	r3	m	-999	Distance between lidar and boundary dividing the plume and postplume regions
CP	r4	m	-999	Distance between lidar and far boundary of postplume region
CQ	F2D	m^2/(Mm sr)^2	-999	Parameter for calculation soot emission based on statistics of plume density - usefulness not evaluated yet
CR	F R	m^2/(Mm sr)^2	-999	Parameter for calculation soot emission based on statistics of plume density - usefulness not evaluated yet
CS	ST R	m^2/(Mm sr)	-999	Parameter for calculation soot emission based on statistics of plume density - usefulness not evaluated yet
CT	F 1		-999	Parameter for calculation soot emission based on statistics of plume density - usefulness not evaluated yet
CU	ST 1		-999	Parameter for calculation soot emission based on statistics of plume density - usefulness not evaluated yet
CV	# Tp grids		-999	Number of Δz levels occupied by the Tp beams

APPENDIX D:
Discussion of Errors and Improvement of LIDAR Accuracy

There are many sources of error and uncertainty in this new method, some small and others substantial. They include photon counting statistics in the measurement, spatial variations in ambient scattering, uncertainties in aircraft engine specifications and throttle settings, limitations to LIDAR calibration accuracy, inaccuracy in determining plume size and shape, uncertainty in the value of η, and simplifications in the theoretical assumptions.

A consideration of likely magnitude of these errors and uncertainties, and assuming they are independent of one another, led to a two-part uncertainty estimate for the EI values in Table 3 of $\pm (0.05\ n^{-1/2}$ g/kg$)\ \pm$ factor of 2 times EI, where n is the number of cycles with the particular power setting (Table 3). The first part of the uncertainty arises mostly from random-like errors (photon statistics and nonuniform ambient), but also the uncertainties in theory and data from which EI_{vol} and $EI_{\Delta T}$ were determined. The second part arises out of bias-like uncertainties in EI_{enh}, including η, the theoretical assumptions, the horizontal plume size, the LIDAR calibration, and engine specifications. The overall uncertainty is indeed large, but can be very much reduced.

The uncertainty in η actually has four main potential sources of error. First is the value of refractive index, for which we used the suggestion in Horvath (1993) of 2+2i and density 2.25 g cm^{-3} for pure soot. A more recent review (Bond and Bergstrom 2006) considered the refractive index of light absorbing particles and arrived at a more definitive value at 550 nm and corresponding material density than before. This paper may show the path for us to determine a more accurate value at 355 nm for engine soot. The second place for improvement is to use a scattering theory that accounts in a more rigorous and accurate way for the nonspherical shape of the particles. There are several methods (Sorenson 2001, Mishchenko et al. 2000), and one or more could be selected based on ease of implementation and expected accuracy. As indicated in Fig. 9, η depends on the characteristic size of the soot particles. Updating the LIDAR calculations with size distribution measurements from modern engines will help reduce the uncertainty in η. It would be very helpful to learn from such measurements if the mean geometrical mass diameter of the size distribution tends to depend on EI, e.g., if the diameter tends to increase with EI. In that case, Eq. 31 would need to be modified to have a functional relationship between η and EI. Finally, the possibility also exists that the particles from the engine detected by the LIDAR are not entirely soot. Particle growth by organic gas deposition will occur as the plume ages. New particles will also be formed, but these will be very small and not add significantly to the LIDAR backscatter. The uncertainty in η is a principal part of the overall uncertainty and should be a topic of future research to improve accuracy of the LIDAR method.

LIDAR calibrations from this project had an estimated error margin of ±30%. More careful and complete calibration procedures in the future can halve the calibration errors.

The horizontal size of the exhaust plume was estimated rather than measured in the stationary tests. The scan plane was close to the tail where the plume was still quite narrow, and the 5-m range resolution of the LIDAR could not resolve the plume's horizontal size. Accuracy can be improved by changing to a faster analog-to-digital converter to make the range resolution considerable finer. Another approach would be to scan farther downstream where the plume is larger.

The sensitivity of the LIDAR system can be improved to reduce random noise caused by photon statistics of the rather weak raw signals obtained by OPAL. A larger-diameter receiving telescope, higher optical transmission in the system, and transmitting more photons (larger pulse energy and/or higher pulse rate) will increase sensitivity.

The stationary measurements suffered some complications and errors due to contamination by plumes of scattering particles from other sources. Although the airline hosting the stationary measurements was extremely helpful, the location was somewhat busy with ground vehicles, and sometimes other aircraft in the vicinity were taxiing and performing runups. The worst difficulty was self-contamination when light winds with a dominant tail-wind component to the test aircraft slowly blew its exhaust back into our sampling region. This seemed most significant in the B767 (B) case. This pooling or recirculation affected the LIDAR's comparison of plume signal against ambient, and may have added soot to the air ingested into the engine. Screening during quality assurance and the use of fore- and post-plume regions during data processing eliminated the worst cases, but couldn't remove all the effects. It would be good to design future tests to minimize such interferences.

When it is necessary to operate both engines, operating them at identical throttle settings would simplify data analysis and improve accuracy by eliminating the need to bootstrap the contribution of the secondary engine.

Engine operating parameters are a blend of ICAO data, Jane's data, and calculations based on simple assumptions. The air mass flow data come from Jane's, and the ultimate source of these values is unknown to this author. It would be worthwhile to investigate how these are determined and how accurate they are. Rather than using the simple assumptions described above, actual data on how thrust, air mass flow, exit nozzle velocity, and exhaust air temperature at the nozzle vary with throttle setting might improve determination of these parameters and accuracy of the result.

Alteration of ambient aerosol in the air passing through the engine and during mixing with the ambient air downstream is now estimated with simple approximations, as is the dilution of the air density of the warm plume. One factor not yet included is the loss of water from ambient particles in the bypass air and also ambient air mixing into further downstream due to a warm plume with lower relative humidity. This may be the reason there were more negative B767 *EI*'s than positive ones. These changes in ambient aerosol and plume density are significant or even dominate in low-soot plumes, so improving the assumptions and theory for them will lead directly to better accuracy in those cases.

By applying these improvements, a goal of reducing the uncertainty to $\pm(\ 0.01$ g/kg) $\pm 0.3 EI$ is reasonable.